



TECHNISCHE  
UNIVERSITÄT  
WIEN  
Vienna University of Technology

DISSERTATION

# Holographic descriptions of anisotropic plasma

ausgeführt zum Zwecke der Erlangung des akademischen Grades eines  
Doktors der technischen Wissenschaften unter der Leitung von

Univ. Prof. DI Dr. Anton Rebhan  
Institutsnummer E136  
Institut für Theoretische Physik

eingereicht an der Technischen Universität Wien  
Fakultät für Physik

von

**DI Dominik Steineder**  
Matrikelnummer 0425447  
Steinbrechergasse 24/13  
A-1220 Wien  
[steineder@hep.itp.tuwien.ac.at](mailto:steineder@hep.itp.tuwien.ac.at)

Wien, am 30.10.2012

Unterschrift



Dedicated to my brother Manuel,  
(10. 11. 1973 - 7. 12. 2011)

*Du bist nicht mehr da  
wo du warst,  
aber du bist überall  
wo wir sind.*



## Deutsche Kurzfassung

In Schwerionen-Kollisionen am “Large Hadron Collider” (LHC) und am “Relativistic Heavy Ion Collider” (RHIC) wird ein Materiezustand erzeugt, bei dem die ansonsten in Hadronen gebundenen Quarks und Gluonen ein Plasma bilden, dessen Eigenschaften Gegenstand intensiver Untersuchungen sind. Im Jahr 2005 wurde entdeckt, dass dieses Quark-Gluon-Plasma (QGP) sich überraschenderweise wie eine nahezu perfekte Flüssigkeit verhält mit einem extrem niedrigen Verhältnis von Scherviskosität zu Entropiedichte  $\eta/s$ . Dieses Verhältnis ist auch ein Indikator dafür, dass der erzeugte Materiezustand extrem stark gekoppelt ist, was störungstheoretische Zugänge erschwert. Um zeitabhängige Phänomene zu untersuchen, wo auch die Gittereichtheorien keine verlässlichen Ergebnisse liefern, muss man sich einer vermuteten Korrespondenz zwischen Gravitationstheorien in einer Raumzeit mit einer zusätzlichen Dimension und Eichtheorien bedienen. Diese bildet die Physik einer Eichtheorie bei starker Kopplung auf lösbare Probleme in der Gravitationstheorie ab. Mit Hilfe dieser sogenannten holographischen Dualität konnte beispielsweise der niedrige Wert von  $\eta/s$  erklärt werden.

In dieser Arbeit befassen wir uns mit Verallgemeinerungen der üblicherweise in isotropen Plasmen betrachteten Größen auf anisotrope Systeme, die eine Vorzugsrichtung (z.B. die Kollisionsachse) besitzen. Um diese mithilfe von Gravitationstheorien beschreiben zu können, diskutieren wir zwei Modelle mit sehr unterschiedlichen Eigenschaften. Zum besseren Verständnis untersuchen wir dabei auch den Grenzwert verschwindender Kopplung in einem der beiden Modelle und finden ein überraschend nichttriviales Phasendiagramm als Funktion von der Temperatur und einer anisotropen Ladungsdichte. Anschließend berechnen wir die spektralen Dichten für Photonen und Dileptonen in beiden Modellen und diskutieren die Unterschiede.

Eines der wichtigsten Resultate der vorliegenden Arbeit ist, dass die vermutete untere Schranke von  $\eta/s = 1/4\pi$  von einer der zwei Scherviskositäten, die in einem axialsymmetrischen anisotropen System definiert werden können, noch unterschritten wird. Dies war vorher nur durch Einführung von höheren Ableitungstermen in der Gravitationstheorie möglich. Wir zeigen, dass die Scherviskosität in der transversalen Ebene das bekannte Resultat  $\eta/s = 1/4\pi$  liefert, während die zweite diesen Wert für nichtverschwindende Anisotropien unterschreitet. Zusätzlich zu dem rein theoretischen Interesse an diesem Ergebnis könnte diese Entdeckung auch für ein in Schwerionen-Kollisionen erzeugtes QGP von Bedeutung sein, da angenommen werden kann, dass ein solches Plasma für einen beträchtlichen Teil seiner sehr kurzen Lebensdauer anisotrop ist.

Schließlich betrachten wir noch weitere interessante phenomenologische Größen in einem anisotropen Plasma, wie das Potential zwischen zwei unendlich schweren Quarks und einen Parameter, der die Unterdrückung von sogenannten Jets beschreibt. Diese Größen wurden auch in schwach gekoppelten Modellen für Plasmen mit einer

anisotropen Impulsverteilung berechnet und wir vergleichen die Ergebnisse für kleine und unendlich große Kopplungen. Diese Untersuchungen helfen uns dabei, die von uns betrachteten Modelle besser zu verstehen, werfen allerdings auch einige Fragen auf, welche wir am Ende dieser Arbeit zusammenfassen.

## Abstract

In heavy ion collisions at the “Large Hardon Collider” (LHC) and the “Relativistic Heavy Ion Collider” (RHIC) it is possible to provide conditions under which the quarks and gluons that are usually confined into hadrons become deconfined. This new state of matter is called quark gluon plasma (QGP) and its properties are currently under intense investigation. In 2005 it was discovered that the QGP, instead of behaving like a gas, is better described as a fluid with a surprisingly low ratio of shear viscosity to entropy density  $\eta/s$ . The fact that this ratio is so low also indicates that the produced matter interacts strongly and this limits the applicability of any perturbative approach considerably. To study real time phenomena such as transport coefficients also lattice gauge theories are not yet reliable. A powerful tool in this context is the conjectured duality between gravity theories in a spacetime with one additional dimension and a gauge theory, which maps the strong coupling limit of the gauge theory to a solvable problem in the gravity theory. Using this so called holographic duality it was possible to explain the extremely low value of  $\eta/s$ .

In this thesis we study generalizations of quantities which have been considered in spatially isotropic plasma for anisotropic systems that possess a preferred direction (e.g. the collision axis). To make use of the holographic duality we discuss two models with very different properties. To gain more insight we also discuss the limit of vanishing coupling in one of the models and find a surprisingly nontrivial phase diagram as a function of temperature and an anisotropic charge density. Next we compute the spectral densities for electromagnetic probes in both models and discuss the differences.

One of the most interesting aspects of this thesis is the demonstration that the conjectured lower bound for  $\eta/s = 1/4\pi$  can be violated by one of two shear viscosities present in an axisymmetric system. Values for  $\eta/s$  below this bound were found previously only by introducing higher derivative terms in the gravity action. We show that in a spatially anisotropic plasma the purely transverse component of the shear viscosity saturates the bound while the longitudinal shear viscosity is even smaller for any nonvanishing anisotropy. This finding is interesting from a purely theoretical point of view, but could also be of importance for QGP produced in heavy ion collisions, since it is reasonable to expect the plasma to be anisotropic for a significant time interval.

Finally, we consider further observables in an anisotropic plasma which are of phenomenological interest. These are the potential between two infinitely heavy quarks and the jet quenching parameter. Both were also computed in weakly coupled models with a fixed momentum anisotropy. We compare the results for small and infinitely large couplings. These investigations are useful to understand the holographic models better, but also raise new questions that we summarize at the end of this thesis.





# Contents

<b>1</b>	<b>Introduction</b>	<b>1</b>
1.1	The strong force . . . . .	1
1.2	Heavy ion collisions . . . . .	3
1.3	The holographic duality . . . . .	7
1.4	Adding a direction . . . . .	9
<b>2</b>	<b>Holographic models</b>	<b>11</b>
2.1	Singular gravity duals (JW model) . . . . .	11
2.2	Axion-dilaton-gravity duals (MT model) . . . . .	13
2.2.1	Construction of the gravity dual . . . . .	15
2.2.2	Thermodynamics . . . . .	17
2.2.3	Boundary theory at zero coupling . . . . .	27
<b>3</b>	<b>Photons and Dileptons</b>	<b>36</b>
3.1	Introducing Photons and Dileptons . . . . .	36
3.2	Production Rates . . . . .	37
3.3	Tensor Structure of Anisotropic Correlators . . . . .	38
3.4	Singular Gravity Duals . . . . .	39
3.4.1	Equations of Motion and Asymptotic Solution . . . . .	39
3.4.2	Spectral functions at strong coupling . . . . .	40
3.4.3	Numerical Results . . . . .	41
3.5	Anisotropically $\theta$ -deformed gauge theory . . . . .	50
3.5.1	Using the membrane paradigm . . . . .	50
3.5.2	Numerical results . . . . .	53
<b>4</b>	<b>Shear Viscosities of Anisotropic Plasma</b>	<b>63</b>
4.1	Outline of the computation . . . . .	64
4.2	Construction of Physical Modes . . . . .	65
4.3	Shear viscosities from Kubo's formula . . . . .	67
4.3.1	Computing at the horizon . . . . .	67
4.3.2	From the horizon to the boundary . . . . .	71

4.4	Momentum diffusion . . . . .	72
4.4.1	Mapping to vector perturbations . . . . .	72
4.4.2	Lowest lying quasinormal modes . . . . .	73
<b>5</b>	<b>Heavy Quarks</b>	<b>75</b>
5.1	Heavy quark static potential . . . . .	75
5.1.1	Holographic computations . . . . .	75
5.1.2	Comparison with weak-coupling calculations . . . . .	82
5.2	Jet quenching . . . . .	85
5.2.1	Holographic calculations . . . . .	85
5.2.2	Comparison with weak coupling calculations . . . . .	89
<b>6</b>	<b>Conclusion and Outlook</b>	<b>92</b>
<b>A</b>	<b>Basics of Relativistic Hydrodynamics</b>	<b>95</b>
A.1	Ideal Hydrodynamics . . . . .	95
A.2	Adding Dissipation . . . . .	96
A.3	Anisotropic Hydrodynamics . . . . .	97
A.4	Momentum Diffusion . . . . .	97
<b>B</b>	<b>Ingredients of the string theoretic foundation of AdS/CFT</b>	<b>99</b>
B.1	D-branes and Yang-Mills theory . . . . .	99
B.2	D-branes and Supergravity . . . . .	100
B.3	Statement of the Duality . . . . .	101
B.4	Holographic Renormalization . . . . .	102
<b>C</b>	<b>Hard-anisotropic-loop effective theory</b>	<b>105</b>
C.1	Distribution functions and normalization . . . . .	105
C.2	Relation to holographic models . . . . .	106
C.2.1	JW model . . . . .	106
C.2.2	MT model . . . . .	107
<b>D</b>	<b>Details of the anisotropic axion-dilaton-gravity dual</b>	<b>108</b>
D.1	Equations of motion . . . . .	108
D.2	Numerical solution . . . . .	109
D.2.1	Series expansion close to the horizon . . . . .	109
D.2.2	Series expansion close to the boundary . . . . .	110
D.2.3	Matching of solutions . . . . .	110

---

<b>E</b>	<b>Details on the zero-coupling limit of the MT model</b>	<b>112</b>
E.1	$T = 0$ contribution . . . . .	112
E.2	Finite $T$ contribution . . . . .	113
E.2.1	High- and low- $T$ expansions . . . . .	114
	<b>Acknowledgments</b>	<b>116</b>

# Chapter 1

## Introduction

### 1.1 The strong force

In the late 1950's and in the 1960's a large amount of experimental data relevant to the strong interaction was gathered. The large number of particles and resonances discovered called for a theoretical framework within which the data could be described. The perturbative method of quantum field theory, which had been so successful before when quantum electrodynamics had been found, was not capable of explaining the interactions of hadrons. Therefore, new formulations independent of the perturbative method were developed. Among others was a theory of relativistic strings. When considering a scattering amplitude of two hadrons to two hadrons it was observed that any finite sum of such amplitudes has uncontrollable UV divergencies and only an infinite number of terms might alter the UV behavior. After Veneziano proposed an amplitude with a softer UV behavior [1] it was discovered that this amplitude came out of theories of relativistic strings. One success of this model was to explain the Regge trajectories, which implied a linear relation of the mass squared and the spin of the resonances. This behavior was indeed found for many resonances experimentally. However, string theories had a number of shortcomings in explaining the strong interaction, for example the theory predicted a particle with negative mass, the tachyon, and a massless spin two particle that was not discovered. Therefore, string theory did not seem to be an appropriate description of the strong force.

On the other hand in the late 1960's studies on the classification of hadrons suggested that they were made out of more fundamental building blocks, the quarks [2]. Eventually the breakthrough in understanding the strong interaction was made in 1973 when the property of asymptotic freedom of non-Abelian gauge field theories was discovered [3, 4]. It was found that the interaction between the fundamental building blocks of the hadrons becomes weaker when the momentum transfer is increased

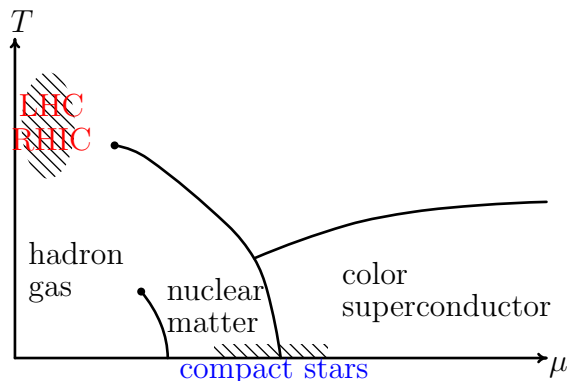


Figure 1.1: Schematic phase diagram of QCD as a function of temperature  $T$  and baryon chemical potential  $\mu$ . LHC and RHIC denote the regions of the phase diagram that are being explored by the experimental heavy ion programs at the LHC and RHIC.

and in this regime a description in terms of a perturbative quantum field theory appears possible. Experimentally asymptotic freedom was first observed in deep inelastic electron-proton scattering at SLAC (Stanford Linear Accelerator Center). At high enough energies and therefore high enough resolution of these collisions, it was observed that the electrons scattered off almost free and pointlike constituents of the proton.

For asymptotic freedom the non-Abelian nature of the gauge theory is crucial. However, this non-Abelian gauge theory required that the quarks have an extra symmetry which was dubbed “color”. Eventually we have all the ingredients to write down the Lagrangian of Quantum Chromodynamics (QCD), the widely accepted theory of the strong interactions

$$\mathcal{L} = -\frac{1}{4}F_{\mu\nu}^a F^{a\mu\nu} + \sum_{k=1}^{N_f} \bar{\psi}_k (i\gamma^\mu D_\mu - m_k) \psi_k, \quad (1.1)$$

with  $D_\mu = \partial_\mu - igT^a A_\mu^a$ . The  $T^a$ ’s are the generators of  $SU(3)$  the gauge group of QCD. The quarks  $\psi$  and the gluons  $A_\mu^a$  are in the fundamental and the adjoint representation, respectively. It is also easy to see from the Lagrangian that due to the non-Abelian character of QCD there exist self interactions of the gauge fields, which is the main source of asymptotic freedom.

At small energy scales the counterpart of asymptotic freedom is that the coupling constant increases and perturbative methods fail. This led to the development of low-energy effective models, which should incorporate only certain features of QCD, and numerical simulation of QCD on a spacetime lattice.

If we do not restrict our considerations to QCD in vacuum but consider finite temperatures and densities we can explore the QCD phase diagram. The regions of

asymptotically large temperatures and/or densities can be studied by perturbative methods. For small enough densities lattice gauge theory turned out to be the outstanding nonperturbative tool to study the thermodynamics of the system. It was discovered that while at small temperatures the fundamental degrees of freedom of QCD, namely the quarks and gluons, are confined to hadrons at temperatures above a certain threshold  $T_c \sim 150\text{MeV}$  a so called quark-gluon plasma (QGP) forms [5, 6]. Actually the QGP was the state of matter our universe was in for until about  $10^{-5}\text{s}$  after the big bang. A theorist's way of producing such a QGP would be to take an empty box and heat it up. As the temperature increases mesons will form. At some point the density of mesons will be so high that they start to overlap. The quarks and gluons then no longer know to which meson they originally corresponded and can move through the box, they are deconfined.

## 1.2 Heavy ion collisions

Of course the theorist's approach to produce a QGP is not feasible in reality and experimentalists have to work hard to produce the deconfined phase of QCD in high energy collisions of heavy ions here on earth more than 13 billion years after the big bang. The first attempts to study nucleus-nucleus collisions go back to the early 1970's even, when such experiments were performed at the Lawrence Berkeley National Laboratory. These collisions took place at fixed target energies ranging up to 2 GeV and had the main purpose to study compressed baryonic matter [7]. In order to address the deconfined phase of QCD higher center of mass energies  $\sqrt{s}$  were needed. In the 1980's two more fixed target experiments at Brookhaven National Laboratory (BNL) and at CERN, namely the Alternating Gradient Synchrotron (AGS) and the Super Proton Synchrotron (SPS), delivered data for heavy ion collisions at  $\sqrt{s} = 5$  GeV and 17 GeV per nucleon pair, respectively. However, only after the Relativistic Heavy Ion Collider (RHIC) at BNL started operating in 2000 at center of mass energies of 200 GeV per nucleon pair, it was possible to safely confirm the production of the QGP. Ten years later in 2010 the heavy ion program at the Large Hadron Collider (LHC) at CERN started and set new records, since there lead ions collide at  $\sqrt{s} = 2.76$  TeV per nucleon pair and center of mass energies of up to 5.5 TeV are planned.

After this short historical remarks let us briefly discuss how such a heavy ion collision looks like. Since the nuclei are highly accelerated to almost the speed of light they appear strongly Lorentz contracted in the laboratory frame. The nuclei collide head on with a certain impact parameter  $b$ , which specifies the displacement of the centers of the two ions in the transverse plane. A non-central collision is shown schematically in Figs. 1.2 and 1.3. For high enough energy densities the QGP forms in the collision region. The spectator nucleons that do not participate in the collision

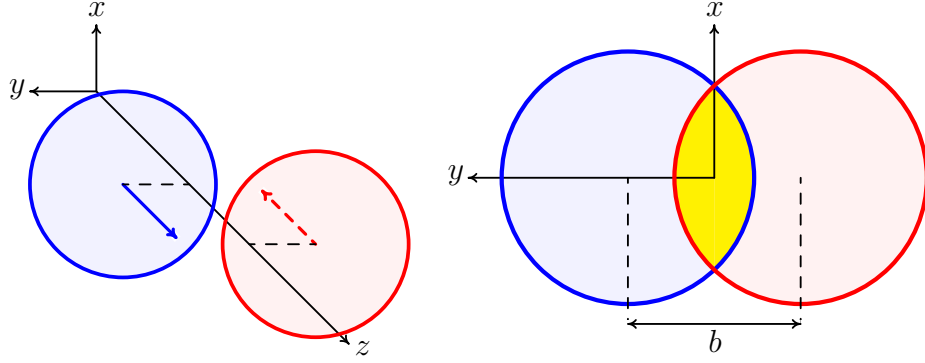
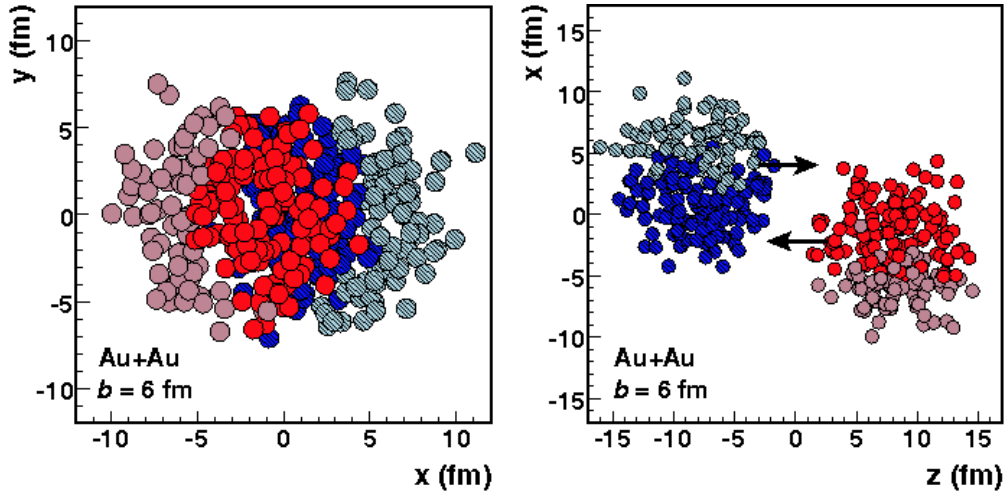


Figure 1.2: Geometry of a high energy heavy ion collision.

Figure 1.3: Glauber Monte Carlo simulation of two gold nuclei at an impact parameter  $b = 6$  fm in the transverse plane (left) and from a side view (right). Spectator particles are shown in pale color. Figure from [8].

simply fly further along the collision axis. Due to longitudinal expansion at very early times after the two nuclei hit each other the produced plasma will be out of equilibrium and have a sizable anisotropy. We will return to this issue in a later section. The plasma then quickly expands and thermalizes. Due to the expansion the temperature drops and at some point the deconfined quarks and gluons hadronize and form up to several thousands of hadrons in the final state that can be detected. The average number of produced hadrons per collision depends on the center of mass energy and reaches 8000 for top RHIC energies [9, 10].

The lifetime of the QGP is only of the order of some fm/c and we have to rely on indirect evidences that a deconfined state of matter has formed shortly after the collision. Some of the observables that indicate the formation of QGP are

- *elliptic flow*: In non-central collisions ( $b \neq 0$ ) the region in which the plasma forms has an almond shape in the transverse plane. If the medium thermalizes quickly enough this anisotropic shape leads to a larger pressure gradient along the shorter diameter than along the longer diameter. Hydrodynamic evolution converts the initial pressure gradients to velocity gradients in the final state. Elliptic flow is quantified in terms of the second Fourier coefficient  $v_2$  of the particle distribution in the transverse plane

$$p_0 \frac{dN}{d^3p} \Big|_{p_z=0} = v_0(p_T) \left( 1 + 2v_1(p_T) \cos(\phi) + 2v_2(p_T) \cos(2\phi) + \dots \right), \quad (1.2)$$

where  $\phi$  is the angle between the momentum vector and the  $x$ -axis. The surprising experimental finding is that by comparing the elliptic flow to hydrodynamic simulations it turns out that the ratio of shear viscosity to entropy density  $\eta/s$  has to be remarkably small, of the order of 1/10 [11, 12]. We present some details of this reasoning in Appendix A. On the other hand the value of  $\eta/s$  can also be viewed as an indication of the interaction strength, because for a weakly coupled plasma

$$\eta/s = \frac{\#}{g^4 \log(\#/g)}. \quad (1.3)$$

Inserting the precise coefficients that can be found in [13] and extrapolating the result to large gauge couplings  $g \sim 1$  we would obtain  $\eta/s \sim 5$ , which is still a magnitude too large to explain the experimental findings. This seems to suggest that the deconfined medium produced in heavy ion collisions behaves like a strongly coupled liquid rather than a weakly coupled gas.

- *jet quenching*: During the initial stage after the collision a pair of high energetic partons can have formed within the deconfined medium and travel in opposite directions through the plasma. Subsequently they lose energy to the medium



and slow down. If this pair is produced close to one edge of the QGP such that one parton can escape the medium almost unmodified and manifests itself as a jet in the detector, the other parton has to travel a significant distance through the QGP and loses energy. Therefore, there appears a less energetic (or in extreme cases even no) backward jet corresponding to the one that belongs to the first parton. This behavior has been observed at RHIC and LHC [14, 15].

Aside from this intuitive phenomenon experimentalists also quantify the slow down of initially fast partons by the nuclear suppression factor

$$R_{AA} = \frac{1}{N_{coll}} \frac{dN/dp_T^{AA}}{dN/dp_T^{pp}}. \quad (1.4)$$

$R_{AA}$  gives the yield of a particle species in heavy ion collisions, typically measured as a function of its transverse momentum, divided by the similar yield of proton-proton collisions scaled such that the number of independent nucleon-nucleon collisions are the same. A deviation of  $R_{AA}$  from 1 reflects either medium effects or initial state effects. The latter can be studied in collisions of deuterons or protons with heavy ions, because then one does not expect a QGP to be formed. Eventually experiments revealed that hadrons do show suppression due to the presence of QGP [16, 17]. A nice check is that photons which do not interact strongly with the medium are not suppressed [18].

- *quarkonia*: By quarkonia we mean bound states of a charm  $c$  or bottom  $b$  quark and its antiquark. Due to the larger mass of the charm and the bottom these mesons have a smaller size. In a QGP of temperature  $T$ , the plasma can resolve distances down to  $1/T$  and therefore screen quarks which are separated down to this distance. However, since quarkonia of heavy quarks are bound more strongly, their dissociation temperatures are higher. If we could now subsequently increase the temperature of the QGP we would at first detect the usual rate of charmonium states but as the temperature increases  $c\bar{c}$  states cannot form in the QGP and their rate would be suppressed. However, as long as we are below the dissociation temperature of the still stronger bound  $b\bar{b}$  system the bottomium mesons should not yet be suppressed. This sequential suppression pattern of quarkonium states is a generic prediction of all models of quarkonium suppression. So far only the lightest charmonium state  $J/\psi$  has been investigated and we have to wait for more statistics at LHC and RHIC. However, due to the higher collision energy at the LHC and related to this the much higher production rate of bottomium, detailed studies of quarkonium suppression become available [19].

### 1.3 The holographic duality

As we have just pointed out, heavy ion collision experiments suggest that the QGP produced is a strongly coupled quantum liquid and therefore describing it will involve nonperturbative methods. In the first section we have already mentioned lattice gauge theory as an outstanding nonperturbative tool, but it turns out that its utility is limited. For example, currently real time phenomena such as transport coefficients or out of equilibrium situations can not be described reliably.

However, in 1997 a new powerful nonperturbative tool was discovered, namely the holographic duality<sup>1</sup> [20]. The remarkable feature of this duality is that it maps a problem in a  $d$ -dimensional field theory without gravity to a problem in a  $(d + 1)$ -dimensional theory with gravity. The main advantage of this duality is that problems that are hard to solve, because they involve strong or even infinite couplings, are mapped to problems that can be solved much more easily in the dual theory. Since this implies a connection between two different theories in different spacetime dimensions, this duality is often referred to as holographic duality. In the last decade most constraints of the original formulation, such as conformality, have been relaxed, but no violation of the duality has been found. Therefore, in [10] the situation is summarized as “from the current point of view, holographic duality is simply a true, if as yet unproven, fact about quantum field theories and quantum gravity.”

In this introductory section we only attempt to motivate the holographic duality heuristically (see also [21, 22, 23]). The term holographic can be understood by considering entropy in quantum field theories without gravity, where it scales like the volume and the entropy of black holes that scales like the area. The fact that black holes are states with maximal entropy in gravity theories is a hint that the quantum field theory without gravity can only live in a spacetime with one dimension less, if we attempt to identify the two entropies. Actually this extra dimension can be understood by the renormalization group (RG). A quantum field theory can be sliced up by the energy scale and it was found that the running of coupling constants as a function of this RG scale  $r$  can be described by local equations

$$r\partial_r g(r) = \beta(g(r)), \quad (1.5)$$

where  $\beta$  is the famous beta function. Let us for simplicity consider a theory with  $\beta = 0$  that is symmetric under rescaling of the coordinates  $x^\mu \rightarrow \lambda x^\mu$  and the energy scale  $r \rightarrow r/\lambda$ . The most general  $(d + 1)$  dimensional metric with scale and Poincaré invariance is

$$ds^2 = \frac{L^2}{v^2} (\eta_{\mu\nu} dx^\mu dx^\nu + dv^2), \quad (1.6)$$

---

<sup>1</sup>This duality is also known as gauge/gravity duality or AdS/CFT, where AdS stands for anti-de Sitter spacetime, which is a homogenous and isotropic spacetime with constant negative curvature and CFT is the acronym for conformal field theory.

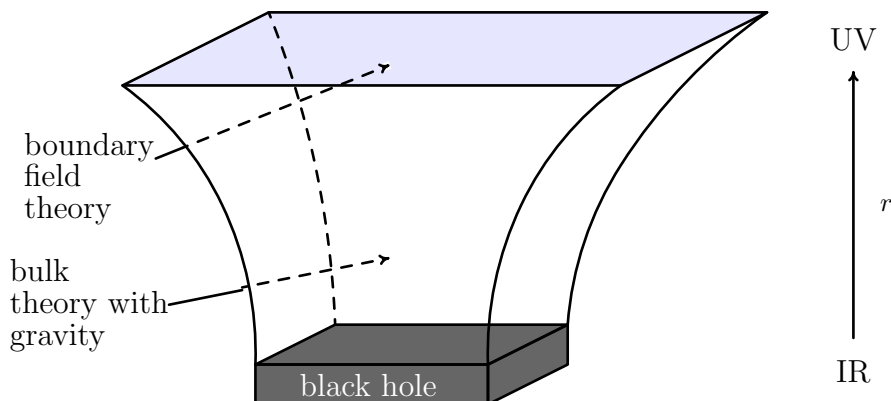


Figure 1.4: Schematic illustration of the gauge/gravity duality.

where we have changed the coordinate system to  $v = L^2/r$ . This is the metric of  $\text{AdS}_{d+1}$  with  $L$  being the AdS radius, which solves the equations of motion of the action

$$S_{\text{bulk}} = \frac{1}{16\pi G_N} \int d^{d+1}x \sqrt{-g} (\mathcal{R} - 2\Lambda), \quad (1.7)$$

(where  $\mathcal{R}$  is the Ricci scalar and  $\Lambda$  is the cosmological constant) for  $\Lambda = -d(d-1)/(2L^2)$ . On the other hand this metric represents a family of copies of Minkowski space parametrized by  $v$ . It is interesting that this spacetime has a boundary at  $v = 0$  which corresponds to the UV in the quantum field theory, where we have to specify boundary conditions. It is also common to say that the field theory “lives” at the boundary. Variants of this simplest case can be obtained for example by considering a black hole in the gravity theory. This corresponds to thermal states in  $d$  dimensional field theory, identifying the temperature and entropy of the black hole with the temperature and entropy of the thermal ensemble in the quantum field theory. Pictorially this is represented in Fig. 1.4. Furthermore, it is possible to include a number of additional fields in the bulk action and study different lower dimensional field theories. Sometimes gravity duals can be consistently obtained from string theory in which case the duality is precisely known. This is often called a top-down approach. In bottom-up approaches one postulates a gravity dual with a certain field content and certain properties and studies the corresponding quantum field theory that might only be defined via the holographic duality. We present some details of the original argument for this duality as well as aspects that are of certain interest for us later in Appendix B.

The main issue in a direct attack of the problems of strongly coupled QGP is that there exists no known gravity dual to QCD so far. Therefore, we can only study theories that share certain properties with QCD and try to identify some universal trends. This strategy has proven useful in the past, when for example the shear

viscosity of an  $\mathcal{N} = 4$  super Yang-Mills (SYM) plasma in equilibrium was calculated [24]. First of all the result was found to be the same for a large class of gravity duals corresponding to different deformations of the field theory and secondly the value  $\eta/s = 1/4\pi$  is surprisingly close to the measured value. But nevertheless we should be aware that whether  $\mathcal{N} = 4$  SYM theory is a good toy model for QCD depends strongly on the observables we want to consider. For example  $\mathcal{N} = 4$  SYM is conformal and the coupling constant does not run. This implies that even at asymptotically large temperatures the coupling constant will remain large in contrast to QCD.

Furthermore, there is no confinement. Some of the differences become small for a certain temperature range where the QCD matter is strongly coupled, approximately conformal and deconfined. We also note that some of the above differences, such as confinement can nevertheless be mimicked by more refined gravity duals. But it is still important to keep in mind that ultimately it is not QCD we are studying when we apply the holographic duality and we have to think about the validity of our results carefully in the context of QCD. Nevertheless it seems legitimate to note that 30 years after string theory attempted to be the theory of the strong force, eventually it celebrates a comeback in the QCD community since it can be useful to understand the strongly coupled quantum liquid produced in heavy ion collisions.

## 1.4 Adding a direction

The main motivation for the work that will be presented in the following chapters is to gain a better understanding of the early stages of the strongly coupled quantum liquid produced after the heavy ion collision. At this point the plasma is not yet completely thermalized, and due to the collision axis there is one preferred direction present. Some studies even indicate that the plasma may have substantial pressure anisotropies over its entire lifetime [25, 26, 27, 28]. Taking this anisotropy into account already led to interesting new phenomena at weak coupling. The probably most exciting feature is the development of non-Abelian plasma instabilities [29, 30, 31, 32, 33, 34, 35, 36]. These turned out to be the parametrically dominant phenomena in anisotropic weakly coupled QGP and therefore play an important role in processes like thermalization. But also other observables such as the photon production rate, jet quenching parameter or the properties of quarkonium states are affected by the anisotropy.

At strong coupling the investigation of anisotropic systems has just begun. One route is to model heavy ion collisions dynamically making use of the holographic duality. In these approaches shock wave collisions in the dual gravity theory were studied. These works involve solving Einstein's equations numerically and therefore obtain a metric that is changing in time [37, 38, 39, 40, 41, 42]. Transferring the results via the holographic duality to SYM plasma it was possible to gain information

of the time evolution of the energy density and pressures of the deconfined plasma. Due to the axisymmetry of the system there exist two distinct pressures, one along the collision axis and one transverse to it. Even though these pressures follow a hydrodynamic evolution already at quite early times, there is nevertheless a sizable pressure anisotropy present for a long period. Unfortunately, it is notoriously difficult to gain further insight in anisotropic systems with these time evolving geometries. In a first attempt to gain a better understanding about the features that might be introduced in the strongly coupled plasma by the presence of an anisotropy, it seems natural to start with a stationary setting. This can only be a good approximation to the physics of collisions on short enough time scales and the validity might be significantly limited. Nevertheless from a purely theoretical point of view one might find completely new behavior related to the presence of the anisotropy. Eventually it is also of interest to compare the results to the weak coupling case, where also stationary systems are considered regularly.

As a remark and further motivation we also want to point out that anisotropic systems at strong coupling are not only interesting in the context of heavy ion collisions, but also for condensed matter systems, where some of the assumptions about stationarity might even be easier to satisfy. As an example we can mention superfluid liquid helium-3 which is a so called p-wave superfluid and breaks rotational symmetry under certain external circumstances [43]. Holographic models mimicking a phase transition to an anisotropic superfluid have been constructed e.g. in [44, 45]. Other anisotropic systems that might be interesting for applying similar ideas we are going to discuss in this thesis are nematic fluids also known as liquid crystals [46].

After these introductory sections where we have tried to sketch the base this work relies on and motivate the questions we are going to investigate in the remaining chapters, we turn to two specific models to study effects of anisotropies at strong coupling in chapter 2. There we will review in detail the construction of the gravity duals and comment on the features of the boundary theories. Next, we calculate spectral functions for electromagnetic probes and study the modifications in the presence of a spatial anisotropy in chapter 3. In chapter 4 we will compute the shear viscosity for one of the anisotropic models in different ways. Finally, we turn to study infinitely heavy quarks as probes of the anisotropic plasma and compare our findings to computations at weak coupling in chapter 5. Most of the results discussed in the present thesis have been published in [47, 48, 49, 50]. Finally, we are going to draw conclusions and give an outlook for further work. We relegated the review of some basic concepts and also some detailed computations to the appendices A - E.

# Chapter 2

## Holographic models

In the introduction 1.3 we have motivated that the infinite coupling regime of certain quantum field theories becomes manageable in terms of a dual gravity theory in asymptotically AdS spacetime with an additional dimension. In this chapter we introduce two different gravity duals that describe an  $\mathcal{N} = 4$  SYM theory with a fixed anisotropy.

### 2.1 Singular gravity duals (JW model)

By making use of the holographic duality expectation values of local operators in the gauge theory can be reconstructed from the asymptotics of the dual supergravity fields near the boundary. The field corresponding to the stress-energy tensor  $T_{\mu\nu}$  is the metric and the reconstruction of  $\langle T_{\mu\nu} \rangle$  from the near-boundary asymptotics has been studied in [51, 52, 53] and is also discussed briefly in appendix B.

Let us consider a generic asymptotically AdS metric in so-called Fefferman Graham coordinates (in the following we set the AdS radius  $L = 1$ )

$$ds^2 = \frac{1}{v^2} (dv^2 + g_{\mu\nu}(x, v) dx^\mu dx^\nu), \quad (2.1)$$

where the indices  $\mu, \nu = 0, 1, 2, 3$  do not include the holographic coordinate. Solutions of vacuum Einstein's equations with negative cosmological constant  $\Lambda = -6$ , which correspond to  $\text{AdS}_5$ , give for the expansion close to the boundary at  $v = 0$

$$g_{\mu\nu}(x, v) = g_{(0)\mu\nu}(x) + g_{(2)\mu\nu}(x)v^2 + g_{(4)\mu\nu}(x)v^4 + \dots \quad (2.2)$$

Here  $g_{(0)\mu\nu}(x)$  is the metric of the boundary quantum field theory that we choose to be the flat Minkowski metric  $g_{(0)\mu\nu}(x) = \eta_{\mu\nu}$ . It can then be checked that  $g_{(2)\mu\nu}(x) = 0$  and

$$g_{(4)\mu\nu}(x) = \frac{2\pi^2}{N_c^2} \langle T_{\mu\nu}(x) \rangle. \quad (2.3)$$

However, this whole procedure can also be reversed, namely constructing a general supergravity solution from a given stress energy tensor [53]. Vacuum Einstein's equations impose only two constraints on the stress-energy tensor namely energy momentum conservation and tracelessness. The latter can be shown for general metrics by considering the leading terms with respect to  $v \rightarrow 0$  of the  $vv$ -component of Einstein's equations<sup>1</sup>. For a specified  $\langle T_{\mu\nu} \rangle$  it is then in principle possible to obtain all higher terms  $g_{(n)\mu\nu}(x)$  recursively from Einstein's equations and therefore reconstruct the corresponding gravity dual. In [55] this method has been used to rederive the static black hole for  $\langle T_{\mu\nu} \rangle = \text{diag}(\epsilon, P, P, P)$  with  $\epsilon = 3P$ , but also other gravity duals such as the single planar shock wave or boost-invariant geometries were derived. The latter were obtained by considering a stress energy tensor of the form  $\langle T_{\mu\nu} \rangle = \text{diag}((\epsilon(\tau), P_\perp(\tau), P_\perp(\tau), P_z(\tau)))$  only depending on proper time  $\tau = \sqrt{t^2 - z^2}$ .

Here we are interested in a stationary anisotropic stress-energy tensor

$$\langle T_{\mu\nu} \rangle = \text{diag}(\epsilon, P_\perp, P_\perp, P_z), \quad \langle T^\mu_\mu \rangle = 0, \quad (2.4)$$

which we consider as an approximation to the full dynamics at sufficiently short time scales. A primary measure of the anisotropy of the boundary field theory is the pressure anisotropy defined as

$$\Delta = \frac{P_\perp}{P_z} - 1, \quad (2.5)$$

where  $\Delta > 0$  ( $\Delta < 0$ ) corresponds to an oblate (prolate) plasma.

A metric that respects the symmetries of our anisotropic plasma takes the general form

$$ds^2 = \frac{1}{v^2} (-a(v)dt^2 + c(v)(dx^2 + dy^2) + b(v)dz^2 + du^2). \quad (2.6)$$

Solving five-dimensional Einstein's equations

$$R_{MN} - \left(\frac{1}{2}\mathcal{R} - \Lambda\right)g_{MN} = 0 \quad (2.7)$$

with a negative cosmological constant  $\Lambda = -6$  and the Ricci scalar  $\mathcal{R} = -20$  for the 5-dimensional metric (2.6) respecting the boundary conditions defined by the flat Minkowski metric and the stress-energy tensor we find [56]

$$\begin{aligned} a(v) &= (1 + A^2 v^4)^{1/2 - \sqrt{36 - 2B^2}/4} (1 - A^2 v^4)^{1/2 + \sqrt{36 - 2B^2}/4} \\ b(v) &= (1 + A^2 v^4)^{1/2 - B/3 + \sqrt{36 - 2B^2}/12} (1 - A^2 v^4)^{1/2 + B/3 - \sqrt{36 - 2B^2}/12} \\ c(v) &= (1 + A^2 v^4)^{1/2 + B/6 + \sqrt{36 - 2B^2}/12} (1 - A^2 v^4)^{1/2 - B/6 - \sqrt{36 - 2B^2}/12}. \end{aligned} \quad (2.8)$$

---

<sup>1</sup>For boost invariant metrics the tracelessness condition is derived from vacuum Einstein's equations in [54], but the same arguments are valid in general.

The parameters  $A$  and  $B$  are related to the energy density and the pressures according to

$$\epsilon = \frac{N_c^2}{2\pi^2} \left( \frac{A^2}{2} \sqrt{36 - 2B^2} \right), \quad (2.9)$$

$$P_\perp = \frac{N_c^2}{2\pi^2} \left( \frac{A^2}{6} \sqrt{36 - 2B^2} + \frac{A^2 B}{3} \right), \quad (2.10)$$

$$P_z = \frac{N_c^2}{2\pi^2} \left( \frac{A^2}{6} \sqrt{36 - 2B^2} - \frac{2A^2 B}{3} \right). \quad (2.11)$$

$A$  is a dimensionful parameter which in the isotropic case ( $B = 0$ ) is related to the temperature  $T$  according to  $A = \pi^2 T^2 / 2$ . Nonvanishing values of the dimensionless parameter  $B$  characterize the anisotropy of the system, since  $P_z$  and  $P_\perp$  depend differently on  $B$ . For negative  $B$  the plasma is prolate, while it is oblate for positive  $B$ . Particular values of  $B$  are  $B = \sqrt{2}$ , where  $P_L = 0$  ( $\Delta = \infty$ ), and  $B = -\sqrt{6}$  where  $P_T = 0$  ( $\Delta = -1$ ), because in a plasma made of free particles, such values correspond to maximal anisotropies, but the above geometry permits also negative values of pressure components for larger  $B$  (limited only by  $|B| < \sqrt{18}$ ).

The metric given in eq. (2.6) is pathological in the sense that a naked singularity appears whenever  $B$  does not vanish. For instance, the induced metric at constant  $t$  and  $v = 1/\sqrt{A}$  is degenerate,

$$b(v)c(v)^2 \propto (1 - A^2 v^4)^{(6 - \sqrt{36 - 2B^2})/4}. \quad (2.12)$$

Three-dimensional space degenerates at  $v = 1/\sqrt{A}$  into a two-dimensional sheet when  $B > 0$  and into a one-dimensional line when  $B < 0$ . This is illustrated in Fig. 2.1 in terms of asymptotically ( $v \rightarrow 0$ ) spherical congruences of holographically radial light-like geodesics. At finite  $v$  these are deformed into ellipsoids, which degenerate at  $v = 1/\sqrt{A}$ . However, in [56] it was noted that it is nevertheless possible to define purely ingoing and outgoing boundary conditions at the naked singularity, which gives for example the possibility to define retarded current-current correlation functions<sup>2</sup>. The same strategy we just explained was also used to obtain numerically a gravity dual for an anisotropic plasma with multiple  $U(1)$  charges in [57].

## 2.2 Axion-dilaton-gravity duals (MT model)

From the previous section we conclude that for vacuum Einstein's equations we only find singular geometries if we choose the stress-energy tensor of the boundary theory

<sup>2</sup>However, the expansion in small  $B$  performed in [56] is not really allowed, because the character of the singularities in the equations of motion changes if we truncate at linear order in  $B$ . We will study this in detail in chapter 3.



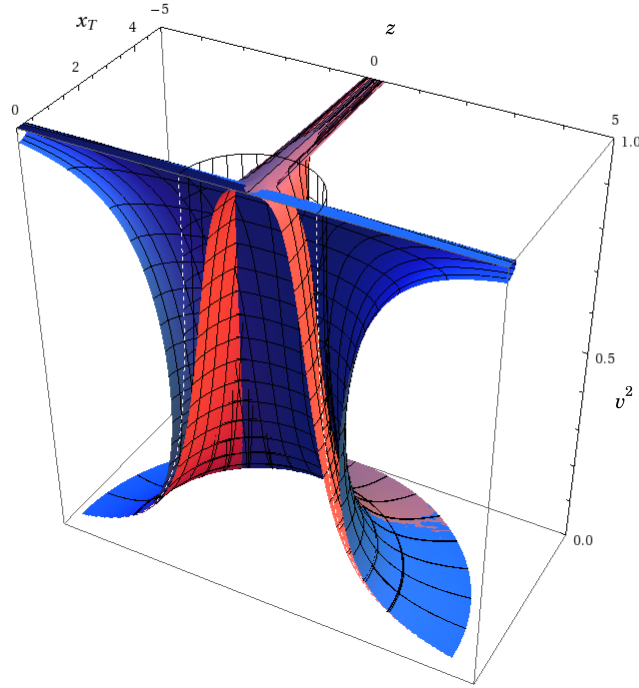


Figure 2.1: Asymptotically spherical congruences of (holographically) radial light-like geodesics which get deformed into ellipsoids as they approach the singularity at  $v = 1$  in units where  $A = 1$ . The blue (darker) surface corresponds to prolate anisotropy  $B = -\sqrt{6}$ , the red (lighter) surface to oblate anisotropy  $B = \sqrt{2}$ , and the transparent mesh to the isotropic case  $B = 0$ . Here  $x_T = \sqrt{x^2 + y^2}$  and  $z$  correspond to the spatial extents of the ellipsoids with  $x^2 + y^2 + z^2 = \text{const}$ , which degenerate into an infinite disk or line for oblate or prolate anisotropy, respectively. (Note that  $x_T$  is a radial variable.)

to be stationary and antisymmetric. In this section we therefore review another model for stationary anisotropic plasma at strong coupling described in [58, 59]. The main difference to the aforementioned approach is that we need to consider axions and dilatons in the supergravity theory to be able to introduce a spatial anisotropy in a regular geometry without naked singularities.

### 2.2.1 Construction of the gravity dual

The action for the type IIB supergravity in the string frame with non-trivial metric  $g_{MN}$ , axion  $\chi$ , dilaton  $\phi$  and Ramond-Ramond (RR) five form  $F_5$  is

$$S = \frac{1}{\kappa_{10}^2} \int d^{10}x \sqrt{-g} \left[ e^{-2\phi} (\mathcal{R} + 4\partial_{\tilde{M}}\phi\partial^{\tilde{M}}\phi) - \frac{1}{2}F_1^2 - \frac{1}{4 \cdot 5!}F_5^2 \right], \quad (2.13)$$

where  $\tilde{M} = 0, \dots, 9$  and  $F_1 = d\chi$  is the axion field-strength [60, 59]. The equation of motion for the dilaton is

$$\mathcal{R} + 4g^{\tilde{M}\tilde{N}}(\nabla_{\tilde{M}}\nabla_{\tilde{N}}\phi - \partial_{\tilde{M}}\phi\partial_{\tilde{N}}\phi) = 0 \quad (2.14)$$

and Einstein's equations become

$$R_{\tilde{M}\tilde{N}} + 2\nabla_{\tilde{M}}\nabla_{\tilde{N}}\phi + \frac{1}{4}g_{\tilde{M}\tilde{N}}e^{2\phi}(F_{\tilde{M}}F_{\tilde{N}} + \frac{1}{48}F_{\tilde{M}\tilde{A}\tilde{B}\tilde{C}\tilde{D}}F_{\tilde{N}}^{\tilde{A}\tilde{B}\tilde{C}\tilde{D}}) = 0. \quad (2.15)$$

The forms have to obey equations of motion

$$d \star F_1 = 0 \quad \text{and} \quad d \star F_5 = 0, \quad (2.16)$$

where  $\star$  denotes the ten-dimensional Hodge dual. Additionally, they satisfy Bianchi identities

$$dF_1 = 0 \quad \text{and} \quad dF_5 = 0 \quad (2.17)$$

and the self-duality constraint  $F_5 = \star F_5$ .

To obtain an anisotropic gravity dual preserving rotational invariance only in the  $xy$ -plane we make an ansatz for the string-frame metric

$$ds^2 = \frac{1}{u^2} \left( -\mathcal{F}\mathcal{B}dt^2 + dx^2 + dy^2 + \mathcal{H}dz^2 + \frac{du^2}{\mathcal{F}} \right) + \mathcal{Z}d\Omega_{S_5}^2, \quad (2.18)$$

with  $\Omega_{S_5}$  being the metric of a unit five sphere. In the above expression we have used reparametrization invariance to fix  $g_{xx}$  and  $g_{yy}$ . Therefore it is not possible to set  $\mathcal{B} = 1$ , but we can use a scaling symmetry to demand  $\mathcal{B}_{bdry} = 1$  and the boundary is located at  $u = 0$ . It is also possible to achieve  $\mathcal{H}_{bdry} = 1$  which is necessary to be able

to obtain asymptotically AdS spacetime. In general we want all the functions  $\mathcal{F}$ ,  $\mathcal{B}$ ,  $\mathcal{H}$ ,  $\mathcal{Z}$  and  $\phi$  to be functions of the holographic coordinate  $u$  only. Finally,  $\mathcal{F}$  allows for the introduction of a black hole and the horizon is located at  $u_h$  where  $\mathcal{F}(u_h) = 0$ .

The self-dual five form is proportional to the volume of the five sphere

$$F_5 = \alpha(\Omega_{S_5} + \star\Omega_{S_5}). \quad (2.19)$$

The equations of motion for the dilaton and the metric imply that  $\alpha = 4e^{-\phi_{bdry}}$ . Without loss of generality we choose the dilaton to vanish at the boundary and get  $\alpha = 4$ . To get an anisotropic gravity dual we want the axion to be  $\chi = az$ . Both  $F_5$  and  $F_1 = d\chi$  obey the equations of motion (2.16) and Bianchi identities (2.17). We can simplify the ansatz further by setting

$$\mathcal{H} = e^{-\phi} \quad \text{and} \quad \mathcal{Z} = e^{\frac{\phi}{2}}. \quad (2.20)$$

With these choices the  $S_5$  part of the spacetime factorizes in the Einstein frame, reducing the bulk action to five-dimensional axion-dilaton gravity with a negative cosmological constant that comes from the five-form flux  $F_5$

$$\begin{aligned} S_{bulk} = & \frac{1}{2\kappa^2} \int_{\mathcal{M}} d^5x \sqrt{-g} \left[ \mathcal{R} + 12 - \frac{1}{2} \partial_M \phi \partial^M \phi - \frac{e^{2\phi}}{2} \partial_M \chi \partial^M \chi \right] \\ & + \frac{1}{2\kappa^2} \int_{\partial\mathcal{M}} d^4x \sqrt{-\gamma} 2K, \end{aligned} \quad (2.21)$$

where  $M = 0, \dots, 4$  and  $\kappa^2 = 8\pi G = 4\pi^2/N_c^2$ .  $\gamma_{\mu\nu}$  is the induced metric on the boundary of the manifold  $\mathcal{M}$  and  $K$  is the trace of the extrinsic curvature. In the Einstein frame the metric is given by

$$ds^2 = \frac{e^{-\frac{\phi}{2}}}{u^2} \left( -\mathcal{F}\mathcal{B}dt^2 + dx^2 + dy^2 + \mathcal{H}dz^2 + \frac{du^2}{\mathcal{F}} \right). \quad (2.22)$$

The functions  $\mathcal{F}$ ,  $\mathcal{B}$ ,  $\mathcal{H}$  and  $\phi$  can be obtained numerically by solving the equations of motion. The details are given in [59] and to some extent in appendix D.1. It is important to note that by looking at the asymptotic equations of motion it is possible to verify that  $\mathcal{F}_{bdry} = \mathcal{H}_{bdry} = \mathcal{B}_{bdry} = 1$  for  $\phi_{bdry} = 0$  and therefore that the induced metric on the boundary is flat.

After we found a spatially anisotropic gravity dual that requires a one-form  $F_1$  and a five form  $F_5$ , we turn to the question what the corresponding field theory will be. The  $C_4$  charge coming from  $F_5 = dC_4$  can be related to D3-branes. The axion can actually be related to a  $C_8$  charge by  $\star d\chi = \tilde{F}_9 = dC_8$  and is associated with D7-branes. The D3-branes extend along the 4 boundary theory directions while the D7-branes wrap the  $S_5$  and are additionally extended only along  $t$ ,  $x$ , and  $y$  (see

		$t$	$x$	$y$	$z$	$u$	$S^5$
$N_c$	$D3$	x	x	x	x		
$N_{D7}$	$D7$	x	x	x			x

Table 2.1: Brane set-up.

also Table 2.1). We will denote the density of D7-branes along the  $z$ -direction by  $n_{D7} = dN_{D7}/dz$ .

Starting only with D3-branes gives  $\mathcal{N} = 4$  SYM theory. Adding now  $n_{D7}$  D7-branes sources a non trivial axion which itself appears in the Wess-Zumino term of D3-branes giving the following deformation <sup>3</sup>

$$\delta S = \frac{1}{8\pi^2} \int_{D3} \hat{\theta} \text{Tr} F \wedge F = \frac{1}{4\pi} \int_{D3} \hat{\chi} \text{Tr} F \wedge F = \frac{1}{g_{YM}^2} \int_{D3} \chi \text{Tr} F \wedge F. \quad (2.23)$$

Since  $\chi = az$  this clearly breaks isotropy. A very similar brane set-up was also used to model the fractional quantum Hall effect in [61]. However, there and in [60] the geometry of the gravity dual considered did not asymptote to AdS. Recently in [62] another related gravity dual with jumps in the  $\theta$ -parameter as a function of  $z$  was considered as a model for topological insulators and the authors argue that the MT model can actually be viewed as a continuum of jumping axion solutions smeared in the  $z$ -direction. However, an important difference is that the D7 branes in [62] do extend to the boundary in contrast to the situation in the MT model.

## 2.2.2 Thermodynamics

### Temperature and entropy

After discussing the construction of the gravity dual and the corresponding deformation of the  $\mathcal{N} = 4$  SYM theory at the boundary we turn to the thermodynamic properties of this set-up. The expression for the temperature can be found by considering the relevant terms of the metric close to the horizon after euclidean continuation

$$ds^2 = \frac{e^{-\phi_h/2}}{u_h^2} \left( |\mathcal{F}_1| \mathcal{B}_h(u_h - u) dt_E^2 + \frac{du^2}{|\mathcal{F}_1|(u_h - u)} \right), \quad (2.24)$$

where  $\mathcal{F}_1 = \mathcal{F}'(u_h)$  is negative. We can introduce new coordinates to bring the line element into the form  $ds^2 = d\rho^2 + \rho^2 d\vartheta^2$ . This new coordinates are then related to

---

<sup>3</sup>Here  $\theta = 2\pi\hat{\chi}$ ,  $\chi = g_s\hat{\chi}$  and  $a = g_s n_{D7}$ . The rescaling by  $g_s$  comes from our choice that  $\phi_{bdry} = 0$ , which can be achieved by defining  $e^\varphi = g_s e^\phi$  and  $F_n = g_s \hat{F}_n$  and similarly for all other hatted variables. Note that  $\varphi$  determines the string coupling  $g_s = e^{\varphi_{bdry}}$ . Finally, we mention that the number of D7-branes  $N_{D7} = \int d\hat{\chi}$  is measured by the circulation of  $\hat{\chi}$  around them.

$(t_E, u)$  by

$$\rho = \frac{2e^{-\phi_h/4}}{u_h} \sqrt{\frac{u_h - u}{|\mathcal{F}_1|}} \quad \text{and} \quad \vartheta = \frac{|\mathcal{F}_1| \sqrt{\mathcal{B}_h} t_E}{2}. \quad (2.25)$$

From the requirement that  $\vartheta \cong \vartheta + 2\pi$  we find that  $t_E \cong t_E + \delta t_E$  such that

$$T = \frac{1}{\delta t_E} = \frac{|\mathcal{F}_1| \sqrt{\mathcal{B}_h}}{4\pi}. \quad (2.26)$$

It is also a straightforward task to find the entropy density per unit volume in the  $xyz$ -directions

$$s = \frac{A_h}{4GV_3} = \frac{N_c^2}{2\pi u_h^3} e^{-\frac{5\phi_h}{4}}. \quad (2.27)$$

In an isotropic plasma with  $a = 0$  the functions in the metric are given by

$$\phi = 0, \quad \mathcal{B} = \mathcal{H} = 1, \quad \mathcal{F} = 1 - \frac{u^4}{u_h^4}, \quad \text{with } u_h = \frac{1}{\pi T} \quad (2.28)$$

and then eq. (2.27) gives the well known result for the entropy density in an  $\mathcal{N} = 4$  SYM plasma

$$s^0(T) = \frac{\pi^2}{2} N_c^2 T^3. \quad (2.29)$$

In the limit of  $a \gg T$  the entropy density scales differently [59, 60]

$$s = c_{ent} = N_c^2 a^{\frac{1}{3}} T^{\frac{8}{3}}, \quad (2.30)$$

with  $c_{ent} \approx 3.2$  being a numerical coefficient obtained in [59].

### The stress-energy tensor

Next, we want to calculate the holographic stress-energy tensor. This is complicated by large-volume divergencies in the action that must be subtracted consistently by holographic renormalization. The renormalization procedure extended to general axion-dilaton gravity duals is discussed in [63]. The counterterm we eventually have to add to the bulk action is

$$S_{c.t.} = -\frac{1}{\kappa^2} \int d^4x \sqrt{\gamma} \left( 3 - \frac{e^{2\phi}}{8} (\partial\chi)^2 \right) + \ln v \int d^4x \sqrt{\gamma} \mathcal{A} - \frac{c_{sch} - 1}{4} \int d^4x \sqrt{\gamma} \mathcal{A}. \quad (2.31)$$

Here  $\gamma_{\mu\nu}$  is the induced metric on the boundary with euclidean signature. Note that since we are interested in the thermodynamics of the system it is convenient to work in euclidean spacetime.  $\mathcal{A}$  is the conformal anomaly in the axion-dilaton gravity system and finally,  $v$  is the standard Fefferman-Graham coordinate. The logarithmic term in eq. (2.31) is needed to cancel divergencies in the bulk action. However, it also breaks diffeomorphism invariance in the bulk and is therefore the origin of the conformal anomaly in the boundary theory. This will introduce an additional reference scale  $\mu$  in the theory and the physics will not only depend on  $a/T$  but on  $a/\mu$  and  $T/\mu$  separately. The third term in eq. (2.31) is finite and represents the freedom in the choice of renormalization scheme. Shifts of  $c_{sch}$  are precisely equivalent to rescaling of the reference scale  $\mu$  [59].

Expanding the functions in the metric near the boundary gives

$$\phi = -\frac{a^2}{4}v^2 + \left(\frac{2\mathcal{B}_4}{7} - \frac{47a^4}{4032}\right)v^4 - \frac{a^4}{6}v^4 \ln v + \mathcal{O}(v^6), \quad (2.32)$$

$$\mathcal{F} = 1 + \frac{11a^2}{24}v^2 + \left(\mathcal{F}_4 + \frac{11a^4}{144}\right)v^4 + \frac{7a^4}{12}v^4 \ln v + \mathcal{O}(v^6), \quad (2.33)$$

$$\mathcal{B} = 1 - \frac{11a^2}{24}v^2 + \left(\mathcal{B}_4 - \frac{11a^4}{144}\right)v^4 - \frac{7a^4}{12}v^4 \ln v + \mathcal{O}(v^6), \quad (2.34)$$

$$\mathcal{H} = 1 + \frac{a^2}{4}v^2 - \left(\frac{2\mathcal{B}_4}{7} - \frac{173a^4}{4032}\right)v^4 + \frac{a^4}{6}v^4 \ln v + \mathcal{O}(v^6). \quad (2.35)$$

The coefficients  $\mathcal{B}_4(a, T)$  and  $\mathcal{F}_4(a, T)$  are not determined by the asymptotic equations of motion but can be read off numerically for a particular solution. We present our numerical approach in appendices D.2.2 and D.2.3. In fact  $\mathcal{B}_4$  and  $\mathcal{F}_4$  are the coefficients of the  $\mathcal{O}(u^4)$  terms in the near boundary expansion of the functions  $\mathcal{B}$  and  $\mathcal{F}$  in the  $u$ -coordinate. The precise relation between  $v$  and  $u$  can be found in [59]. Making use of the results of [63] we can then read off the stress-energy tensor  $\langle T_{\mu\nu} \rangle = \text{diag}(\epsilon, P_\perp, P_\perp, P_z)$  with

$$\epsilon = \frac{N_c^2}{2\pi^2} \left( -\frac{3}{4}\mathcal{F}_4 - \frac{23}{28}\mathcal{B}_4 + \frac{2777}{16128}a^4 + \frac{c_{sch}}{96}a^4 \right), \quad (2.36)$$

$$P_\perp = \frac{N_c^2}{2\pi^2} \left( -\frac{1}{4}\mathcal{F}_4 - \frac{5}{28}\mathcal{B}_4 + \frac{611}{16128}a^4 - \frac{c_{sch}}{96}a^4 \right), \quad (2.37)$$

$$P_z = \frac{N_c^2}{2\pi^2} \left( -\frac{1}{4}\mathcal{F}_4 - \frac{13}{28}\mathcal{B}_4 + \frac{2777}{16128}a^4 + \frac{c_{sch}}{96}a^4 \right). \quad (2.38)$$

In Fig. 2.2 the energy density and the pressures are shown for increasing anisotropy and fixed position of the horizon  $u_h = 2$ . For small values of  $a/T$  we encounter an oblate pressure anisotropy while it then becomes isotropic and increasingly prolate as we further increase  $a/T$ . We note that keeping  $u_h$  fixed does only approximately correspond to fixed temperature, since the temperature also weakly depends on the

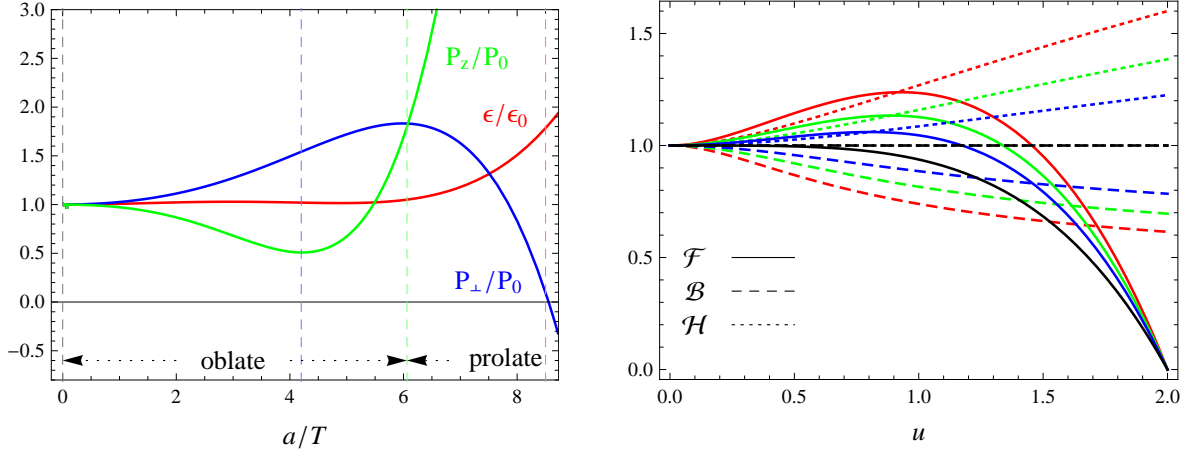


Figure 2.2: In the left plot the energy density and the longitudinal and transverse pressure normalized to the isotropic Stefan-Boltzmann values  $\epsilon_0 = 3\pi^2 N_c^2 T^4/8$  and  $P_0 = \pi^2 N_c^2 T^4/8$  are shown for  $u_h = 2$ ,  $\mu = 1$  and  $c_{sch} = -1$ . This corresponds to a temperature that varies from  $T \approx 1.59$  to  $T \approx 1.75$  with increasing  $a/T$ . To the right we plot the functions  $\mathcal{F}$ ,  $\mathcal{B}$ , and  $\mathcal{H}$  for different values of  $a/T$  indicated by the vertical dashed lines with the same color in the left plot.

value of the dilaton at the horizon. It is remarkable that the metric functions  $\mathcal{F}$ ,  $\mathcal{B}$ , and  $\mathcal{H}$  change monotonically as we increase the anisotropy parameter  $a$  without a qualitative change when the pressure anisotropy changes from oblate to prolate, which is in stark contrast to the JW model.

We can also find expressions for the expectation values of operators dual to  $\phi$ ,  $\mathcal{O}_\phi \sim \text{Tr} F^2$ , and  $\chi$ ,  $\mathcal{O}_\chi \sim \text{Tr} F \tilde{F}$  and the trace and divergence of the stress energy tensor [63]

$$\partial^\mu \langle T_{\mu\nu} \rangle + \langle \mathcal{O}_\phi \rangle \partial_\nu \phi_{(0)} + \langle \mathcal{O}_\chi \rangle \partial_\nu \chi_{(0)} = 0, \quad (2.39)$$

$$\langle T_\mu^\mu \rangle = \mathcal{A}(g_{\mu\nu}^{(0)}, \phi_{(0)}, \chi_{(0)}) = \frac{1}{12\kappa^2} \left( g_{(0)}^{\mu\nu} \partial_\mu \chi_{(0)} \partial_\nu \chi_{(0)} \right). \quad (2.40)$$

For the case at hand with  $\phi = \phi(u)$  and  $\chi = az$  it turns out that  $\langle \mathcal{O}_\chi \rangle = 0$  and  $\partial_\mu \phi_{(0)} = 0$  which implies conservation of the stress energy tensor  $\partial^\mu \langle T_{\mu\nu} \rangle = 0$ . For the trace anomaly we find

$$\langle T_\mu^\mu \rangle = \frac{N_c^2 a^4}{48\pi^2}. \quad (2.41)$$

### Thermodynamic functions

After we have obtained the stress-energy tensor from the gravity dual we now discuss the various thermodynamic functions of interest to us (see also [59, 47]). We

will do this in full generality for later convenience when we also take a look at the boundary theory at zero coupling. Energy is a function of extensive variables,  $E = E(S, N, L_\perp, L_z)$ , where instead of  $N_{D7}$  we have written only  $N$  and refer to it as the number of charges that cause the anisotropy of the system<sup>4</sup>. Pressures in various directions are most naturally expressed in terms of energy, and are given by

$$P_\perp = -\frac{1}{L_z} \left( \frac{\partial E}{\partial L_\perp^2} \right)_{S, N, L_z}, \quad P_z = -\frac{1}{L_\perp^2} \left( \frac{\partial E}{\partial L_z} \right)_{S, N, L_\perp}. \quad (2.42)$$

A more convenient quantity to compute, however, is the Helmholtz free energy,  $F = F(T, N, L_\perp, L_z) \equiv E - TS = Vf(T, a)$ . It can be obtained in field theory from the partition function

$$F = -T \ln \mathcal{Z}_{part}. \quad (2.43)$$

and along the lines of holographic duality from the on-shell action

$$S_{o.s.} = \beta \int d^3x f, \quad (2.44)$$

with  $\beta = 1/T$ . From the definitions of pressures in eq. (2.42) and the relation between  $F$  and  $E$ , we immediately find that the pressures are given by

$$P_\perp = -\frac{1}{L_z} \left( \frac{\partial F}{\partial L_\perp^2} \right)_{T, N, L_z} = -\frac{1}{L_z} \left( \frac{\partial F}{\partial L_\perp^2} \right)_{T, a} = -f \quad (2.45)$$

$$\begin{aligned} P_z &= -\frac{1}{L_\perp^2} \left( \frac{\partial F}{\partial L_z} \right)_{T, N, L_\perp} = -f - L_z \left( \frac{\partial f}{\partial L_z} \right)_{T, N} \\ &= -f + a \left( \frac{\partial f}{\partial a} \right)_T. \end{aligned} \quad (2.46)$$

Note that even though our physical system is inherently anisotropic as soon as  $a \neq 0$  (with e.g. anisotropic relations between energies and momenta of its particles), the pressure would be necessarily isotropic in thermal equilibrium if  $a$  were not react differently to changing the system size along different directions.

We can also study the system in the grand canonical ensemble, as a function of the chemical potential  $\mu \equiv \partial F / \partial N$  conjugate to the number  $N$  of the charges causing the anisotropy. The associated free energy, the grand potential, is given by

$$G \equiv F - N \left( \frac{\partial F}{\partial N} \right)_{T, L_\perp, L_z} = V \left[ f - a \left( \frac{\partial f}{\partial a} \right)_T \right]. \quad (2.47)$$

---

<sup>4</sup>In our notation  $\epsilon$  is the energy density that is related to the actual energy of the system by  $E = \epsilon \cdot V$ .



The grand potential has the general form  $G(T, \mu, L_\perp, L_z) = Vg(T, \mu/L_\perp^2)$ , which is easy to see from above as follows. Defining<sup>5</sup>  $\Phi \equiv \partial f / \partial a$ , it is clear by construction that the grand potential can be written as  $G = Vg(T, \Phi)$  with  $g(T, \Phi) = f - a\partial_a f$ . On the other hand, we have

$$\mu \equiv V \left( \frac{\partial f}{\partial N} \right)_{T,L} = L_\perp^2 \left( \frac{\partial f}{\partial a} \right)_T = L_\perp^2 \Phi, \quad (2.48)$$

and thus  $\Phi = \mu/L_\perp^2$  and  $G = Vg(T, \mu/L_\perp^2)$ . In terms of the grand potential, the pressures can then be written as

$$P_\perp = -\frac{1}{L_z} \left( \frac{\partial G}{\partial L_\perp^2} \right)_{T,\mu,L_z} = -g - L_\perp^2 \left( \frac{\partial g}{\partial L_\perp^2} \right)_{T,\mu} \quad (2.49)$$

$$= -g + \Phi \left( \frac{\partial g}{\partial \Phi} \right)_T, \quad (2.50)$$

$$P_z = -\frac{1}{L_\perp^2} \left( \frac{\partial G}{\partial L_z} \right)_{T,\mu,L_\perp} = -\frac{1}{L_\perp^2} \left( \frac{\partial G}{\partial L_z} \right)_{T,\Phi} = -g. \quad (2.51)$$

Instead of working with  $F$  and  $G$ , which are functions of conjugate variables  $N$  and  $\mu$ , respectively, it is more convenient to consider the free energy densities  $f$  and  $g$ , which are functions of the conjugate variables  $a$  (number of charges per unit length) and  $\Phi$  (chemical potential per unit transverse area), respectively.

Before we move to discussing the phase diagram at infinite coupling, we reproduce analytical results for thermodynamic quantities in the high temperature limit  $T \gg a, \mu$  and the opposite limit  $T \ll a, \mu$  for completeness, but refer the reader to the original work [59] for details. Omitting terms of  $\mathcal{O}(a^6)$  for  $T \gg a, \mu$  we find

$$\epsilon = \epsilon_0(T) + \frac{N_c^2 T^2 a^2}{32} + \frac{N_c^2 a^4}{1536\pi^2} \left[ 8c_{sch} - 41 - 32 \ln \frac{a}{2\pi T} \right] + \frac{N_c^2 a^4}{48\pi^2} \ln \frac{a}{\mu}, \quad (2.52)$$

$$P_\perp = P_0(T) + \frac{N_c^2 T^2 a^2}{32} + \frac{N_c^2 a^4}{1536\pi^2} \left[ -8c_{sch} + 9 + 32 \ln \frac{a}{2\pi T} \right] - \frac{N_c^2 a^4}{48\pi^2} \ln \frac{a}{\mu}, \quad (2.53)$$

$$P_z = P_0(T) - \frac{N_c^2 T^2 a^2}{32} + \frac{N_c^2 a^4}{512\pi^2} \left[ 8c_{sch} - 9 - 32 \ln \frac{a}{2\pi T} \right] + 3 \frac{N_c^2 a^4}{48\pi^2} \ln \frac{a}{\mu}, \quad (2.54)$$

$$\Phi = -\frac{N_c^2 T^2 a^2}{16} + \frac{N_c^2 a^3}{384\pi^2} \left[ 8c_{sch} - 9 - 32 \ln \frac{a}{2\pi T} \right] + 4 \frac{N_c^2 a^3}{48\pi^2} \ln \frac{a}{\mu}, \quad (2.55)$$

---

<sup>5</sup>In the infinite coupling case the chemical potential  $\Phi$  can be also read off from the asymptotic behavior of an RR 8-form coming from the D7 branes. In order for this to coincide with the thermodynamic definition it is necessary to choose  $c_{sch} = -1$ . Details can be found in [59].

while in the other limit we get

$$\epsilon = \frac{N_c^2 a^4}{5376\pi^2} (28c_{sch} - 1 + 192c_{int}) + \frac{N_c^2 a^4}{48\pi^2} \ln \frac{a}{\mu} + \frac{8c_{ent} N_c^2 a^{1/3} T^{11/3}}{11}, \quad (2.56)$$

$$P_\perp = -\frac{N_c^2 a^4}{5376\pi^2} (28c_{sch} - 1 + 192c_{int}) - \frac{N_c^2 a^4}{48\pi^2} \ln \frac{a}{\mu} + \frac{3c_{ent} N_c^2 a^{1/3} T^{11/3}}{11}, \quad (2.57)$$

$$P_z = \frac{N_c^2 a^4}{5376\pi^2} (84c_{sch} + 109 + 576c_{int}) + 3\frac{N_c^2 a^4}{48\pi^2} \ln \frac{a}{\mu} + \frac{2c_{ent} N_c^2 a^{1/3} T^{11/3}}{11}, \quad (2.58)$$

$$\Phi = \frac{N_c^2 a^3}{1344\pi^2} (28c_{sch} + 27 + 192c_{int}) + \frac{N_c^2 a^3}{12\pi^2} \ln \frac{a}{\mu} - \frac{c_{ent} N_c^2 T^{11/3}}{11a^{2/3}}, \quad (2.59)$$

where we omitted higher order terms in  $T/a$ . The constants  $c_{int}$  and  $c_{ent}$  must be determined numerically.

### Phase diagram

Finally, we discuss the phase diagram of the anisotropic plasma in the infinitely strong coupling limit. We emphasize that the system we consider contains a fixed number  $N$  of charges (here D7 branes). The way these charges are distributed along the  $z$ -axis is a free parameter determined by minimizing the free energy  $F$ . Throughout this work we are going to refer to these various distributions as various phases of the system. For simplicity, we only consider distributions which consist of homogeneous regions of finite extent with various charge densities  $a$ . We refer to the phase with only one region as homogeneous phase and the phase with two or more regions as inhomogeneous phase. The boundary between regions in the inhomogeneous phase must be perpendicular to the  $z$ -axis, because  $a$  can only vary in  $z$ -direction.

Besides the thermodynamically unstable phase, where infinitely small charge fluctuations can lower the free energy, there may also exist a metastable phase. In this phase finite charge fluctuations are required for the transition to the inhomogeneous phase.

In order for two homogeneous regions to exist next to each other the intensive thermodynamic variables must have the same values in each region. Therefore the longitudinal pressure  $P_z$  has to have the same value in each region<sup>6</sup> (“mechanical equilibrium”) and the same is true for the chemical potential  $\Phi$  (“chemical equilibrium”) as long as each region contains a non-zero number of charges so that processes taking charges from one region to another can remain in equilibrium. If the other region is isotropic ( $a = 0$ ) there are no charges and therefore no charges can be transferred from there to the other region. In that case chemical equilibrium cannot be reached.

---

<sup>6</sup>Since the boundary between two regions can only be perpendicular to the  $z$ -axis, we do not need to require equality of the transverse pressures.

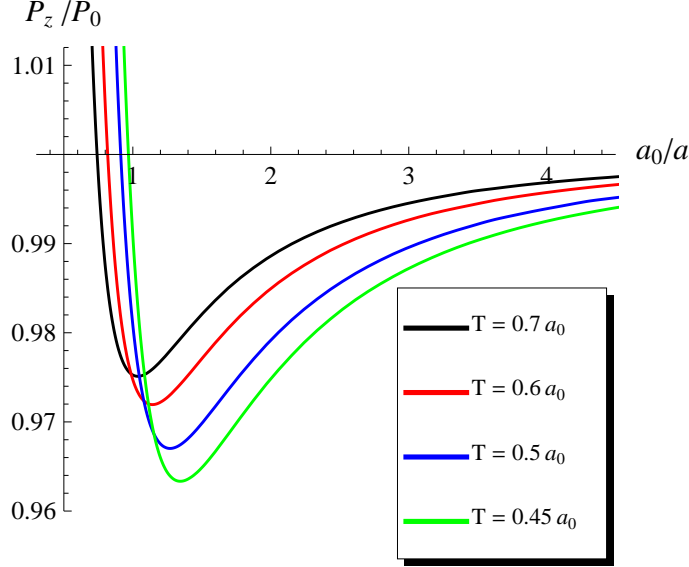


Figure 2.3: Longitudinal pressure as a function of  $1/a$  for various temperatures at strong coupling normalized to the Stefan-Boltzmann pressure. The temperature and the charge density are given in units of charge density  $a_0 \approx 1.27\mu$ . This scale is defined by  $f(T = 0, a_0) = 0$  and simplifies the comparison with the results at zero coupling.

It is well known that homogeneous phases violating

$$\left(\frac{\partial P_z}{\partial L_z}\right)_{T,N} < 0 \quad \Rightarrow \quad \left(\frac{\partial P_z}{\partial(1/a)}\right)_T < 0 \quad (2.60)$$

are unstable and cannot exist in equilibrium. Using eq. (2.46) we can rewrite the above conditions equally well as

$$\left(\frac{\partial^2 f}{\partial^2 a}\right)_T = \left(\frac{\partial \Phi}{\partial a}\right)_T > 0. \quad (2.61)$$

In Fig. 2.3 we plot the longitudinal pressure as a function of  $1/a$ . This corresponds to the well known pressure-volume plots that indicate the unstable regions in a phase diagram. We note that for small  $a$  the longitudinal pressure is a monotonically increasing function of  $1/a$  irrespectively of the temperature. This can also be seen from the analytical high and low temperature limits eqs. (2.55) and (2.59). For small enough  $a$  condition (2.61) is always violated. This has interesting consequences, namely that in the strong coupling limit infinitely small densities of D7 branes are thermodynamically unstable with respect to a redistribution of the branes in  $z$ -direction. Only for a finite  $a$  we obtain metastable and stable phases. This also requires that there are always isotropic ( $a = 0$ ) regions present in the inhomogeneous phase.

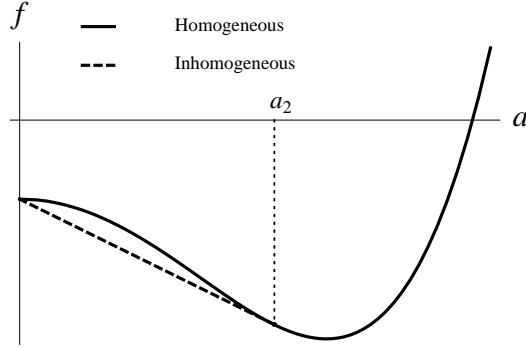


Figure 2.4: Condition for coexistence of isotropic and anisotropic regions at strong coupling. The dashed line, giving the free energy of the inhomogeneous phase, is the tangent to  $f(T, a)$  at  $a = a_2$  and coincides with  $f(T, a)$  at  $a = 0$ .

If one region is isotropic e.g.  $a_1 = 0$  and a second region has a finite charge density  $a_2$  then chemical equilibrium cannot be reached. We are left with the condition that the longitudinal pressures have to be the same

$$f(T, a_2) - a_2 \Phi(T, a_2) = f(T, 0). \quad (2.62)$$

In Fig. 2.4 this condition is presented graphically. The dashed line drawn from  $(0, f(T, 0))$  to  $(a_2, f(T, a_2))$  is tangent to  $f(T, a)$  at  $a = a_2$ . Since  $\partial^2 f / \partial^2 a|_{a=0} < 0$ , the dashed line is always below  $f(T, a)$  and therefore the free energy of the inhomogeneous phase with regions having  $a = 0$  and  $a = a_2$  is lower than that of the homogeneous phase with corresponding overall density.

Our numerical result for the full phase diagram is shown in Fig. 2.5 and agrees with the qualitative sketch given in [59]. Even though it cannot be seen in the plot we checked that all four lines start out strictly vertical in the zero temperature limit and then the red dashed line and the black line bend to the left for small temperatures and the other two bend to the right. This behavior can also be anticipated from the analytical expressions in the low  $T$  limit eqs. (2.56)-(2.59). For any curve  $\mathcal{X}$  (where  $\mathcal{X}$  can be  $f$ ,  $P_z$ ,  $\Phi$  or  $\partial\Phi/\partial a$ ) in the phase diagram we can define the tangent vector  $(n_a, n_T)$ . By definition along the curve the derivative of  $\mathcal{X}$  vanishes

$$n_a \frac{\partial \mathcal{X}}{\partial a} + n_T \frac{\partial \mathcal{X}}{\partial T}. \quad (2.63)$$

Starting at  $T = 0$  we have  $n_T > 0$  and

$$n_a = \left( \frac{\partial \mathcal{X}}{\partial T} \right) \left( \frac{\partial \mathcal{X}}{\partial a} \right)^{-1} n_T. \quad (2.64)$$

At  $T = 0$  we find that  $n_a$  has to vanish for all four curves and at low temperatures the respective curves behave as explained above. More details for  $\mathcal{X} = \Phi$  at low temperature are given in [59].

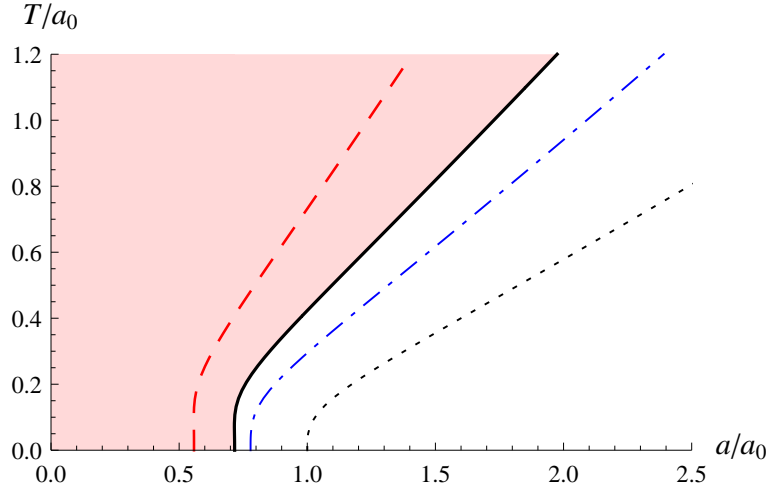


Figure 2.5: The phase diagram at strong coupling. The solid line separates the homogeneous and inhomogeneous (red shaded region) phases. The red dashed line indicates the region where the homogeneous phase is unstable. The blue dash-dotted line indicates  $\Phi = 0$ . For smaller  $a/a_0$  the pressure anisotropy is oblate otherwise it is prolate. To the left of the dotted line  $f(a, T) < f(0, T)$ .

Before considering the boundary gauge theory at zero coupling we briefly summarize our findings at infinite coupling

- For small enough charge densities  $a$  we always encounter a thermodynamically unstable region followed by a metastable phase when we increase  $a$ . There the D7 branes redistribute along the  $z$ -direction such that there are stacks with  $a = 0$  and stacks with a larger  $a$ . Eventually for large enough charge densities we end up in a stable homogeneous phase. This behavior is qualitatively the same for all temperatures.
- Increasing the charge density we at first encounter an oblate pressure anisotropy. Then the plasma has equal pressures in longitudinal and transverse direction at some intermediate  $a$  and thereafter becomes increasingly prolate for larger charge densities.
- For both the unstable and metastable phase the “would be” homogeneous pressure anisotropy is oblate and it decays into an inhomogeneous phase where there are isotropic stacks with no charge density and oblate stacks with a larger charge density. While the homogeneous phase is trivially in chemical equilibrium the inhomogeneous system it decays into is not.

### 2.2.3 Boundary theory at zero coupling

#### Setup and notation

After reviewing the thermodynamics of anisotropically  $\theta$ -deformed gauge theory at infinite coupling we want to contrast the results with what we find for the same theory at zero coupling [47]. The deformation we need to consider is

$$\delta S = \int d^4x \frac{az}{g_{YM}^2} \text{Tr } F \wedge F. \quad (2.65)$$

As we are only interested in the zero coupling limit we are essentially studying a theory of free photons and can therefore neglect the gauge group indices in the following. Absorbing  $g_{YM}$  in  $F$  by rescaling we obtain the following modified Yang-Mills Lagrangian

$$\mathcal{L} = \mathcal{L}_{YM} - \frac{1}{4} \tilde{\theta}(x) \epsilon^{\mu\nu\rho\sigma} F_{\mu\nu} F_{\rho\sigma}, \quad (2.66)$$

where  $\mathcal{L}_{YM} = -\frac{1}{4} F_{\mu\nu} F^{\mu\nu} - \frac{1}{2} (\partial_\mu A^\mu) + (\text{ghosts})$ . By partially integrating we can rewrite the Lagrangian

$$\mathcal{L} = \mathcal{L}_{YM} + \frac{1}{4} j(x) \epsilon^{\mu\nu\rho\sigma} A_\mu F_{\nu\rho} \zeta_\sigma \quad (2.67)$$

with  $\partial_\sigma \tilde{\theta}(x) = j(x) \zeta_\sigma$ . The theory we consider contains a source  $j(x)$  that is coupled to a homogeneous but anisotropic 2+1 dimensional Chern-Simons operator  $\epsilon^{\mu\nu\rho\sigma} A_\mu F_{\nu\rho} \zeta_\sigma$ , with the 2+1 dimensional subspace being specified by  $\zeta_\sigma$ . Furthermore, the charges that couple to  $\epsilon^{\mu\nu\rho\sigma} A_\mu F_{\nu\rho} \zeta_\sigma$  can only be localized in the  $\zeta$ -direction,  $j(x) = j(x_\mu \zeta^\mu)$  because of gauge invariance. A similar Chern-Simons deformation of electrodynamics has been considered in [64]. There the  $\zeta^\mu$  parameter is timelike and therefore the model is isotropic but violates Lorentz and CPT symmetry. A drawback of a theory with a timelike gradient of  $\theta$  is that tachyonic modes appear. However, these modes are absent for theories with a spacelike  $\theta$  gradient [65, 66].

To make contact with the MT model at strong coupling we choose the charge density to be constant and make the identification

$$j(z) = a \equiv \frac{N}{L_z}. \quad (2.68)$$

Here,  $N$  is the number of charges coupling to the Chern-Simons operator (in the infinite coupling case this was the number of D7 branes) and  $L_z$  the extent of the system in  $\zeta$ -direction, which we have chosen to be the  $z$ -direction. Denoting the linear extent of the system perpendicular to the  $z$ -direction as  $L_\perp$ , the volume is then  $V = L_\perp^2 L_z$ .

The partition function is given by the Euclidean path integral<sup>7</sup>

$$\mathcal{Z}(T, j) = \int \mathcal{D}A_\mu \exp \left[ - \int_0^\beta d\tau \int d^3x \left( \mathcal{L}_{YM}^e + \frac{i}{4} j(x) \epsilon_{\mu\nu\rho\sigma} A_\mu F_{\nu\rho} \zeta_\sigma + \Omega \right) \right]. \quad (2.69)$$

Here the  $\mathcal{L}_{YM}^e = \frac{1}{4} F_{\mu\nu} F_{\mu\nu} + \frac{1}{2} (\partial_\mu A_\mu) + (\text{ghosts})$  and  $\Omega$  is the cosmological constant that is needed for renormalization.

In this section and in appendix E we use the notation  $K^2 = k_\mu k_\mu = k_0^2 + \mathbf{k}^2 = k_0^2 + k_\perp^2 + k_z^2$  for momenta. We renormalize the theory in dimensional regularization by splitting the spacetime into  $\mathbb{R}^3 \times \mathbb{R}^{1-2\epsilon}$  (“transverse”  $\times$  “longitudinal”), with the Chern-Simons term taking the form  $\epsilon_{ijk} A_i F_{jk}$  with  $\{i, j, k\}$  labeling the transverse directions (including Euclidean time). Additionally, we label the longitudinal directions with letters from the beginning of the Greek alphabet,  $\alpha, \beta, \dots$ , leaving  $\mu, \nu, \dots$  to label directions in the entire spacetime.

Our notation for momentum integrations is such that

$$\int_k = \int_{k_z} \int \frac{d^2 k_\perp}{(2\pi)^2} = \left( \frac{e^\gamma \bar{\Lambda}^2}{4\pi} \right)^\epsilon \int \frac{d^{1-2\epsilon} k_z}{(2\pi)^{1-2\epsilon}} \frac{d^2 k_\perp}{(2\pi)^2}, \quad (2.70)$$

$$\oint_K =_T \sum_{k_0} \int_k. \quad (2.71)$$

## Computation of the free energy

In the presence of the source  $j(z) = a$ , the path integral in eq. (2.69) can be carried out immediately with the result

$$\mathcal{Z}(T, a) = e^{-\beta V \Omega} \frac{\det_K(\Delta^{-1}(K))}{\sqrt{\det_{\mu\nu, K}(D_{\mu\nu}^{-1}(K))}}, \quad (2.72)$$

where the inverse photon and ghost propagators are given in momentum space by

$$D_{\alpha\beta}^{-1}(K) = \beta^2 K^2 \delta_{\alpha\beta}, \quad (2.73)$$

$$D_{ij}^{-1}(K) = \beta^2 [K^2 \delta_{ij} - a \epsilon_{ijk} k_k], \quad (2.74)$$

$$D_{i\alpha}^{-1}(K) = D_{\alpha i}^{-1}(K) = 0, \quad (2.75)$$

$$\Delta^{-1}(K) = \beta^2 K^2. \quad (2.76)$$

---

<sup>7</sup>In Euclidean spacetime, we write all the Lorentz indices as subscripts to distinguish it from Minkowski spacetime.

The determinant of the inverse photon propagator over the Lorentz indices is given by

$$\begin{aligned} \|D_{\mu\nu}^{-1}\| &= (\beta^2 K^2)^{1-2\epsilon} \beta^6 K^2 [K^4 + (K^2 - k_z^2) a^2] \\ &= (\beta^2)^{4-2\epsilon} (K^2)^{2-2\epsilon} \prod_{\pm} \left( K^2 + \frac{a^2 \pm \sqrt{a^4 + 4a^2 k_z^2}}{2} \right). \end{aligned} \quad (2.77)$$

It can immediately be seen that the ghost contribution cancels the contribution from the two  $a$ -independent photon modes. The logarithm of the partition function can thus be written as

$$\ln \mathcal{Z}(T, a) = -\frac{\beta V}{2} \oint_K \sum_{\pm} \ln (\beta^2 k_0^2 + \beta^2 (k_{\perp}^2 + M_{\pm}^2(k_z))) - \beta V \Omega, \quad (2.78)$$

where

$$M_{\pm}^2(k_z) = k_z^2 + \frac{a^2 \pm \sqrt{a^4 + 4a^2 k_z^2}}{2}, \quad (2.79)$$

or, equivalently,

$$M_{\pm}(k_z) = \sqrt{k_z^2 + a^2/4} \pm \frac{a}{2}. \quad (2.80)$$

Note that in Minkowski space ( $k_0 \rightarrow i\omega$ ) we have photon modes that for nonzero  $k_z$  split into modes with  $\omega_+^2 > \mathbf{k}^2 = k_{\perp}^2 + k_z^2$  and ones with  $\omega_-^2 < \mathbf{k}^2$ . However, also the latter are non-tachyonic since  $\omega_-^2 \geq 0$ .

Using

$$\begin{aligned} \sum_{n=-\infty}^{\infty} \partial_{x^2} \ln(4\pi^2 n^2 + x^2) &= \sum_{n=-\infty}^{\infty} \frac{1}{4\pi^2 n^2 + x^2} = \frac{1}{2x} \left[ 1 + \frac{2}{e^x - 1} \right] \\ &= \partial_{x^2} [x + 2 \ln(1 - e^{-x})] \end{aligned} \quad (2.81)$$

$$\Rightarrow \sum_{n=-\infty}^{\infty} \ln(4\pi^2 n^2 + x^2) = x + 2 \ln(1 - e^{-x}) + \text{constant}, \quad (2.82)$$

we get for the Helmholtz free energy density  $f = -T/V \ln \mathcal{Z}$  (with the constant absorbed into the cosmological constant)

$$f(T, a) = \Omega + T \sum_{\pm} \int_k \left[ \frac{1}{2} \beta \omega_{\pm} + \ln(1 - e^{-\beta \omega_{\pm}}) \right], \quad (2.83)$$

where

$$\omega_{\pm}^2 = k_{\perp}^2 + M_{\pm}^2(k_z). \quad (2.84)$$



The details of the computations at zero and finite temperature can be found in [47] and are reproduced in appendix E.

The  $T = 0$  limit of eq. (2.83) contains a UV-divergence that needs to be renormalized. In the  $\overline{MS}$ -scheme, we obtain

$$f(0, a) = -\frac{c a^4}{12\pi^2} + \frac{5a^4}{256\pi^2} \ln \frac{a}{\bar{\Lambda}} + \Omega(\bar{\Lambda}), \quad (2.85)$$

where

$$c = \int_0^\infty dx \left[ \left( x^2 + \frac{1}{2}(1 + \sqrt{1 + 4x^2}) \right)^{3/2} + \left( x^2 + \frac{1}{2}(1 - \sqrt{1 + 4x^2}) \right)^{3/2} - 2x^3 - \frac{9}{4}x - \frac{15}{64\sqrt{1 + x^2}} \right] = 0.29136 \dots \quad (2.86)$$

and  $\Omega(\bar{\Lambda})$  is the renormalized cosmological constant running with the scale  $\bar{\Lambda}$ . However, since we want to explore the thermodynamics as a function of  $a$  at some fixed but arbitrary scale  $\bar{\Lambda}$ , we are free to choose the value of the cosmological constant (which is by definition independent of  $a$ ) at that scale. With this in mind, fixing  $\bar{\Lambda}$  to give units  $a$  is measured in, we set  $\Omega = 0$ , yielding for the  $T = 0$  free energy

$$f(0, a) = -\frac{c a^4}{12\pi^2} + \frac{5a^4}{256\pi^2} \ln \frac{a}{\bar{\Lambda}}. \quad (2.87)$$

The coefficient in front of the logarithm gives the trace anomaly of our system

$$\epsilon - 2P_\perp - P_z = -\frac{5a^4}{256\pi^2}. \quad (2.88)$$

It turns out that this is curiously close to the infinite-coupling result which equals  $-a^4/48\pi^2$ .

We are still free to choose the renormalization scale. A convenient way to do this is to express the scale  $\bar{\Lambda}$  in terms of  $a_0$ ,

$$\ln \frac{a_0}{\bar{\Lambda}} = \frac{64c}{15} \quad (2.89)$$

such that

$$f(0, a) = \frac{5a^4}{256\pi^2} \ln \frac{a}{a_0}. \quad (2.90)$$

As before for infinite coupling  $a_0$  is the finite charge density for which the energy density vanishes. In the following we express everything in this section in terms of the scale  $a_0$ .

Other thermodynamic variables of interest at  $T = 0$  can now be computed,

$$\Phi = \frac{\partial f}{\partial a} = \frac{5a^3}{256\pi^2} \left( 1 + 4 \ln \frac{a}{a_0} \right), \quad (2.91)$$

$$P_z = -f + a\Phi = \frac{5a^4}{256\pi^2} \left( 1 + 3 \ln \frac{a}{a_0} \right), \quad (2.92)$$

$$\Phi' = \frac{\partial \Phi}{\partial a} = \frac{5a^2}{256\pi^2} \left( 7 + 12 \ln \frac{a}{a_0} \right). \quad (2.93)$$

Respectively, they vanish at different densities  $a$  given by

$$a_\Phi = a_0 e^{-1/4} \approx 0.7788 a_0, \quad (2.94)$$

$$a_{P_z} = a_0 e^{-1/3} \approx 0.7165 a_0, \quad (2.95)$$

$$a_{\Phi'} = a_0 e^{-7/12} \approx 0.5580 a_0. \quad (2.96)$$

The finite- $T$  contribution is given by

$$f(T, a) - f(0, a) = T \sum_{\pm} \int_k \ln (1 - e^{-\beta\omega_{\pm}}). \quad (2.97)$$

Unfortunately, it is not possible to express this sum-integral in a closed form. We can, however, derive a simpler integral representation for the finite- $T$  contribution that is straightforward to evaluate numerically (see [47] and appendix E.2 for details),

$$f(T, a) - f(0, a) = \frac{T^4}{2\pi^2} \sum_{\pm} \int_0^{\infty} dx x^2 \left( 1 \pm \frac{y}{\sqrt{x^2 + y^2}} \right) \ln (1 - e^{-\sqrt{x^2 + y^2} \mp y}), \quad (2.98)$$

where  $y = a/(2T)$ . The integral in (2.98) is of the same form as integrals encountered in the thermodynamics of bosons of mass  $a/2$  and chemical potential  $-a/2$  (specifically, the first term gives exactly the free energy of such bosons), and we can use standard methods to retrieve high- and low temperature expansions of it. At high temperatures ( $T \gg a$ ) we obtain

$$f(T, a) - f(0, a) = -\frac{\pi^2 T^4}{45} + \frac{a^2 T^2}{48} - \frac{a^3 T}{64} - \frac{5a^4}{256\pi^2} \left( \ln \frac{a}{8\pi T} + \gamma_E - \frac{1}{60} \right) + \mathcal{O}(a^6), \quad (2.99)$$

while at low temperatures ( $T \ll a$ ) we get

$$f(T, a) - f(0, a) = -\frac{3\zeta(7/2)}{2\sqrt{2}\pi^3} a^{1/2} T^{7/2} + \mathcal{O}(a^{-1/2}). \quad (2.100)$$

These expansions are useful in studying the asymptotic behaviour of the system, but in the following analysis we solve the system numerically using the exact results in Eqs. (2.98) and (2.90).

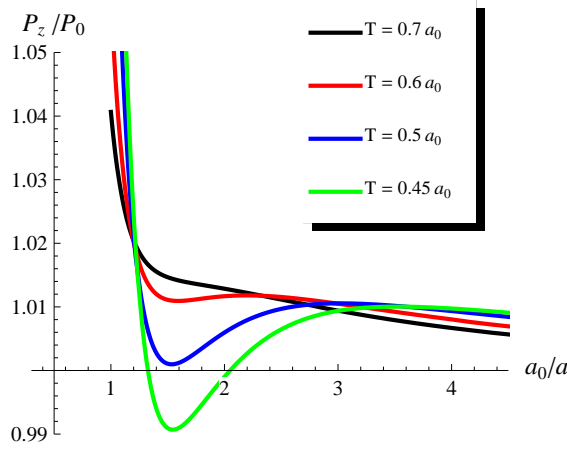


Figure 2.6: Longitudinal pressure as a function of  $1/a$  for various temperatures, normalized to Stefan-Boltzmann pressure.

### Phase diagram

We begin by showing the pressure as a function of  $1/a$  in Fig. 2.6 for various temperatures. There are important differences to the strong coupling situation. First, we emphasize that above a critical temperature there are no unstable regions present, because the pressure is a monotonically decreasing function of  $1/a$ . The second notable difference is that at small charge densities there exist stable regions for zero coupling, even if there are unstable regions for larger values of  $a$ . Therefore the situation at zero coupling becomes richer and additionally to the coexistence of isotropic and anisotropic regions (see eq. (2.62)) we have to discuss the coexistence of two different anisotropic regions as well.

If we have two homogeneous regions with charge densities  $a_1$  and  $a_2$  and  $0 < a_1 < a_2$  then the conditions for chemical and mechanical equilibrium are

$$\Phi(T, a_1) = \Phi(T, a_2) \equiv \Phi, \quad (2.101)$$

$$\frac{f(T, a_2) - f(T, a_1)}{a_2 - a_1} = \Phi, \quad (2.102)$$

respectively. The most important difference to  $a_1 = 0$  is that for  $a_1 > 0$  chemical equilibrium is also reached. At zero coupling both situations, namely zero and nonzero  $a_1$  are possible and the free energy as a function of the charge density is shown in Fig. 2.7. As opposed to strong coupling  $\partial^2 f / \partial^2 a > 0|_{a=0}$ . This can be seen already from the high temperature expansions of the free energy at strong and zero coupling eqs. (2.53) and (2.99)<sup>8</sup>.

<sup>8</sup>Note that  $f = -P_{\perp}$  and that then the  $a^2 T^2$  term in the high temperature expansion is positive for zero coupling but negative for infinite coupling.

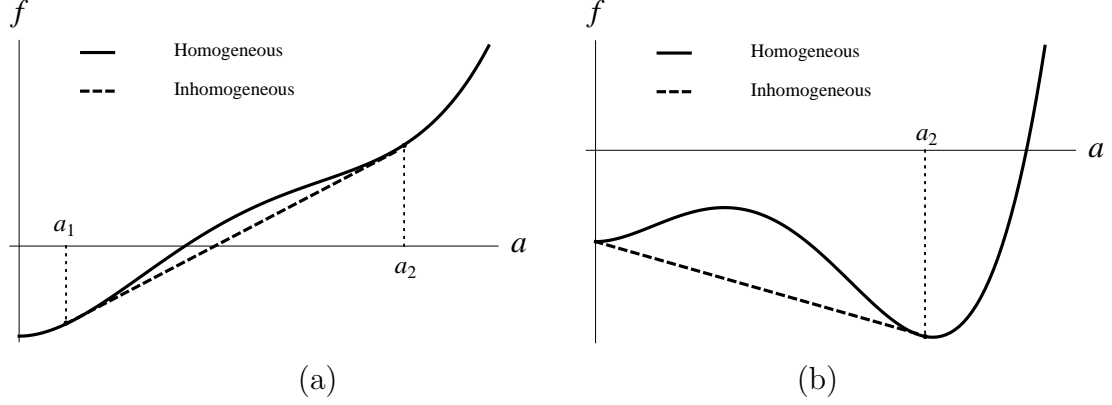


Figure 2.7: Two cases where the conditions for coexistence of homogeneous regions are realized. (a) The dashed line, giving the free energy of the inhomogeneous phase, is the tangent to  $f(T, a)$  at points  $a = a_1$  and  $a = a_2$ . (b) The dashed line is the tangent to  $f(T, a)$  at  $a = a_2$  and coincides with  $f(T, a)$  at  $a = 0$ .

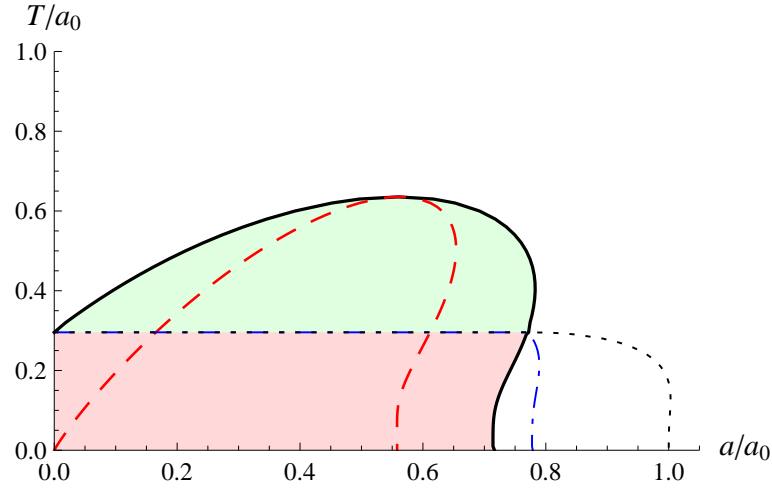


Figure 2.8: The phase diagram. The solid line separates the homogeneous and inhomogeneous (shaded region) phases. In the green shaded part of the phase diagram, the inhomogeneous phase consists of separate anisotropic regions with different values of  $a$ , whereas in the red shaded part, the plasma contains anisotropic and isotropic regions. The red dashed line indicates the region where the (would-be) homogeneous phase is unstable. The blue dash-dotted line indicates vanishing chemical potential. Inside the line, the pressure anisotropy is oblate, outside it is prolate. The dotted line indicates the region where  $f(a, T) < f(0, T)$ .

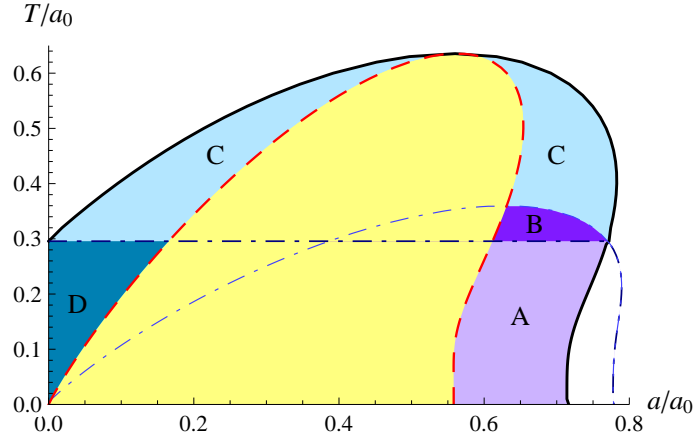


Figure 2.9: The phase diagram showing different metastable phases labeled A–D with homogeneous Chern-Simons charge distribution (the thermodynamically unstable region is shown in yellow). The light-blue dash-dotted curve corresponds to  $\Phi = 0$  in the homogeneous case, with  $\Phi > 0$  (prolate pressure anisotropy) and  $\Phi < 0$  (oblate) above and below this line, respectively. Above the straight dark-blue dash-dotted line the inhomogeneous ground state is composed of differently prolate plasma, below this line the ground state is a mix of isotropic and oblate plasma.

The actual phase diagram at zero coupling is presented in Fig. 2.8. The unstable and metastable regions are bounded by the black line. In the red shaded area the inhomogeneous phase consists of isotropic and anisotropic (finite charge density) regions, which have an oblate pressure anisotropy. In the green shaded region the system is, in addition to being inhomogeneous, also anisotropic everywhere. At large enough temperature the plasma is always stable.

The type of pressure anisotropy (prolate vs. oblate) is determined by the chemical potential  $\Phi = \partial f / \partial a$ . In Fig. 2.8 the boundary in separating prolate plasma from oblate plasma is given by the blue dot-dashed line. Outside that line, the plasma is prolate. This is also true for the inhomogeneous region that is shaded green. There every stack of plasma has prolate pressure anisotropy. The high temperature plasma is prolate irrespective of the value of the charge density, which is another obvious difference to strong coupling. Actually there is only a small region at low temperatures where the plasma is homogeneous and oblate (the unshaded region between the full line and the blue dash-dotted line).

In the region of the phase diagram where the inhomogeneous phase is energetically preferred, one can distinguish a number of qualitatively different metastable situations for homogeneous charge distribution as shown in Fig. 2.9. The thermodynamically unstable region for homogeneous charge distributions is colored yellow, while the metastable region is divided into four different sections labeled A–D. For a homogeneous charge distribution the dividing line between oblate and prolate pressure

anisotropy is given by light-blue dash-dotted curve, whereas for the inhomogeneous phase the dividing line is the straight dark-blue dash-dotted line. This difference is responsible for the appearance of four different “decay modes” of homogeneous metastable phases with density  $a$ :

- (A) the metastable homogeneous phase is oblate and decays into a mix of regions that are isotropic ( $a_1 = 0$ ) and oblate ( $a_2 > a$ )
- (B) the metastable homogeneous phase is oblate and decays into a mix of prolate regions with different nonvanishing densities  $a_1 < a$  and  $a_2 > a$
- (C) the metastable homogeneous phase is prolate and decays into a mix of prolate regions with different nonvanishing densities  $a_1 < a$  and  $a_2 > a$
- (D) the metastable homogeneous phase is prolate and decays into a mix of regions that are isotropic ( $a_1 = 0$ ) and oblate ( $a_2 > a$ )

Metastable homogeneous phases of type A and D decay into inhomogeneous systems that are not in chemical equilibrium, even though the initially homogeneous phase has been in chemical equilibrium trivially. We emphasize that at infinite coupling we only encounter section A. Therefore it turns out that, surprisingly, the zero coupling phase diagram is even richer than the one at infinite coupling.

# Chapter 3

## Photons and Dileptons

Photons and leptons produced in an early stage after the heavy ion collision interact only very weakly with the medium and can leave the plasma without any rescattering. Therefore the production of photons and dileptons is an interesting observable to study the far from equilibrium properties. In thermal equilibrium the production from an isotropic plasma has been studied both in (resummed) perturbation theory [67, 68, 69, 70] and in strongly coupled SYM plasma by means of holographic duality [71, 72, 73, 74]. At strong coupling also out of equilibrium production of photons and dileptons has been investigated, however in an isotropic background [75, 76]. And recently the dependence of the thermalization pattern on the gauge coupling in such a holographic model has been considered, too [77]. In a weakly coupled QGP the angular dependence of photon and dilepton production in the presence of momentum anisotropies has been studied in [78, 79, 80, 81, 82, 83, 84, 85]. In the following we shall discuss results obtained for stationary anisotropic plasma at infinite coupling making use of the models presented in sections 2.1 and 2.2.

### 3.1 Introducing Photons and Dileptons

We start by quickly reviewing the possibilities to couple electromagnetism to the  $\mathcal{N} = 4$  SYM theory, which consists of  $SU(N_c)$  gauge bosons, four Weyl fermions  $\psi_p$  and six real scalars  $\phi_{pq} = -\phi_{qp}$ , all transforming in the adjoint representation of  $SU(N_c)$ . There is also an anomaly free global  $SU(4)$   $R$ -symmetry present, under which the fermions transform in the **4** and the scalars in the **6** representation. We can take a  $U(1)$  subgroup of the  $SU(4)$   $R$ -symmetry associated with a  $U(1)$  gauge field coupled to the conserved current. By doing so we are able to model the electromagnetic interactions. In principle it is possible to take any linear combination of Cartan subalgebra generators to embed the  $U(1)$  in the  $SU(4)$   $R$ -symmetry group (for details see [71]). We will choose  $t^3 = (1/2, -1/2, 0, 0)$  to be the generator of the  $U(1)$  such

that two of the Weyl fermions have charge  $\pm 1/2$  and two complex scalars have charge  $1/2$ . The conserved current is

$$J_\mu^{EM} = \frac{1}{e} \frac{\delta S_{int}}{\delta A^\mu} = \frac{1}{2} \left( \psi_1^{a\dagger} \bar{\sigma}_\mu \psi_1^a - \psi_2^{a\dagger} \bar{\sigma}_\mu \psi_2^a + \sum_{p=3,4} \phi_{1p}^{a\dagger} (-i \vec{D}_\mu + i \overleftarrow{D}_\mu) \phi_{1p}^a \right), \quad (3.1)$$

where  $a$  is the  $SU(N_c)$  group index and the covariant derivative  $D_\mu$  involves the  $SU(N_c)$  gauge fields as well as the  $U(1)$  electromagnetic vector potential  $A_\mu$ . Because we are only interested in the leading order terms in the electromagnetic coupling  $e$ , it is sufficient to treat the electromagnetic interaction as being linear in  $A_\mu$ . Then we can consistently ignore the electromagnetic vector potential in the covariant derivative acting on the scalar. In order to also add weakly coupled leptons  $l$  with charge  $e_l$  and mass  $m$ , the Lagrangian is extended to

$$\mathcal{L} = \mathcal{L}_{SYM} + \mathcal{L}_{int} - \frac{1}{4} F_{\mu\nu}^2 - \bar{l} (\not{D} + m) l \quad \text{with } \mathcal{L}_{int} = e J_\mu^{EM} A^\mu, \quad (3.2)$$

where  $J_\mu^{EM}$  is the  $t^3$  component of the  $R$ -current.

In the gauge/gravity setup, only the SYM part will be realized dynamically, but we can calculate current-current correlators to leading order in the electromagnetic coupling and to all orders in the SYM coupling.

## 3.2 Production Rates

The rate of photons produced per unit time and per unit volume is<sup>1</sup>

$$d\Gamma_\gamma = \frac{d^3k}{(2\pi)^3} \frac{ie^2}{2|\mathbf{k}|} \eta^{\mu\nu} G_{\mu\nu}^<(K) |_{k^0=|\mathbf{k}|}, \quad (3.3)$$

where

$$G_{\mu\nu}^<(K) = \int d^4X e^{-iK \cdot X} \langle J_\mu^{EM}(0) J_\nu^{EM}(X) \rangle \quad (3.4)$$

is the Wightman function of electromagnetic currents. Any correlator of the conserved current can be expressed in terms of the spectral function, which is defined as

$$\chi_{\mu\nu}(K) = \int d^4X e^{-iK \cdot X} \langle [J_\mu^{EM}(0), J_\nu^{EM}(X)] \rangle \quad (3.5)$$

and the distribution function. Later we will determine this spectral function by making use of

$$\chi_{\mu\nu}(K) = -2\text{Im} G_{\mu\nu}^{ret}(K). \quad (3.6)$$

---

<sup>1</sup>Here we use capital letters to denote 4 vectors and lower case letters for the absolute value of 3 vectors. The Minkowski metric is defined as  $\eta_{\mu\nu} = \text{diag}(-1, 1, 1, 1)$ .



The Wightman function is given by

$$G_{\mu\nu}^<(K) = -i\chi_{\mu\nu}(K)f(K), \quad (3.7)$$

where  $f$  reduces to the Bose-Einstein distribution in thermal equilibrium.

The dilepton production takes place via an intermediate virtual photon and the rate is given by

$$d\Gamma_{l\bar{l}} = \frac{d^4K}{(2\pi)^4} \frac{ie^2e_l^2(-K^2 - 4m^2)^{1/2}(-K^2 + 2m^2)}{6\pi|K^2|^{5/2}} \theta(k^0)\theta(-K^2 - 4m^2)\eta^{\mu\nu}G_{\mu\nu}^<(K), \quad (3.8)$$

where  $e_l$  is the charge of the lepton. In this case the Wightman function has to be evaluated for timelike momenta.

### 3.3 Tensor Structure of Anisotropic Correlators

For an anisotropic medium, the tensor structure of the current-current correlator is more complicated than in the isotropic finite temperature case [48]. Because the electromagnetic current is conserved it must satisfy Ward identities, which in the vacuum implies that any  $G_{\mu\nu}(K) \sim P_{\mu\nu}\mathcal{C}(K)$  with  $P_{\mu\nu} = \eta_{\mu\nu} - K_\mu K_\nu/K^2$ .

We begin with the case when the wave vector is pointing in the direction of the anisotropy denoted by  $\mathbf{n} = n\mathbf{e}_z$ . Then it is sufficient to introduce longitudinal and transverse projectors

$$P_{00}^T = P_{i0}^T = 0, \quad P_{ij}^T = \delta_{ij} - \frac{k_i k_j}{k^2}, \quad P_{\mu\nu}^L = P_{\mu\nu} - P_{\mu\nu}^T, \quad (3.9)$$

with  $i, j = 1, 2, 3$ . For the correlators we then find

$$G_{\mu\nu}(K) = P_{\mu\nu}^T \tilde{\Pi}^T(K) + P_{\mu\nu}^L \tilde{\Pi}^L(K). \quad (3.10)$$

This is exactly the same structure one has in isotropic systems.

If we choose the wave vector to point in a perpendicular direction with respect to the anisotropy  $\mathbf{k} = k\mathbf{e}_1$ , we need one further tensorial structure,

$$P_{00}^2 = P_{i0}^2 = 0, \quad P_{ij}^2 = \delta_{ij} - \frac{k_i k_j}{k^2} - \frac{n_i n_j}{n^2} \quad (3.11)$$

$$P_{00}^z = P_{i0}^z = 0, \quad P_{ij}^z = \frac{n_i n_j}{n^2} \quad (3.12)$$

$$P_{\mu\nu}^1 = P_{\mu\nu} - P_{\mu\nu}^2 - P_{\mu\nu}^z. \quad (3.13)$$

As a consequence the correlator is then specified by three scalar functions

$$G_{\mu\nu}(K) = P_{\mu\nu}^1 \tilde{\Pi}^1(K) + P_{\mu\nu}^2 \tilde{\Pi}^2(K) + P_{\mu\nu}^z \tilde{\Pi}^z(K). \quad (3.14)$$

With a generic orientation of the wave vector, more structure functions would be needed, however, we shall restrict our attention to the two extreme cases of wave vector parallel and orthogonal to the anisotropy direction.

### 3.4 Singular Gravity Duals

We first compute the spectral function for the JW model, where the  $z$ -direction is the preferred direction and the metric can be written as<sup>2</sup>

$$ds^2 = g_{tt}(v)dt^2 + g_{xx}(v)(dx^2 + dy^2) + g_{zz}(v)dz^2 + g_{vv}(v)dv^2. \quad (3.15)$$

#### 3.4.1 Equations of Motion and Asymptotic Solution

To obtain the retarded correlator we have to solve the equations of motion for a gauge field, which are given by

$$\partial_A(\sqrt{-g}g^{AC}g^{BD}F_{CD}) = 0. \quad (3.16)$$

We start by considering the case when the wave vector points in the direction of the anisotropy ( $\mathbf{k} = k_L \mathbf{e}_z$ ). Then the equation of motion for  $E_T = \omega A_T$  is

$$E_T'' + \frac{\partial_v(\sqrt{-g}g^{vv}g^{xx})}{\sqrt{-g}g^{vv}g^{xx}}E_T' - \frac{g^{tt}\omega^2 + g^{zz}k_L^2}{g^{vv}}E_T = 0, \quad (3.17)$$

where primes denote derivatives with respect to the holographic coordinate  $v$ . The dependence of  $v$  is suppressed everywhere. The longitudinal electric field  $E_L = k_L A_t + \omega A_z$  satisfies

$$E_L'' + \frac{(g^{tt})^2 \partial_v(\sqrt{-g}g^{vv}g^{zz})\omega^2 + (g^{zz})^2 \partial_v(\sqrt{-g}g^{vv}g^{tt})k_L^2}{\sqrt{-g}g^{vv}g^{tt}g^{zz}(g^{tt}\omega^2 + g^{zz}k_L^2)}E_L' - \frac{g^{tt}\omega^2 + g^{zz}k_L^2}{g^{vv}}E_L = 0. \quad (3.18)$$

If the wave vector points in a direction in the  $xy$ -plane and therefore is perpendicular to the anisotropy, we obtain three different differential equations. For  $\mathbf{k} = k_1 \mathbf{e}_x$  we then find

$$E_2'' + \frac{\partial_v(\sqrt{-g}g^{vv}g^{xx})}{\sqrt{-g}g^{vv}g^{xx}}E_2' - \frac{g^{tt}\omega^2 + g^{xx}k_1^2}{g^{vv}}E_2 = 0, \quad (3.19)$$

$$E_z'' + \frac{\partial_v(\sqrt{-g}g^{vv}g^{zz})}{\sqrt{-g}g^{vv}g^{zz}}E_z' - \frac{g^{tt}\omega^2 + g^{xx}k_1^2}{g^{vv}}E_z = 0 \quad (3.20)$$

for the two modes transverse to the wave vector and

$$E_1'' + \frac{(g^{tt})^2 \partial_v(\sqrt{-g}g^{vv}g^{xx})\omega^2 + (g^{xx})^2 \partial_v(\sqrt{-g}g^{vv}g^{tt})k_1^2}{\sqrt{-g}g^{vv}g^{tt}g^{xx}(g^{tt}\omega^2 + g^{xx}k_1^2)}E_1' - \frac{g^{tt}\omega^2 + g^{xx}k_1^2}{g^{vv}}E_1 = 0 \quad (3.21)$$

---

<sup>2</sup>We note that the holographic coordinate in [48] corresponds to  $v^2$  here.

for the electric field along the direction of the wave vector. These equations are quite lengthy if the explicit form of the metric coefficients is inserted, therefore we will not do so here.

For all of these equations, we can use a Frobenius ansatz near the boundary ( $v = 0$ ) and find the characteristic exponents to be 0 and 2. Close to the naked singularity (which appears exactly where the horizon is in the isotropic case) the differential equations have the following form,

$$\frac{d^2}{dv^2}\phi + \frac{C_1}{(1-v)}\frac{d}{dv}\phi + \frac{\omega^2 C_2}{(1-v)^\alpha}\phi = 0 \quad (3.22)$$

with  $\alpha = (2 + \sqrt{36 - 2B^2})/4 \leq 2$ . For isotropic systems  $\alpha = 2$  and a Frobenius ansatz is still possible at  $v = 1$ . We then find the characteristic exponents  $\pm i\omega/\sqrt{8}$  near the horizon and we can easily define ingoing boundary conditions. For nonvanishing anisotropy  $\alpha < 2$  we can perform a coordinate transformation  $x = (1-v)^{(2-\alpha)}$  in order to find appropriate boundary conditions at the naked singularity. The equation of motion is given by

$$\frac{d^2}{dx^2}\phi + \frac{\beta}{x}\frac{d}{dx}\phi + \frac{\gamma^2}{x}\phi = 0 \quad (3.23)$$

where

$$\beta = 1 - \frac{C_1 + 1}{2 - \alpha} \quad \gamma^2 = \frac{C_2 \omega^2}{(2 - \alpha)^2}. \quad (3.24)$$

The solution to this differential equation is

$$\phi(v) \sim (1-v)^{(2-\alpha)(1-\beta)/2} H_{1-\beta}^{(1,2)}(2\gamma(1-v)^{(2-\alpha)/2}), \quad (3.25)$$

where the Hankel function of the second kind  $H_\nu^{(2)}$  represents ingoing boundary conditions, which we will use for our numerical studies later on.

### 3.4.2 Spectral functions at strong coupling

In order to find the on-shell boundary action, we start from the five-dimensional Maxwell action, which is given by

$$S_{Maxwell} = -\frac{1}{4g_B^2} \int d^5x \sqrt{-g} g^{AC} g^{BD} F_{AB} F_{CD} \quad (3.26)$$

with  $g_B = 16\pi^2 L/N_c^2$  and  $L$  the AdS radius. Choosing the gauge  $A_v = 0$  we obtain the on-shell boundary term

$$\begin{aligned} S_{bdry} = & -\frac{1}{2g_B^2} \int_{v \rightarrow 0} d^4x \sqrt{-g} g^{vv} \left( g^{tt} A'_t(K, v) A_t(-K, v) \right. \\ & \left. + g^{zz} A'_z(K, v) A_z(-K, v) + g^{xx} \mathbf{A}'_T(K, v) \mathbf{A}_T(-K, v) \right). \end{aligned} \quad (3.27)$$

Considering a wave vector pointing into the direction of the anisotropy first, we obtain the relation

$$\omega g^{tt} A'_t(K, v) - k_L g^{zz} A'_z(K, u) = 0, \quad (3.28)$$

which follows directly from the equations of motion. Inserting this into (3.27) and rewriting the result in terms of electric fields  $E_L = \omega A_z + k_L A_t$  and  $\mathbf{E}_T = \omega \mathbf{A}_T$ , the boundary term of the action becomes

$$\begin{aligned} S_{bdry} = & -\frac{1}{2g_B^2} \int_{v \rightarrow 0} d^4x \sqrt{-g} g^{vv} \left( \frac{g^{tt}}{\omega^2 g^{tt}/g^{zz} + k_L^2} E'_L(K, v) E_L(-K, v) \right. \\ & \left. + \frac{g^{xx}}{\omega^2} \mathbf{E}'_T(K, v) \mathbf{E}_T(-K, v) \right). \end{aligned} \quad (3.29)$$

The transverse correlator is defined as

$$G_{TT}(K) = \frac{\delta^2 S_{bdry}}{\delta A_T(K) \delta A_T(-K)} = \frac{\omega^2 \delta^2 S_{bdry}}{\delta E_T(K) \delta E_T(-K)}. \quad (3.30)$$

Applying the Lorentzian AdS/CFT prescription [86] and inserting the explicit form of the metric coefficients we find<sup>3</sup>

$$G_{TT}(K) = \tilde{\Pi}_T(K) = -\frac{2}{g_B^2} \lim_{v \rightarrow 0} \frac{E'_T(K, v)}{E_T(K, v)}. \quad (3.31)$$

After a similar computation for the longitudinal correlator we find

$$\tilde{\Pi}_L(K) = -\frac{2}{g_B^2} \lim_{v \rightarrow 0} \frac{E'_L(K, v)}{E_L(K, v)}. \quad (3.32)$$

When the wave vector is in the 1-direction we obtain three scalar functions which are given by

$$\tilde{\Pi}_n(K) = -\frac{2}{g_B^2} \lim_{v \rightarrow 0} \frac{E'_n(K, v)}{E_n(K, v)}, \quad (3.33)$$

with  $n = 1, 2, z$ .

### 3.4.3 Numerical Results

#### Wave vector parallel to anisotropy direction

First, we discuss the form of the spectral function for a wave vector parallel to the anisotropy direction. For lightlike momenta only the transverse contribution to the

---

<sup>3</sup>Defining the correlator in this way a real contact term proportional to  $K^2$  that, however, does not contribute to the physically relevant spectral function we are interested in, is to be discarded.

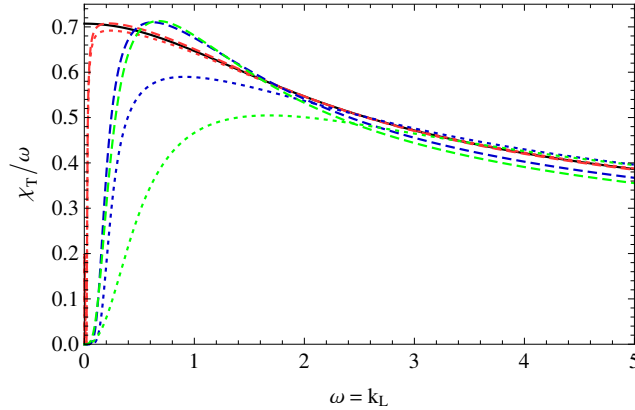


Figure 3.1: Transverse contribution to spectral density for lightlike momenta with values for the anisotropy parameter  $B = 0$  (black),  $B = 0.1$  (red, dashed),  $B = -0.1$  (red, dotted),  $B = 1$  (blue, dashed),  $B = -1$  (blue, dotted),  $B = \sqrt{2}$  (green, dashed) and  $B = -\sqrt{6}$  (green, dotted). The dimensionful parameter  $A$ , which equals  $\pi^2 T^2/2$  in the isotropic case  $B = 0$ , has been set to unity.

spectral density is nonvanishing and the results for different anisotropy parameters are shown in Fig. 3.1. The isotropic spectral density is shown in black and coincides with [71] after the correct normalization is chosen. For nonvanishing anisotropy we notice a qualitative difference for small frequencies, namely all spectral functions tend to zero faster than  $\omega$ , which is in stark contrast to the isotropic situation. However, for small values of  $B$  the curve quickly rises and then settles close to the isotropic one. For increasing anisotropy the spectral densities deviate more strongly from the isotropic result, in particular at small frequencies.

We have already mentioned that the appearance of a naked singularity in the JW model can be viewed as a break-down of the stationarity condition of the anisotropic model. Therefore the small frequency limit is unphysical and cannot be studied within this framework. The same actually happens for models that study non-equilibrium but isotropic situations by considering collapsing shells in a stationary limit [75, 76]. On the other hand, at larger frequencies our analysis should be able to map the nonequilibrium situation in the form of a snapshot, so it is reassuring that there the effects of the anisotropy connect smoothly with the isotropic limit. Given that the appearance of the naked singularity changes the character of the differential equations, this is not completely obvious a priori.

Since the low frequency limit seems to be unphysical, the question arises down to what value of  $\omega$  we might trust this calculation. It makes sense to assume that the lower bound of the frequency will depend on the anisotropy of the system. For larger anisotropies our assumption of a time invariant background may break down earlier.

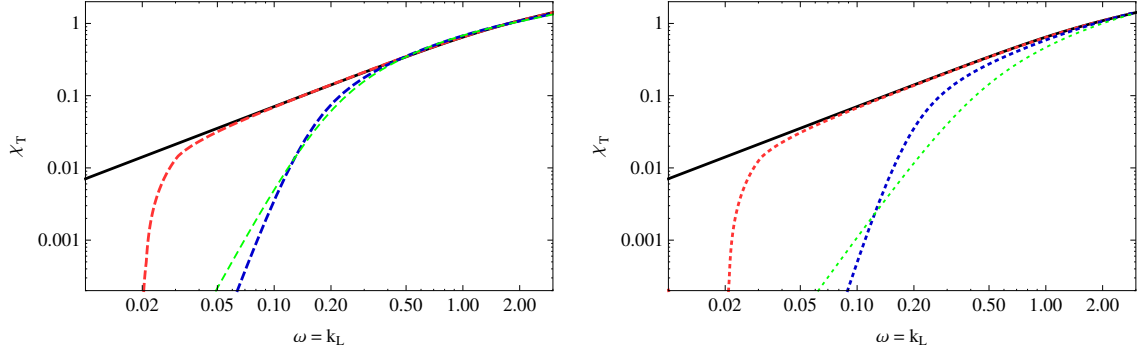


Figure 3.2: Double logarithmic plot to estimate the deviation from the linear behavior of the spectral function with respect to  $\omega$ . In the left panel we consider positive anisotropies and in the right panel negative ones. Color coding as in Fig. 3.1.

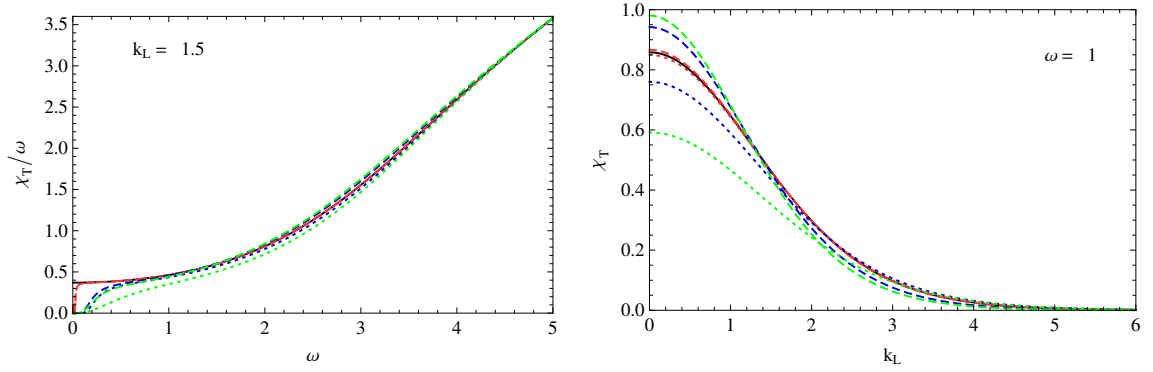


Figure 3.3: Transverse spectral function for  $k_L$  fixed (left) and  $\omega$  fixed (right). Color coding as in Fig. 3.1.

A possible hint to estimate the range of validity of the calculation presented here can come from considering the deviation from  $\chi \propto \omega$ . This is presented in Fig. 3.2 where we plot the spectral density logarithmically. We see that even for the most extreme anisotropy parameters this suggests that our calculation is valid down to  $\omega \sim 1$  (in units where  $A = 1$ ).

In Fig. 3.3 the form of the transverse part of the spectral function is shown for  $k_L$  fixed and  $\omega$  fixed, respectively. In the left panel the difference in the small frequency behavior between isotropic and anisotropic results is again obvious.

As already mentioned the longitudinal part of spectral density  $\chi_L = \chi_{zz} - \chi_{tt}$  vanishes for lightlike momenta. This is still the case if we turn on the anisotropy. In Fig. 3.4 we see that the spectral function is negative for spacelike momenta, vanishes

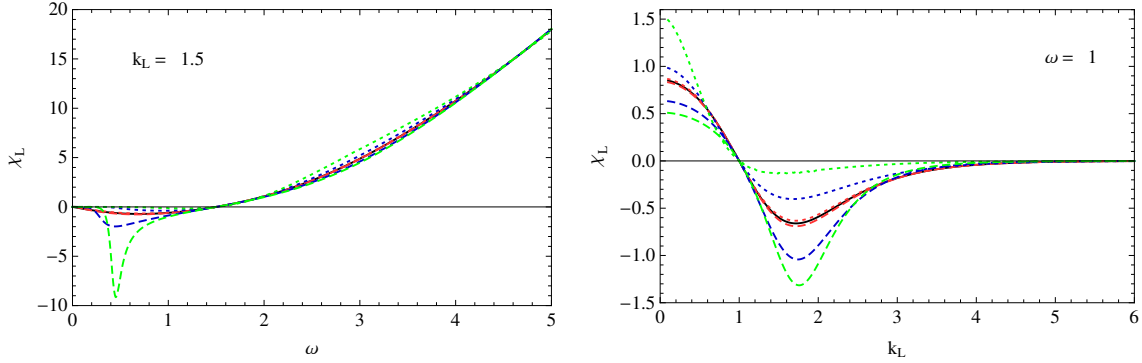


Figure 3.4: Longitudinal spectral function for  $k_L$  fixed (left) and  $\omega$  fixed (right). Color coding as in Fig. 3.1.

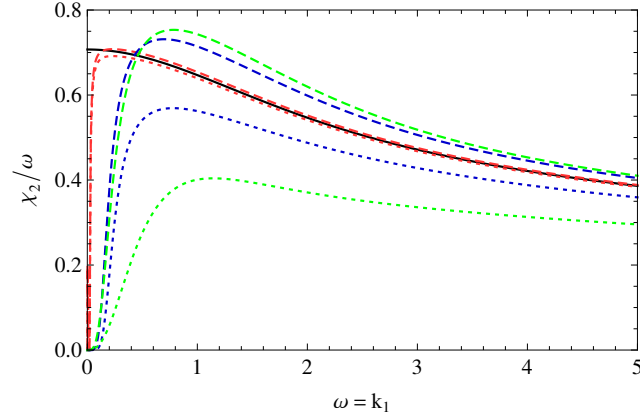


Figure 3.5: Part of spectral density perpendicular to  $k_1$  and to the anisotropy direction for lightlike momenta. Color coding as in Fig. 3.1.

for lightlike momenta and becomes positive for timelike momenta.

### Wave vector perpendicular to anisotropy direction

Next we consider a wave vector pointing in a direction in the  $xy$ -plane. Then there is a mode  $E_2$  which is both, perpendicular to the wave vector and the anisotropy direction. This mode can be compared to the transverse mode before and we see that the behavior for small frequencies and wave vectors is quite similar. The spectral function is larger for oblate anisotropy and smaller for prolate. However, while this is still true for larger frequencies and momenta in the present case (see Fig. 3.5), the opposite was true for  $\chi_T$ , where the behavior changed at some intermediate frequency or momentum.

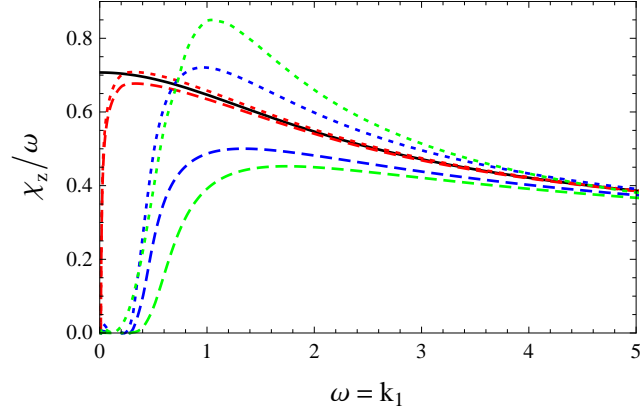


Figure 3.6: Spectral function along the anisotropy direction for lightlike momenta. Color coding as in Fig. 3.1.

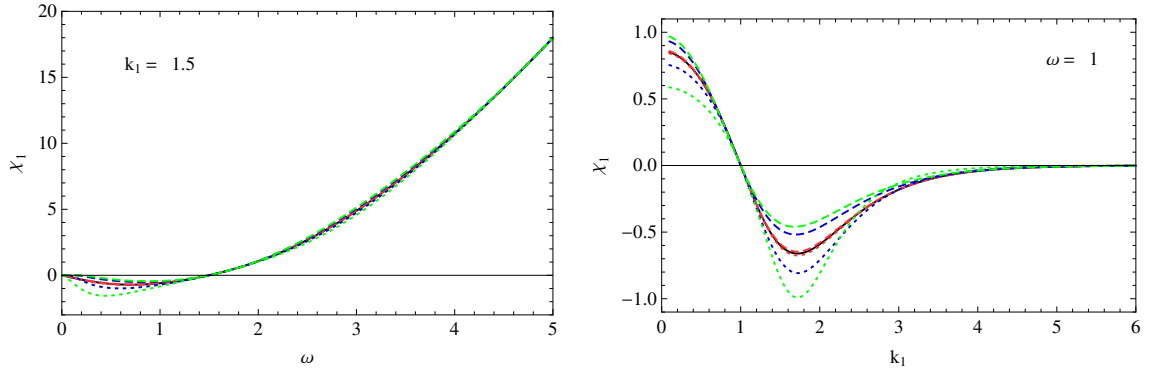


Figure 3.7: Spectral function longitudinal to the wave vector for  $k_1$  fixed (left) and  $\omega$  fixed (right). Color coding as in Fig. 3.1.

For  $\mathbf{k} = k_1 \mathbf{e}_1$  there is another mode which is transverse with respect to the wave vector. The results for this mode, which is pointing along the  $z$ -direction are shown for lightlike momenta in Fig. 3.6. Compared to the previous modes that were transverse with respect to the wave vector, the dependence on  $B$  changed. Here the spectral density is larger for prolate anisotropy and smaller in the oblate case.

Finally, we can consider the mode longitudinal to the wave vector. The behavior is shown in Fig. 3.7 and we note that the modifications for oblate and prolate plasma are now reversed as compared to the longitudinal mode in  $z$ -direction.



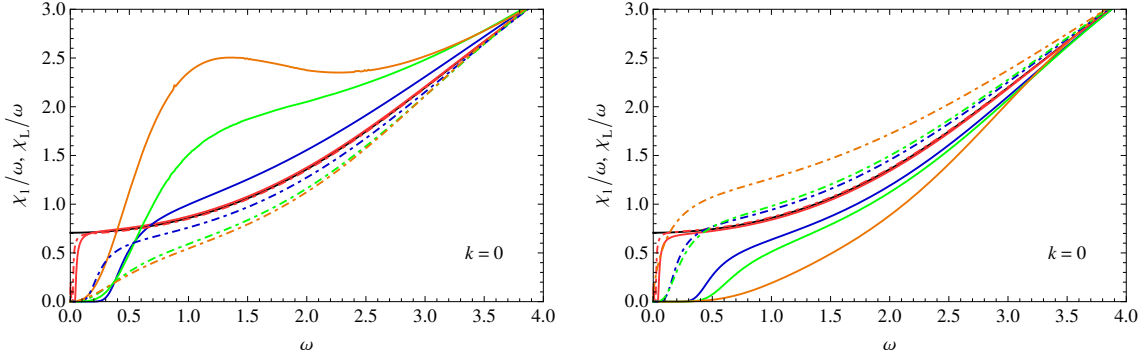


Figure 3.8: Anisotropic AC conductivities: prolate vs. oblate anisotropies for various values of  $B$ . Full lines correspond to longitudinal conductivity, dashed lines to transverse conductivity. Color coding of  $B$  as in Fig. 3.1, with the addition of orange lines for  $B = \mp 3$ , values for which negative pressures arise.

### Conductivities

The fact that for any nonzero anisotropy parameter  $B$  all spectral functions tend to zero stronger than linearly in the limit  $\omega \rightarrow 0$  means that both the diffusion constant and the DC conductivity vanish according to Kubo's formulae. This absence of hydrodynamic behavior is clearly related to the absence of a horizon, which for  $B \neq 0$  gets replaced by a naked singularity.

In Fig. 3.8 we display the results for the AC conductivities, juxtaposed for the cases of prolate ( $B < 0$ ) and oblate ( $B > 0$ ) anisotropies. In each case one can define longitudinal and transverse conductivities with respect to the direction of anisotropy. For prolate anisotropies transverse conductivities are found to be reduced compared to the isotropic case, whereas for oblate anisotropies this is true for longitudinal conductivities. However, in the limit of vanishing frequency, all conductivities go to zero. The frequency range in which this happens increases as the amount of anisotropy is increased, up to the point where one of the pressure components goes to zero. Curiously, when increasing the anisotropy parameter such that also negative pressures are produced, this trend is eventually reversed.

### Anisotropy of traced spectral function for lightlike and timelike momenta

The production of real photons is proportional to the trace of the spectral functions for lightlike momenta. When the wave vector is parallel to the anisotropy direction, we have

$$\chi^\mu{}_\mu(\mathbf{k} = k_L \mathbf{e}_L, K^2 = 0) = 2\chi_T(k_L), \quad (3.34)$$

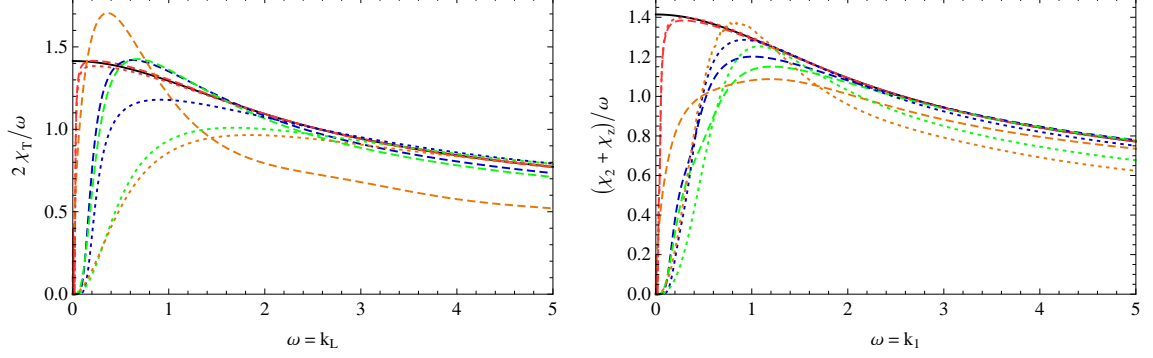


Figure 3.9:  $\chi^\mu{}_\mu/\omega$  for lightlike momenta with wave vector parallel to the anisotropy direction (left panel) and transverse to it (right panel). Color coding of  $B$  as in Fig. 3.8.

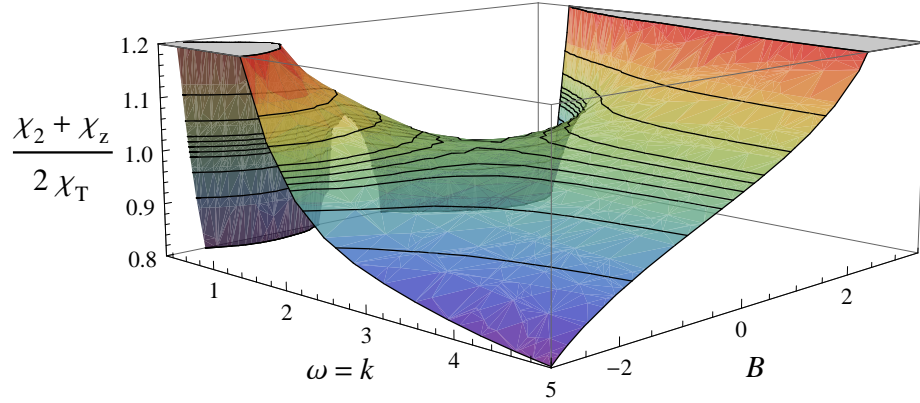


Figure 3.10: Ratio of  $\chi^\mu{}_\mu$  for lightlike momenta with transverse wave vector over this quantity with parallel wave vector (w.r.t. the direction of anisotropy) as a function of both frequency and anisotropy parameter  $B$ .

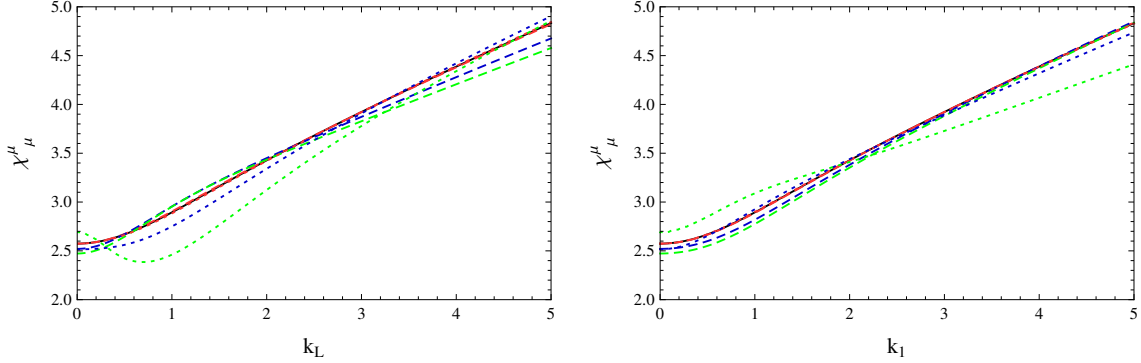


Figure 3.11:  $\chi^\mu{}_\mu$  for timelike momenta with invariant mass  $K^2 = -1$  as a function of  $k_L$  and  $k_1$ , respectively. Color coding as in Fig. 3.1.

whereas for transverse wave vector,

$$\chi^\mu{}_\mu(\mathbf{k} = k_1 \mathbf{e}_1, K^2 = 0) = \chi_2(k_1) + \chi_z(k_1). \quad (3.35)$$

In Fig. 3.9 the results for the wave vector pointing parallel and perpendicular to the anisotropy direction are juxtaposed, and in Fig. 3.10 the ratio between the latter and the former is shown as a function of frequency and anisotropy parameter  $B$ .

For frequencies  $\omega < 1$  (in units where  $A = 1$ ) this ratio shows a rather dramatic dependence on the anisotropy parameter. However, as we have discussed above, we consider this regime to be unphysical. For larger frequencies we indeed find a smoother dependence on the anisotropy parameter. For positive  $B$  (oblate anisotropy) the spectral function with wave vector pointing in the direction of anisotropy is reduced, for negative  $B$  the situation is reversed. As we shall discuss below, this is in line with the behavior of particle distributions for corresponding momentum anisotropies, but the latter typically have exponential suppression at high momentum.

In Fig. 3.11 we display the behavior of  $\chi^\mu{}_\mu$  for timelike momenta, which is relevant for dilepton production, as a function of  $k_L$  and  $k_1$  for the two cases of longitudinal and transverse momentum at a fixed value of  $K^2 = -1$  and observe a fairly mild dependence on the anisotropy parameter  $B$ .

### Photon and dilepton emission

In order to obtain the photon and dilepton production rates, we must insert the results for the spectral function into (3.3) and (3.8), respectively. For the final result we would also need to know the distribution function  $f$ , which in the out-of-equilibrium situation is no longer fixed to the Bose-Einstein function. Absent the fluctuation-dissipation theorem, we should therefore calculate the Wightman function within the

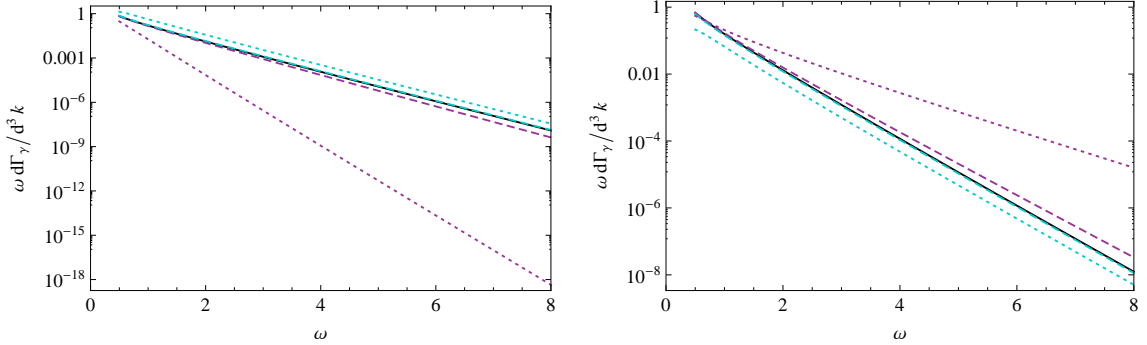


Figure 3.12: Photon production rate in forward (purple) and transverse (cyan) direction for  $B = \pm 0.1$  (dashed) and  $B = \pm 1$  (dotted), where positive signs (oblate cases) correspond to the plot on the left and negative signs (prolate cases) are shown in the right panel. The distribution function  $f$  is normalized by a multiplicative constant  $N(\xi)$  such that the energy density is kept fixed and  $p_{hard} = T = \sqrt{2}/\pi$  in units of  $A = 1$ . As a reference the isotropic rate is given in black.

gauge/gravity duality framework directly. Attempts to incorporate the full formalism of nonequilibrium physics in the AdS/CFT correspondence were undertaken in [87, 88, 89], but we have not been able to apply these concepts to our case.

We shall instead make an estimate of photon and dilepton emission rates by assuming that  $f$  is given by the form (C.1) with a parameter  $\xi$  that at weak coupling gives the same energy momentum tensor as in the boundary field theory of our gravity dual (see eq. (C.6)). Unfortunately the major effect on the directional dependence is then coming from the distribution function, which depends exponentially on the emission angle. In the JW model the energy density depends only weakly on the anisotropy and therefore we want the distribution function to be normalized in such a way that the energy density at weak coupling is kept fixed while we vary the anisotropy parameter  $\xi$ . As we discuss in appendix C.1 this can either be achieved by adjusting an overall constant  $N(\xi)$  or by changing the hard momentum scale according to eq. (C.5).

In Fig. 3.12 we display the resulting photon production rates in longitudinal and transverse directions for small and medium anisotropies when we normalize the distribution function by an overall multiplicative constant<sup>4</sup>  $N(\xi)$ . The left panel shows the situation for oblate anisotropies ( $B = 0.1$  and  $1$ ), the right panel for prolate anisotropies ( $B = -0.1$  and  $-1$ ). To show the dependence on the normalization procedure we also present the results where we have rescaled  $p_{hard}$  such that the energy density is fixed in Fig. 3.13.

<sup>4</sup>Note that in [48] we have set  $p_{hard} = A$ , whereas in Fig. 3.12 we have chosen  $p_{hard} = T = \sqrt{2A}/\pi$ .

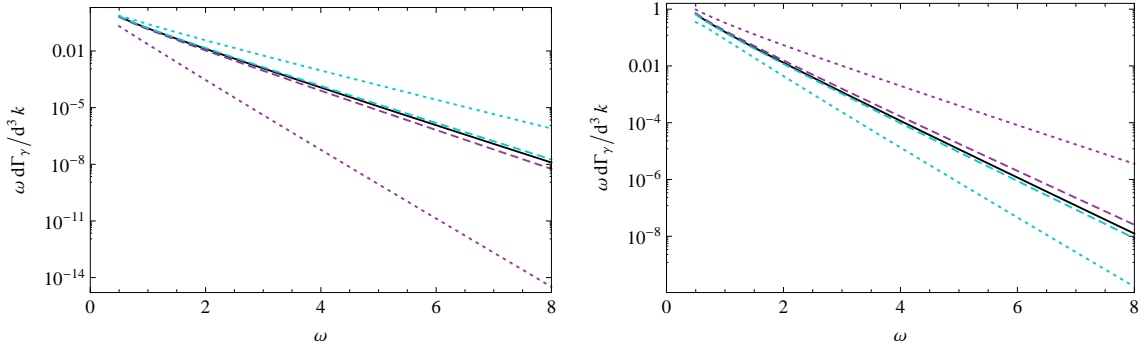


Figure 3.13: Photon production rate in forward (purple) and transverse (cyan) direction for  $B = \pm 0.1$  (dashed) and  $B = \pm 1$  (dotted), where positive signs (oblate cases) correspond to the plot on the left and negative signs (prolate cases) are shown in the right panel. Here  $f$  is normalized by rescaling  $p_{hard}$  and  $N(\xi) = 1$ . As a reference the isotropic rate is given in black.

In either case the directional dependence of the photon emission agrees qualitatively with the corresponding result for oblate anisotropies in the weak coupling (hard anisotropic loop resummed) calculation of Ref. [78].<sup>5</sup> Similar results are obtained for production rates of dileptons. The angular dependence in both cases is strongly dominated by the function  $f$  when it is chosen in accordance to the situation at weak coupling.

## 3.5 Anisotropically $\theta$ -deformed gauge theory

### 3.5.1 Using the membrane paradigm

The same procedure we just outlined for the JW model should in principle also work for the MT model, but it turns out that it is numerically demanding. However, in contrast to the JW model the axion-dilaton-gravity dual possesses a black hole with a regular horizon and therefore allows for a different approach to calculate retarded correlators, namely via the “membrane paradigm”, which states that every black hole in general relativity has in a precise sense a fictitious fluid on its horizon [90]. This fluid can then be identified with the low-energy description of a strongly coupled field

<sup>5</sup>Our estimated result for real photon production is in fact more strongly suppressed in the forward direction than the result of Ref. [78]. It shares this behavior with the soft part of the full result of Ref. [78], which in the forward direction is dominated by hard contributions. The final result of Ref. [78] actually depends on the choice of a separation parameter of hard and soft scales which was fixed by a minimization procedure in the isotropic case. Fixing it instead anew for each value of  $\xi$  would further reduce the hard-loop result in the forward direction.

theory dual to the gravity theory [91, 92, 93, 94]. In order to get the full retarded correlator and not only its hydrodynamic limit ( $\omega, k \rightarrow 0$ ) it is necessary to “take the membrane to the horizon” and calculate the flow of the quantity of interest with respect to the holographic coordinate<sup>6</sup>.

We start by considering a standard Maxwell action (3.26) for a U(1) gauge field in the bulk with coupling constant  $g_B$ . The conjugate momentum with respect to evolution in the holographic coordinate  $u$  is given by

$$j^\mu \equiv \Pi^\mu = \frac{\partial \mathcal{L}}{\partial(\partial_u A_\mu)} = -\frac{\sqrt{-g}}{g_B^2} g^{uu} g^{\mu\nu} F_{u\nu}, \quad (3.36)$$

where by  $\Pi$  we generically denote conjugate momenta with respect to the holographic coordinate. Considering Maxwell’s equation  $\partial_A(\sqrt{-g} g^{AC} g^{BD} F_{CD}) = 0$  and setting  $B = u$  we find

$$\partial_\mu j^\mu = 0, \quad (3.37)$$

which states that currents are conserved on any constant  $u$ -slice. The crucial observation is that while  $F_{ui}$  (which is proportional to  $j^i$ ) and the electric field  $E_i = F_{it}$  are in principle independent, they are related to each other at the horizon. The reason is that the horizon is a regular place for free infalling observers and therefore the gauge field  $A^M$  near the horizon must be nonsingular. The nonsingular combination of  $u$  and  $t$  is given by the Eddington Finkelstein coordinate  $\tilde{v}$  and is defined by<sup>7</sup>

$$d\tilde{v} = dt - \sqrt{-\frac{g_{uu}}{g_{tt}}} du \quad (3.38)$$

which implies

$$F_{ui} = -\sqrt{-\frac{g_{uu}}{g_{tt}}} F_{ti} \quad (3.39)$$

after choosing the gauge  $A_u = 0$  and setting the spatial momentum to zero. The two different membrane conductivities at the horizon are then given by [49]

$$\sigma^{yy}(\omega, u_h) = \sigma^{xx}(\omega, u_h) = \frac{j^x(\omega, u_h)}{F_{xt}(\omega, u_h)} = g_B^{-2} \sqrt{\gamma} g^{xx}|_{uh}, \quad (3.40)$$

$$\sigma^{zz}(\omega, u_h) = \frac{j^z(\omega, u_h)}{F_{zt}(\omega, u_h)} = g_B^{-2} \sqrt{\gamma} g^{zz}|_{uh}, \quad (3.41)$$

<sup>6</sup>There may be observables where even the hydrodynamic limit has a nontrivial flow from the horizon to the boundary. We will encounter such a situation in chapter 4.3.1.

<sup>7</sup>Note that in our notation  $g_{tt}$  is negative in Lorentzian prescription.

where  $\gamma = g/g_{tt}g_{uu}$  and turn out to be independent of the frequency. Next, we have to relate these to the AC conductivities at the boundary defined by

$$\sigma^{ij}(K, 0) = -\frac{G_R^{ij}(K)}{i\omega} = \lim_{u \rightarrow 0} \frac{j^i(K, u)}{F_{jt}(K, u)}, \quad (3.42)$$

where we also want to allow for nonvanishing spatial momenta.

We start by considering a wave vector  $\mathbf{k} = k_L \mathbf{e}_z$  pointing in the direction of the anisotropy and fluctuations along  $(t, z)$ . Maxwell's equations then give

$$g_B^2 \partial_u j^t = i k_L \sqrt{-g} g^{zz} g^{tt} F_{zt}, \quad (3.43)$$

$$g_B^2 \partial_u j^z = i \omega \sqrt{-g} g^{tt} g^{zz} F_{zt}, \quad (3.44)$$

and because of current conservation we find  $j^t = \frac{k_L}{\omega} j^z$ . Using the Bianchi identity  $\partial_t F_{zu} + \partial_z F_{ut} + \partial_u F_{tz} = 0$  we finally obtain

$$\begin{aligned} \partial_u \sigma^{zz} &= \frac{\partial_u j^z}{F_{zt}} - \frac{j^z}{F_{zt}^2} \partial_u F_{zt} \\ &= i \omega \sqrt{-\frac{g_{uu}}{g_{tt}}} \left[ \frac{(\sigma^{zz})^2}{\Sigma_A^z} \left( 1 + \frac{k_L^2}{\omega^2} \frac{g_{tt}}{g_{zz}} \right) - \Sigma_A^z \right], \end{aligned} \quad (3.45)$$

with  $\Sigma_A^z = g_B^{-2} \sqrt{\gamma} g^{zz}$ . We emphasize that  $\sigma^{zz}$  above depends on  $u$  but for better readability we will not write this dependence explicitly. We have to specify a boundary condition for this differential equation which can be obtained by demanding regularity of  $\sigma^{zz}$  at the horizon. Therefore the right side of eq. (3.45) has to vanish, because  $\sqrt{-g_{uu}/g_{tt}} \propto (u - u_h)^{-1}$ . This requirement uniquely determines  $\sigma^{zz}|_{u_h}$  which coincides with eq. (3.41) and is valid even for nonvanishing momenta. For the transverse fluctuations, which we choose to be in  $x$ -direction without loss of generality, Maxwell's equations give

$$-g_B^2 \partial_u j^x + \sqrt{-g} g^{tt} g^{xx} \partial_t F_{tx} + \sqrt{-g} g^{zz} g^{xx} \partial_z F_{zx} = 0 \quad (3.46)$$

and the relevant Bianchi identities are

$$\partial_t F_{xu} + \partial_u F_{tx} = 0, \quad (3.47)$$

$$\partial_t F_{xz} + \partial_z F_{tx} = 0. \quad (3.48)$$

In the end the flow equation is given by

$$\partial_u \sigma^{xx} = i \omega \sqrt{-\frac{g_{uu}}{g_{tt}}} \left[ \frac{(\sigma^{xx})^2}{\Sigma_A^x} - \Sigma_A^x \left( 1 + \frac{k_L^2}{\omega^2} \frac{g_{tt}}{g_{zz}} \right) \right], \quad (3.49)$$

where  $\Sigma_A^x = g_B^{-2} \sqrt{\gamma} g^{xx}$  and regularity at the horizon again requires  $\sigma^{xx}|_{u_h}$  to be equal to eq. (3.40) also for finite spatial momenta. Before we turn to the situation

for a wave vector pointing in a direction perpendicular to the anisotropy we give the relation between the AC conductivities at the boundary and the scalar functions given in eq. (3.10),

$$\sigma^{xx}(K, 0) = \frac{1}{\omega} \text{Im } \tilde{\Pi}^T(K), \quad (3.50)$$

$$\sigma^{zz}(K, 0) = \frac{\omega}{\omega^2 - k_L^2} \text{Im } \tilde{\Pi}^L(K). \quad (3.51)$$

For a wave vector  $\mathbf{k} = k_1 \mathbf{e}_x$  analogous computations lead to the flow equations

$$\partial_u \sigma^{xx} = i\omega \sqrt{-\frac{g_{uu}}{g_{tt}}} \left[ \frac{(\sigma^{xx})^2}{\Sigma_A^x} \left( 1 + \frac{k_1^2}{\omega^2} \frac{g_{tt}}{g_{xx}} \right) - \Sigma_A^x \right], \quad (3.52)$$

$$\partial_u \sigma^{yy} = i\omega \sqrt{-\frac{g_{uu}}{g_{tt}}} \left[ \frac{(\sigma^{yy})^2}{\Sigma_A^x} - \Sigma_A^x \left( 1 + \frac{k_1^2}{\omega^2} \frac{g_{tt}}{g_{xx}} \right) \right], \quad (3.53)$$

$$\partial_u \sigma^{zz} = i\omega \sqrt{-\frac{g_{uu}}{g_{tt}}} \left[ \frac{(\sigma^{zz})^2}{\Sigma_A^z} - \Sigma_A^z \left( 1 + \frac{k_1^2}{\omega^2} \frac{g_{tt}}{g_{xx}} \right) \right], \quad (3.54)$$

and the values of the respective conductivities at the horizon are again the same as in eqs. (3.40) and (3.41). Relating this to the scalar function in eq. (3.14) gives

$$\sigma^{xx}(K, 0) = \frac{\omega}{\omega^2 - k_1^2} \text{Im } \tilde{\Pi}^1(K), \quad (3.55)$$

$$\sigma^{yy}(K, 0) = \frac{1}{\omega} \text{Im } \tilde{\Pi}^2(K), \quad (3.56)$$

$$\sigma^{zz}(K, 0) = \frac{1}{\omega} \text{Im } \tilde{\Pi}^L(K). \quad (3.57)$$

### 3.5.2 Numerical results

#### DC conductivities

First of all we note that in the hydrodynamic limit ( $\omega, k \rightarrow 0$ ) all the flow equations become trivial and therefore the DC conductivities are completely determined by the horizon data. This furthermore implies that they do not depend on the scale  $\mu$  present in the MT model, but only on the ratio  $a/T$ . In the following we will denote the two different DC conductivities by  $\sigma_\perp = \sigma^{xx}(0, 0)$  and  $\sigma_z = \sigma^{zz}(0, 0)$ . Inserting the explicit form of the metric (2.18) into eqs. (3.40) and (3.41) together with the trivial flow in the hydrodynamic limit reveals that

$$\sigma_z = \frac{g_{xx}(u_h)}{g_{zz}(u_h)} \sigma_\perp = \frac{\sigma_\perp}{\mathcal{H}(u_h)} \leq \sigma_\perp. \quad (3.58)$$

The numerical results are presented in Fig. 3.14.



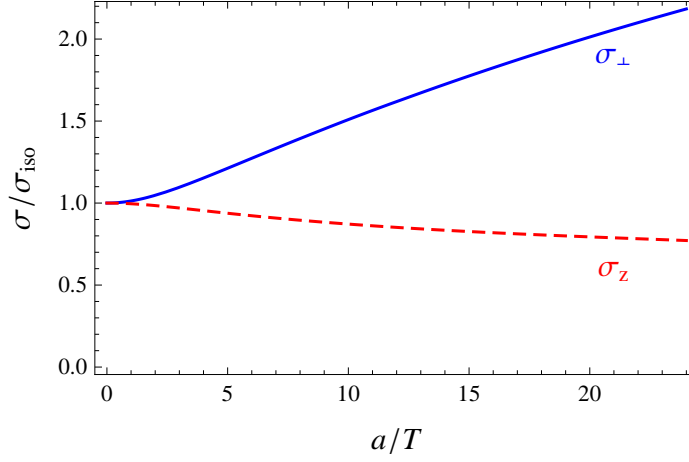


Figure 3.14: DC conductivities along and transverse to the direction of anisotropy as a function of the anisotropy parameter  $a/T$ .

### Diffusion constants

Next, we study charge diffusion processes. In general diffusion is governed by a dispersion law of the form

$$\omega = -iDk^2. \quad (3.59)$$

In our anisotropic situation we expect different diffusion constants  $D$  depending on the direction of  $\mathbf{k}$ . We start by assuming that  $\mathbf{k} = k_L \mathbf{e}_z$  and examine the longitudinal channel in the regime where  $\omega \sim k^2 \ll 1$ . In this limit we find that eq. (3.45) becomes

$$\partial_u \sigma^{zz} = -\frac{ik_L^2}{\omega} \frac{\sqrt{-g_{tt}g_{uu}}}{\Sigma_A^z g_{zz}} (\sigma^{zz})^2. \quad (3.60)$$

After inserting for  $\Sigma_A^z$  the solution for this differential equation with initial condition  $\sigma^{zz}(K, u_h) = \sigma_z$  is

$$\frac{1}{\sigma^{zz}(u)} = \frac{1}{\sigma_z} + \frac{ik_L^2}{\omega} \int_u^{u_h} du \frac{-g_B^2 g_{tt} g_{uu}}{\sqrt{-g}}. \quad (3.61)$$

Making now use of the relation  $G_R^{zz}(K) = -\lim_{u \rightarrow 0} i\omega \sigma^{zz}$  we obtain

$$\frac{i\omega}{G_R^{zz}} = -\frac{1}{\sigma_z} - \frac{ik_L^2}{\omega} \Xi^{-1} \quad \text{with } \Xi = \left[ \int_0^{u_h} du \frac{-g_B^2 g_{tt} g_{uu}}{\sqrt{-g}} \right]^{-1}. \quad (3.62)$$

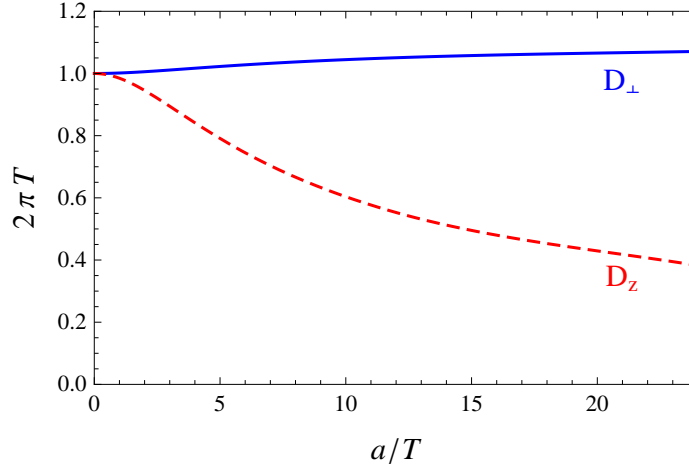


Figure 3.15: Charge diffusion constants along and perpendicular to the anisotropy direction as a function of  $a/T$ .

$\Xi$  is the charge susceptibility. The expression for the retarded correlator is therefore given by

$$G_R^{zz} = \frac{\omega^2 \sigma_z}{i\omega - k_L^2 \sigma_z \Xi^{-1}} \quad (3.63)$$

and we can directly read off the expression for the diffusion constant

$$D_z = \sigma_z \Xi^{-1}, \quad (3.64)$$

which is now not determined by the horizon data only.

If the wave vector points in a perpendicular direction an analogous computation can be done and it is straightforward to calculate

$$D_\perp = \sigma_\perp \Xi^{-1}. \quad (3.65)$$

Both diffusion constants are shown in Fig. 3.15.

We can check the results we just obtained with the help of the membrane paradigm by computing the lowest quasi-normal mode in the diffusive channels. In order to do so we have to solve the differential eqs. (3.18) and (3.21) numerically for the metric of the MT model<sup>8</sup>. Here we want to discuss their asymptotic behavior close to the horizon ( $u = u_h$ ) and the boundary ( $u = 0$ ). We start with the horizon, where the relevant parts of the metric (5.1) take the form

$$g_{tt}(u \approx u_h) = \gamma_t(u - u_h) \quad (3.66)$$

$$g_{uu}(u \approx u_h) = -\frac{\gamma_u}{(u - u_h)}, \quad (3.67)$$

<sup>8</sup>Note that  $g_{vv}$  gets replaced by  $g_{uu}$  for the MT model.

with the strictly positive constants  $\gamma_t = -\mathcal{F}_1 \mathcal{B}_h / e^{\phi_h/2} u_h^2$  and  $\gamma_u = -1/\mathcal{F}_1 e^{\phi_h/2} u_h^2$ . Here and in the following the subscript  $h$  shall always indicate that the function is evaluated at the horizon. The ODE's for both gauge invariant quantities  $E_x(u)$  and  $E_z(u)$  become

$$E''_{x,z}(u) + \frac{1}{u - u_h} E'_{x,z}(u) + \frac{\gamma_u \omega^2}{\gamma_t (u - u_h)^2} E_{x,z}(u) = 0, \quad (3.68)$$

and the characteristic exponents are easily found to be  $\pm i \sqrt{\gamma_u / \gamma_t} \omega$ . The minus sign corresponds to the infalling boundary condition we are interested in.

In contrast, close to the boundary at  $u = 0$  the metric (5.1) takes the form

$$g_{tt} = -\frac{1}{u^2} \quad g_{xx} = g_{zz} = g_{uu} = \frac{1}{u^2} \quad (3.69)$$

and the relevant terms of the ODE are given by

$$E''_{x,z}(u) - \frac{1}{u} E'_{x,z}(u) = 0 \quad (3.70)$$

from which the characteristic exponents are found to be 0 and 2. This implies that the electric fields close to boundary can be written as

$$E_{x,z}(u) = \bar{\mathcal{A}}_{x,z}(\omega, k) + \dots + \bar{\mathcal{B}}_{x,z}(\omega, k) u^2 + \dots, \quad (3.71)$$

where  $\bar{\mathcal{A}}$  and  $\bar{\mathcal{B}}$  are known as connection coefficients. It turns out that the poles of the retarded propagator are obtained if infalling boundary conditions are chosen at the horizon and the connection coefficient of the non normalizable mode at the boundary  $\bar{\mathcal{A}}$  vanishes. This determines the dispersion relation in the hydrodynamic limit  $\omega \ll 1$  and  $q \ll 1$

$$\omega = -i D_{\perp} k^2 \quad \text{for } k \text{ pointing in 1-direction} \quad (3.72)$$

$$\omega = -i D_z k^2 \quad \text{for } k \text{ pointing in } z\text{-direction.} \quad (3.73)$$

We have solved the full ODE's for  $E_x$  and  $E_z$  numerically and found the same results for the diffusion constants as shown in Fig. 3.15. This is reassuring in the sense that it confirms the validity of the membrane paradigm to compute conductivities in our anisotropic setting.

### Spectral functions for wave vector parallel to anisotropy direction

After examining the hydrodynamic regime, we consider the full  $\omega$  and  $\mathbf{k}$  dependence and begin by studying spectral functions for wave vectors along the anisotropy direction. It turns out that now the results depend on both  $a/\mu$  and  $T/\mu$  and we have

$\tilde{\phi}_h$	$u_h$	$a/T$	$T$	$N_c^{-2}s$	$\Delta$	$\epsilon/\epsilon_{iso}$
$-\infty$	1	0	0.318	0.159	0	1
$-21/40$	201/200	1.32	0.318	0.163	0.08	1.01
$3/50$	107/100	6.43	0.318	0.201	-1.00	1.69
$48/625$	7/5	50.51	0.318	0.383	-1.29	$9.42 \cdot 10^3$

Table 3.1: Choice of parameters and corresponding thermodynamic quantities for approximately constant temperature in the anisotropic axion-dilaton gravity dual.

$\tilde{\phi}_h$	$u_h$	$aN_c^{2/3}/s^{1/3}$	$T$	$N_c^{-2}s$	$\Delta$	$\epsilon/\epsilon_{iso}$
$-\infty$	1	0	0.318	0.159	0	1
$-17/50$	41/40	1.13	0.314	0.159	0.18	0.97
$9/250$	6/5	4.23	0.289	0.159	-1.13	1.79
$-619/5000$	2	27.37	0.231	0.159	-1.29	$6.62 \cdot 10^3$

Table 3.2: Choice of parameters and corresponding thermodynamic quantities for approximately constant entropy density in the anisotropic axion-dilaton gravity dual.

different possibilities to compare our findings. Because the MT model is in thermal equilibrium, the temperature of the plasma is well defined, and one possibility is to keep the temperature fixed for different values of anisotropic charge density  $a$ . Equally well we could demand that the entropy density should remain fixed while we vary  $a$ . The model parameters for both cases are shown in Table 3.1 and 3.2 together with some thermodynamic quantities of interest. We emphasize that for small  $a$  we find oblate plasma and for larger  $a$  prolate plasma<sup>9</sup>. We find that the results for spectral functions are qualitatively very similar and therefore we only present plots for constant temperature.

In Fig. 3.16 we plot the transverse part of the spectral function for lightlike momenta. In the  $\omega \rightarrow 0$  limit we recover the DC conductivities perpendicular to the anisotropy direction. The probably most striking difference to the JW model is the behavior for large frequencies where the ratio of spectral function over frequency rises for larger anisotropies. This is in strong contrast to the situation in the JW model, where for large frequencies we always found the same behavior as in the isotropic case, no matter how anisotropic the plasma was. Another important difference is that for the MT model there is no qualitative change when going from an oblate to a prolate plasma. We will also elaborate on this point in chapter 5.

The longitudinal contribution to the spectral function  $\chi_L = \chi_{zz} - \chi_{tt}$  vanishes for

<sup>9</sup>Here we only consider slightly oblate plasma, however, larger  $\Delta$  can also be studied by increasing  $u_h$ .

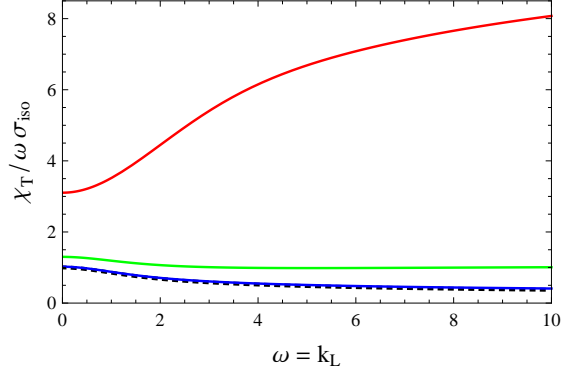


Figure 3.16: Spectral function for lightlike momenta along the anisotropy direction for varying anisotropies at constant temperature:  $a/T = 0$  (isotropic, black dashed line),  $a/T \approx 1.32$  (oblate; blue line),  $a/T \approx 6.43$  (prolate; green line) and  $a/T \approx 50.51$  (prolate; red line).

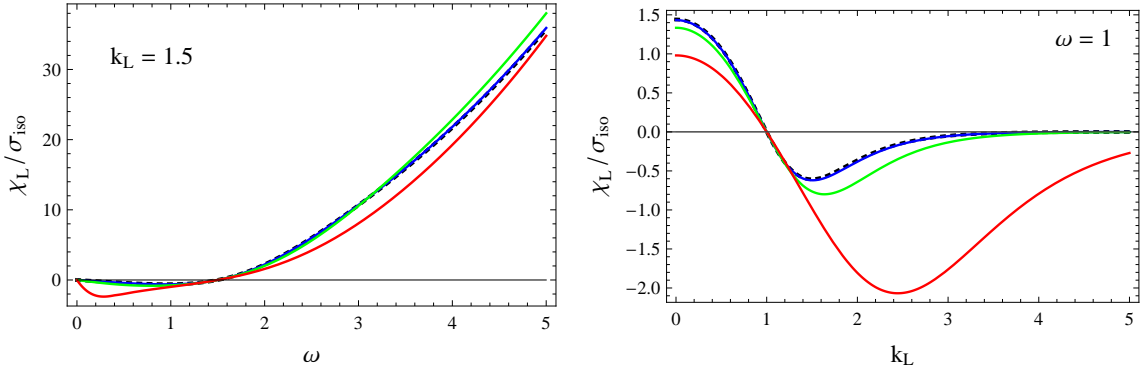


Figure 3.17: Longitudinal part of the spectral function for  $\mathbf{k} = k_L \mathbf{e}_z$  and constant temperature. The color coding is the same as in Fig. 3.16.

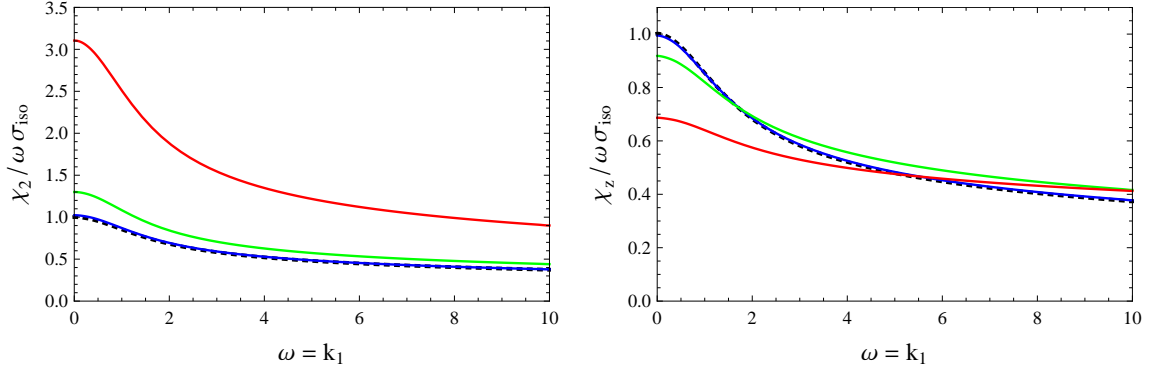


Figure 3.18: Spectral functions for  $\mathbf{k} = k_1 \mathbf{e}_1$  and lightlike momenta. The color coding is the same as in Fig. 3.16.

lightlike momenta as expected. This can be seen in Fig. 3.17, where we have kept either  $k_L$  or  $\omega$  fixed. As before for the JW model the spectral function is negative for spacelike momenta and becomes positive for timelike momenta.

### Spectral functions for wave vector perpendicular to anisotropy direction

When we investigate spectral functions for  $\mathbf{k} = k_1 \mathbf{e}_1$  we have again two modes transverse to the wave vector. For lightlike momenta the results are shown in Fig. 3.18. The zero frequency limit is again consistent with our findings for DC conductivities, which rise in directions perpendicular to the anisotropy and decrease along the anisotropy direction. We also note that at large  $\omega$  the spectral functions order in such a way that the largest value of  $a/T$  is on top. However, the change in the UV behavior compared to the isotropic result is by far not as drastic as for the transverse mode before. For example the ratio  $\chi_{2,z}/\omega$  is monotonically decreasing for increasing  $\omega$ . We checked this numerically up to  $\omega = 100$ .

Finally, in Fig. 3.19  $\chi_1 = \chi_{xx} - \chi_{tt}$  is plotted, where we notice that for timelike momenta the spectral function is the largest for the largest value of  $a/T$ , while the opposite was true for  $\chi_L$  before. However, for spacelike momenta there are no qualitative differences.

### Anisotropy of traced spectral function for lightlike and timelike momenta

As for the JW model we also present the traced spectral function for lightlike and timelike momenta in Figs. 3.20 and 3.21. When we compare the results to the JW model we once again note the significant difference for large  $\omega$  whenever the wave vector is pointing along the anisotropy direction. Furthermore,  $\chi_\mu^\mu$  increases with

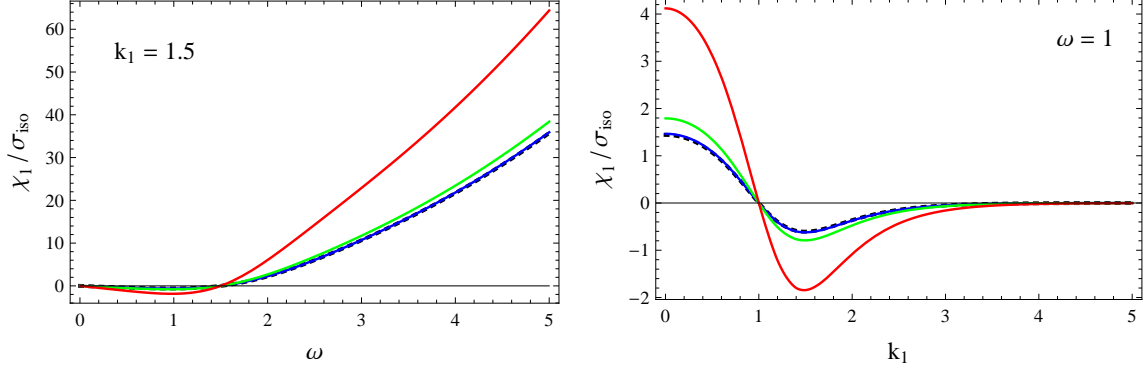


Figure 3.19: Spectral function  $\chi_1$  for  $\mathbf{k} = k_1 \mathbf{e}_1$  and fixed wave vector (left) and frequency (right). The color coding is the same as in Fig. 3.16.

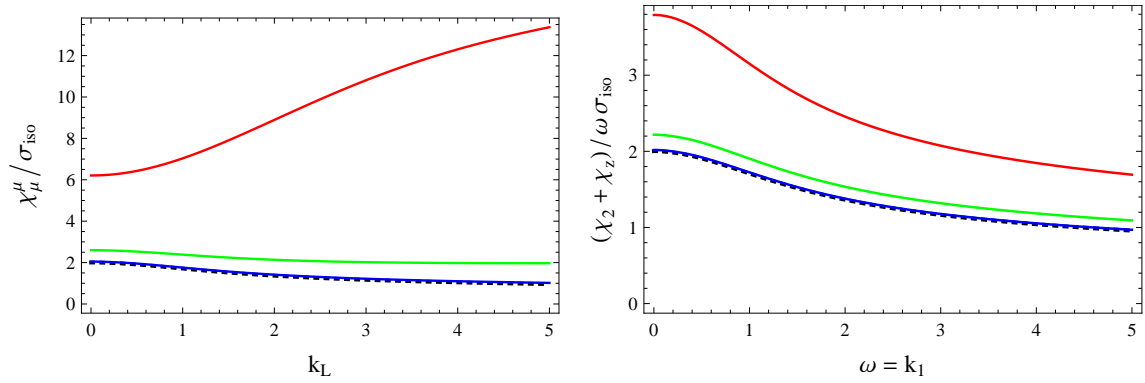


Figure 3.20:  $\chi_\mu^\mu / \omega$  for lightlike momenta with wave vector parallel (left) and perpendicular (right) to the anisotropy direction. The color coding is the same as in Fig. 3.16.

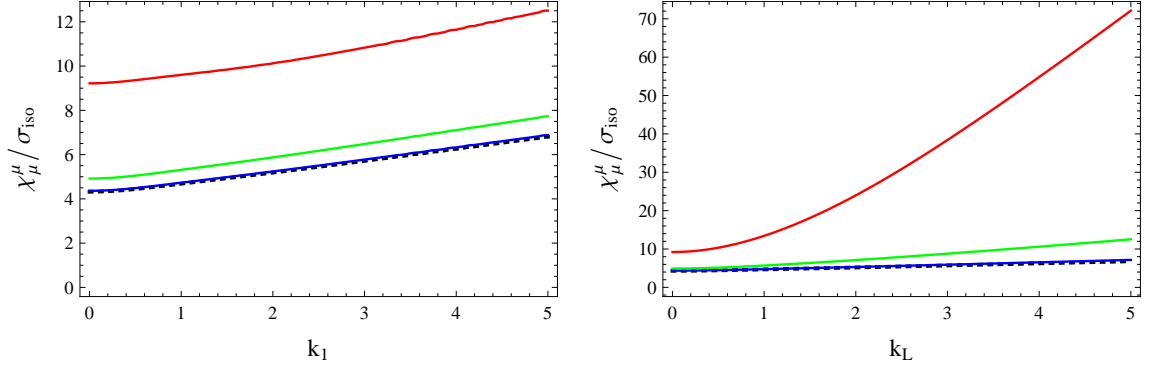


Figure 3.21:  $\chi_\mu^\mu$  for timelike momenta with wave vector parallel (left) and perpendicular (right) to the anisotropy direction. The invariant mass is  $K^2 = -1$ . The color coding is the same as in Fig. 3.16.

increasing anisotropic charge density  $a$  irrelevant whether the plasma is oblate or prolate.

### Photon and dilepton emission

To obtain the photon and dilepton production rates we have to multiply the traced spectral function by the distribution function. The important difference between the JW model and the MT model is that the latter is in thermal equilibrium and therefore the distribution function is the Bose-Einstein distribution function  $f_{BE}(\omega, T) = (\exp(\omega/T) - 1)^{-1}$ . Since the distribution function depends explicitly on the temperature, it will make a difference whether we consider the plasma at constant temperature or at constant entropy density. To keep the entropy density fixed while increasing  $a$  the temperature has to be lowered, leading to a larger suppression in the distribution function. As we have already mentioned the results for the MT model do not change qualitatively when going from an oblate to a prolate plasma. This can also be seen in Fig. 3.22, where we present the production rates for constant temperature and constant entropy density. It is interesting to note that the production of photons with momentum transverse to the anisotropy direction are slightly suppressed compared to photons traveling parallel to the anisotropy direction (this can be better seen in the plot in the right for constant entropy density but is also true for constant temperature). This coincides with the behavior of the JW model in the prolate phase.



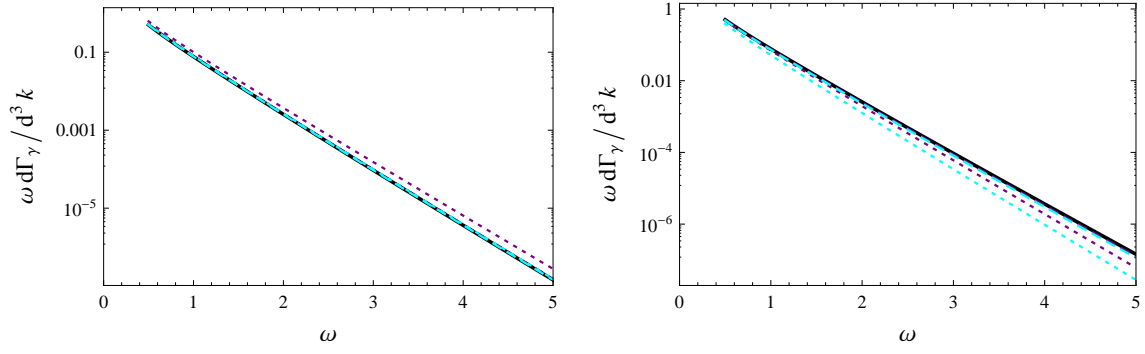


Figure 3.22: Photon production rate in forward (purple) and transverse (cyan) direction. Left: constant temperature with  $a/T \approx 1.32$  (dashed) and  $a/T \approx 6.43$  (dotted). Right: constant entropy density with  $aN_c^{2/3}/s^{1/3} \approx 1.13$  (dashed) and  $aN_c^{2/3}/s^{1/3} \approx 4.23$  (dotted). The isotropic result is shown in black.

## Chapter 4

# Shear Viscosities of Anisotropic Plasma

In [24] the ratio of shear viscosity to entropy density was calculated for an isotropic  $\mathcal{N} = 4$  SYM plasma and found to be  $1/4\pi$ . The computation was done in the limit of infinite coupling by using the holographic duality and essentially boils down to the absorption of gravitons by black holes in the five dimensional gravity dual. In [95] it was then conjectured that  $\eta/s \geq 1/4\pi$  holds for “all relativistic quantum field theories at finite temperature and zero chemical potential”<sup>1</sup>. Later investigations showed that the result  $1/4\pi$  is indeed even more robust and does not depend on details of the system, such as conformality [96] or the introduction of chemical potentials [97, 98, 99]. The only conditions imposed are that we consider two derivative gravity and have isotropy in the spatial directions.

Many attempts to violate this bound were undertaken and we can roughly divide these attempts into two categories. The first is introducing higher derivative terms. These higher derivative terms generically cause undesirable features at the Planck scale, but they can nevertheless be considered as an effective field theory that is only valid up to a certain energy scale. An important finding here was that finite t’Hooft coupling corrections increase  $\eta/s$  consistent with the bound [100]. However, other higher derivative gravity theories that do indeed violate the bound were found too [101, 102, 103], although so far no complete gauge gravity correspondence has been established for finite violations.

The second category of attempts to violate the holographic viscosity bound is considering theories that are not isotropic in the spatial dimensions of the boundary theory. They include the noncommutative plasma [104] and bottom-up models for relativistic superfluids [105, 106, 107]. However, the different shear viscosities in such

---

<sup>1</sup>The bound of  $\eta/s$  is also known as KSS bound (KSS standing for Kovtun, Son and Starinets, the authors of [95]) and holographic shear viscosity bound.

anisotropic systems are either exactly saturating the bound or they are above it. The first successful example to violate  $\eta/s \geq 1/4\pi$  with a two derivative gravity dual was given in [49] and uses the anisotropic axion-dilaton-gravity dual we presented in chapter 2.2. Before we derive this result in the following section we briefly note that it is not possible to compute transport coefficients for the singular-gravity dual of chapter 2.1, because this would involve taking the zero frequency limit, which is not accessible there.

## 4.1 Outline of the computation

In the following we will compute shear viscosities from correlators of stress-energy tensors. A general form of the Kubo formula that relates viscosities to retarded Green's functions is

$$\eta_{\mu\nu\rho\sigma} = \lim_{\omega \rightarrow 0} \text{Im} \left[ \frac{i}{\omega} \int dt d^3x e^{i\omega t} \theta(t) \langle [T_{\mu\nu}(t, 0), T_{\rho\sigma}(0, 0)] \rangle \right], \quad (4.1)$$

where  $\theta(t)$  is the Heaviside step function and has nothing to do with the anisotropic  $\theta$ -parameter in the MT model. We note that the viscosity tensor is a tensor of fourth order. In isotropic systems it turns out that there are only two distinct components namely the shear viscosity and the bulk viscosity. In axisymmetric systems with one preferred direction there are in total five independent components, two of which are shear viscosities (see appendix A.3 and [108, 105, 107]). The careful treatment of the indices of the viscosity tensor will play a crucial role later for interpreting the results for spatially anisotropic gravity duals. Therefore we first want to discuss the general procedure to compute the shear viscosity holographically, while paying attention to the index positions. Using the holographic duality we can relate the expectation value of the energy momentum tensor to the metric by

$$\langle T_{\mu\nu} \rangle = \frac{\delta S[g^{\mu\nu}, \dots]}{\delta g^{\mu\nu}} \Big|_{g^{\mu\nu} = g_{\text{bdry}}^{\mu\nu}}. \quad (4.2)$$

At the level of linear response

$$\langle T_{\mu\nu} \rangle = \frac{\delta S[g^{\mu\nu}, \dots]}{\delta g^{\mu\nu} \delta g^{\rho\sigma}} \Big|_{g^{\mu\nu} = g_{\text{bdry}}^{\mu\nu}} = -G_{\mu\nu\rho\sigma}^R \delta g^{\rho\sigma}. \quad (4.3)$$

To obtain shear viscosities we have to consider off-diagonal components of the stress-energy tensor. Therefore we consider fluctuations of the metric  $\delta g^{ij} = h^{ij}$  with  $i \neq j$  and expand the action to second order in the fluctuations. It turns out that the effective action is that of a scalar if we consider  $\phi = h_i^j$ , therefore calculating  $\eta_{j^i j^i}^i \propto G_{j^i j^i}^{Ri}$ . Finally, we can either use the membrane paradigm or solve the equations of motion for the metric fluctuations numerically. We will do this in detail in the following sections after we have discussed the decomposition of different modes.

## 4.2 Construction of Physical Modes

Additionally to the metric perturbations denoted by  $h_{\mu\nu}$  (we choose a gauge where  $h_{Mu} = 0$ ) we also consider scalar perturbations of the dilaton  $\delta\phi = \varphi$  and the axion  $\delta\chi = \eta$ . First, we consider the case for  $\mathbf{k} = k_L \mathbf{e}_z$  with

$$h_{\mu\nu}(t, z, u) = h_{\mu\nu}(u) e^{-i(\omega t - k_L z)} \quad (4.4)$$

$$\eta(t, z, u) = \eta(u) e^{-i(\omega t - k_L z)} \quad (4.5)$$

$$\varphi(t, z, u) = \varphi(u) e^{-i(\omega t - k_L z)} \quad (4.6)$$

such that the fluctuations do not break the remaining  $O(2)$  symmetry in the  $xy$ -plane. In total the metric tensor has 15 independent components and additionally we have 2 scalar fluctuations. Choosing the gauge  $h_{Mu} = 0$ , 5 of the metric tensor components become constraints and we end up with 7 physical modes. There is still a residual gauge freedom from infinitesimal diffeomorphisms  $x^\mu \rightarrow x^\mu + \Sigma^\mu$  with  $\Sigma^\mu = \Sigma^\mu(u) e^{-i(\omega t - k_L z)}$  left. The fluctuations transform as

$$\delta_\Sigma h_{\mu\nu} = -\partial_\mu \Sigma_\nu - \partial_\nu \Sigma_\mu + 2\Gamma_{\mu\nu}^\rho \Sigma_\rho, \quad (4.7)$$

$$\delta_\Sigma \eta = \eta - \Sigma_\mu \partial^\mu \chi, \quad (4.8)$$

$$\delta_\Sigma \varphi = \varphi - \Sigma_\mu \partial^\mu \phi, \quad (4.9)$$

with  $\Gamma_{\mu\nu}^\rho = \frac{1}{2} g^{\rho\sigma} (\partial_\mu g_{\nu\sigma} + \partial_\nu g_{\sigma\mu} - \partial_\sigma g_{\mu\nu})$  being the Christoffel symbol. All the  $\Sigma$ 's are independent from each other and can be obtained from the constraints  $\delta_\Sigma h_{Mu} = 0$ . To find the physical combinations of the fluctuations we study their behavior under the residual gauge transformations in Table 4.1.

Since the fluctuations neither depend on  $x$  nor on  $y$  we notice immediately that  $h_{xy}$  is already a physical mode and decouples from the rest. This is also known as scalar channel in the terminology of [109]. We note that in the  $O(2)$  symmetric case  $h_{xx} - h_{yy}$  is also gauge invariant and the equation for the corresponding physical mode is identical to  $h_{xy}$  [110]. The two physical modes  $g^{xx}(k_L h_{tx} + \omega h_{xz})$  and  $g^{yy}(k_L h_{ty} + \omega h_{yz})$  are known as shear modes, since in the hydrodynamic regime these modes obey the dispersion relation  $\omega = -D_i \frac{z}{i} k_L^2$  with  $i = x, y$ , such that the diffusion constant  $D_i \frac{z}{i} = \eta_i \frac{z}{i} / (\epsilon + P)$  is related to the shear viscosity. We note that the two scalars  $\varphi$  and  $\eta$  only couple to the sound mode in the  $O(2)$  symmetric case. The choice of physical combinations in that channel is not unique.

The same procedure can be repeated for a wave vector pointing in a perpendicular direction  $\mathbf{k} = k_1 \mathbf{e}_1$  thus breaking the  $O(2)$  symmetry in the  $xy$ -plane. If we choose the 1-direction to be the  $x$ -direction without loss of generality then all fluctuations only depend on  $t$ ,  $x$  and  $u$ . Studying the residual gauge freedom for this case leads to a decomposition into physical modes that is summarized in Table 4.2.

residual gauge freedom	physical modes
$\delta_\Sigma h_{xy} = 0$	$h_{xy}$
$\delta_\Sigma h_{tx} = i\omega \Sigma_x$ $\delta_\Sigma h_{xz} = -ik_L \Sigma_x$	$k_L h_{tx} + \omega h_{xz}$
$\delta_\Sigma h_{ty} = i\omega \Sigma_y$ $\delta_\Sigma h_{yz} = -ik_L \Sigma_y$	$k_L h_{ty} + \omega h_{yz}$
$\delta_\Sigma h_{xx} = \delta_\Sigma h_{yy} = -\frac{g'_{xx}}{g_{uu}} \Sigma_u$ $\delta_\Sigma h_{zz} = -2ik_L \Sigma_z - \frac{g'_{zz}}{g_{uu}} \Sigma_u$ $\delta_\Sigma h_{tz} = i\omega \Sigma_z - ik_L \Sigma_t$ $\delta_\Sigma h_{tt} = 2i\omega \Sigma_t - \frac{g'_{tt}}{g_{uu}} \Sigma_u$ $\delta_\Sigma \eta = -\frac{a}{g_{zz}} \Sigma_z$ $\delta_\Sigma \varphi = -\frac{\varphi'}{g_{uu}}$	<p>7 fluctuations (<math>h_{xx}, h_{yy}, h_{zz}, h_{tz}, h_{tt}, \eta</math> and <math>\varphi</math>)</p> <p>-3 constraints (<math>\Sigma_t, \Sigma_z</math> and <math>\Sigma_u</math>)</p> <p>= 4 physical combinations</p> <p>(<math>h_{xx} - h_{yy}</math> satisfies identical equations as <math>h_{xy}</math>)</p>

Table 4.1: Residual gauge freedom and physical combinations of the fluctuations of the metric  $h_{\mu\nu}$  and the scalars  $\eta$  and  $\varphi$  in the  $O(2)$  symmetric case. Primes denote derivatives with respect to  $u$ .

residual gauge freedom	physical modes
$\delta_\Sigma h_{yz} = 0$	$h_{yz}$
$\delta_\Sigma h_{ty} = i\omega \Sigma_y$ $\delta_\Sigma h_{xy} = -ik_1 \Sigma_y$	$k_1 h_{ty} + \omega h_{xy}$
$\delta_\Sigma h_{tz} = i\omega \Sigma_z$ $\delta_\Sigma h_{xz} = -ik_1 \Sigma_z$ $\delta_\Sigma \eta = -\frac{a}{g_{zz}} \Sigma_z$	<p>3 fluctuations (<math>h_{tz}, h_{xz}</math> and <math>\eta</math>)</p> <p>-1 constraint (<math>\Sigma_z</math>)</p> <p>= 2 physical combinations</p>
$\delta h_{yy} = -\frac{g'_{xx}}{g_{uu}}$ $\delta_\Sigma h_{zz} = -\frac{g'_{zz}}{g_{uu}} \Sigma_u$ $\delta_\Sigma h_{xx} = -2ik_1 \Sigma_x - \frac{g'_{xx}}{g_{uu}} \Sigma_u$ $\delta_\Sigma h_{tx} = i\omega \Sigma_x - ik_1 \Sigma_t$ $\delta_\Sigma h_{tt} = 2i\omega \Sigma_t - \frac{g'_{tt}}{g_{uu}} \Sigma_u$ $\delta_\Sigma \varphi = -\frac{\varphi'}{g_{uu}}$	<p>6 fluctuations (<math>h_{yy}, h_{zz}, h_{xx}, h_{tz}, h_{tt}</math> and <math>\varphi</math>)</p> <p>-3 constraints (<math>\Sigma_t, \Sigma_x</math> and <math>\Sigma_u</math>)</p> <p>= 3 physical combinations</p>

Table 4.2: Residual gauge freedom and physical combinations of the fluctuations of the metric  $h_{\mu\nu}$  and the scalars  $\eta$  and  $\varphi$  in the  $O(2)$  broken case. Primes denote derivatives with respect to  $u$ .

This time  $h_{yz}$  is the scalar channel. Additionally, we have the usual shear channel in the  $xy$ -plane  $g^{yy}(k_1 h_{ty} + \omega h_{xy})$  and also a shear channel that incorporates the fluctuations of the axion. In the limit of  $k_1 \rightarrow 0$   $\eta$  couples only to  $h_{tz}$ , and  $h_{xz}$  decouples. However, for arbitrary  $k_1$  the choice of physical modes in this channel is not unique. The same is true for the remaining 6 fluctuations which must give 3 more physical combinations.

## 4.3 Shear viscosities from Kubo's formula

### 4.3.1 Computing at the horizon

Varying the bulk action of the axion-dilaton-gravity dual given in eq. (2.21) with respect to the metric  $g^{\mu\nu}$  we obtain the equations of motion

$$R_{\mu\nu} - \frac{1}{2}\partial_\mu\phi\partial_\nu\phi - \frac{e^{2\phi}}{2}\partial_\mu\chi\partial_\nu\chi = \frac{1}{2}g_{\mu\nu}\left(\mathcal{R} + 12 - \frac{1}{2}(\partial\phi)^2 - \frac{e^{2\phi}}{2}(\partial\chi)^2\right). \quad (4.10)$$

To first order in the fluctuations  $h_{ij}$  with  $i, j = x, y, z$  and  $i \neq j$  the equations become

$$R_{ij}^{(1)} - \left(\frac{e^{2\phi}}{2}\partial_i\chi\partial_j\chi\right)^{(1)} = \frac{1}{2}h_{ij}A^{(0)} \quad (4.11)$$

with

$$A^{(0)} = \frac{1}{2}\left(\mathcal{R} + 12 - \frac{1}{2}(\partial\phi)^2 - \frac{e^{2\phi}}{2}(\partial\chi)^2\right)^{(0)}. \quad (4.12)$$

The term  $\partial_i\phi\partial_j\phi$  does never appear to linearized order, because  $\phi = \phi(u) + \varphi(t, x, z, u)$ . The axion term can appear for  $\mathbf{k} = k_1\mathbf{e}_x$  and  $h_{xz}$ . However, since we are interested in shear viscosities in this section we can set  $\mathbf{k} = 0$  from the beginning. Therefore  $h_{xy}$  and  $h_{xz}$  decouple from the remaining fluctuations. Alternatively we could restrict ourselves to study only scalar channels according to the previous classifications of physical modes. Then  $h_{xy}$  decouples for  $\mathbf{k} = k_L\mathbf{e}_x$  and  $h_{yz}$  for  $\mathbf{k} = k_1\mathbf{e}_x$ . The effective action quadratic in Fourier modes of metric fluctuations that gives rise to the correct equations of motion is of generic form<sup>2</sup>

$$S_{eff}^{(2)} = \frac{1}{16\pi G} \int \frac{d^4K}{(2\pi)^4} du \left( \psi'_n(-K, u) \mathcal{C}_n^1(K, u) \psi'_n(K, u) + \psi_n(-K, u) \mathcal{C}_n^0(K, u) \psi_n(K, u) \right), \quad (4.13)$$

---

<sup>2</sup>We note that the action obtained by expanding (2.21) to second order in metric fluctuations differs from the effective action (4.13) by total derivative terms of the form  $\partial_u(\psi_n(-K, u)\alpha(u)\psi_n(K, u))$ , where  $\alpha(u)$  is some function of the holographic coordinate. These boundary terms do not change the imaginary part of the Green's function and therefore are irrelevant for the shear viscosity.

where the 3 different scalars are  $\psi_\perp = h_y^x = h_x^y$ ,  $\psi_L = h_z^x = h_x^z$  and  $\psi_{\tilde{L}} = h_x^z = h_z^x$  and the label  $n = \perp, L, \tilde{L}$ . Furthermore, by  $\psi'_n$  we mean  $\partial_u \psi_n$ . The above action can also be written as

$$S_{eff}^{(2)} = \frac{1}{16\pi G} \int \frac{d^4 K}{(2\pi)^4} du \left[ \partial_u (\psi_n \mathcal{C}_n^1 \psi'_n) - \psi_n (\mathcal{C}_n^1 \psi''_n + (\mathcal{C}_n^1)' \psi'_n - \mathcal{C}_n^0 \psi_n) \right], \quad (4.14)$$

where we have not written the dependence on  $K$  and  $u$  explicitly. The first term is a boundary term while the second term gives the equation of motion and vanishes on shell. It is now an easy task to read off the coefficients  $\mathcal{C}_n^0$  and  $\mathcal{C}_n^1$  from the equation of motion for the scalar fields  $\psi_n$ . To write them in a compact form it is necessary to insert the equations of motion at zeroth order. Eventually we find

$$\begin{aligned} \psi_\perp : \quad \mathcal{C}_\perp^1(K, u) &= \frac{\sqrt{-g}}{2g_{uu}} & \mathcal{C}_\perp^0(K, u) &= \frac{\sqrt{-g}}{2} g^{\mu\nu} K_\mu K_\nu \\ \psi_L : \quad \mathcal{C}_L^1(K, u) &= \frac{\sqrt{-g}}{2g_{uu}} \frac{g_{xx}}{g_{zz}} & \mathcal{C}_L^0(K, u) &= \frac{\sqrt{-g}}{2} \frac{g_{xx}}{g_{zz}} g^{\mu\nu} K_\mu K_\nu \\ \psi_{\tilde{L}} : \quad \mathcal{C}_{\tilde{L}}^1(K, u) &= \frac{\sqrt{-g}}{2g_{uu}} \frac{g_{zz}}{g_{xx}} & \mathcal{C}_{\tilde{L}}^0(K, u) &= \frac{\sqrt{-g}}{2} \frac{g_{zz}}{g_{xx}} (g^{\mu\nu} K_\mu K_\nu + g^{zz} a^2 e^{2\phi}). \end{aligned}$$

Above we assume that the  $K$ 's are chosen in each case such that the considered metric fluctuation decouples from all the other fluctuations. We again emphasize that for general  $K$ 's different fluctuations can couple and therefore the equations of motion become more complicated. However, the above expressions are always true for  $\mathbf{k} = 0$ , which is enough to compute shear viscosities.

The conjugate momenta  $\Pi_n$  with respect to the holographic coordinate  $u$  are obtained by

$$\Pi_n(K, u) = \frac{\partial \mathcal{L}_{eff}^{(2)}}{\partial (\partial_u \psi_n(-K, u))} = \frac{\mathcal{C}_n^1(K, u) \partial_u \psi_n(K, u)}{8\pi G} \quad (4.15)$$

and the corresponding flow equations are

$$\partial_u \Pi_n(K, u) = \frac{\partial \mathcal{L}_{eff}^{(2)}}{\partial \psi_n(-K, u)} = \frac{\mathcal{C}_n^0(K, u) \psi_n(K, u)}{8\pi G}. \quad (4.16)$$

According to Kubo's formula the viscosities are obtained from the imaginary part of the zero frequency limit of the retarded correlator between two stress-energy tensors (see eq. (4.1)). The non-diagonal components of the stress energy tensor are related to the scalars  $\psi_n$  and the retarded Green's function for these scalars are

$$G_n^R(K) = - \lim_{u \rightarrow 0} \frac{\Pi_n(K, u)}{\psi_n(K, u)}. \quad (4.17)$$

In this section we stay at the horizon where we can use

$$\partial_u \psi_n(K, u_h) = -\sqrt{-\frac{g_{uu}(u_h)}{g_{tt}(u_h)}} \partial_t \psi_n(K, u_h). \quad (4.18)$$

Therefore at the horizon the shear viscosities can be computed from

$$\eta_n(u_h) = \frac{\Pi_n(K, u_h)}{i\omega \psi_n(K, u_h)} = \frac{1}{8\pi G} \sqrt{-\frac{g_{uu}(u_h)}{g_{tt}(u_h)}} \mathcal{C}_n^1(K, u_h). \quad (4.19)$$

We start by considering  $\psi_\perp = h_y^x = h_x^y$  for which we obtain

$$\eta_\perp(u_h) = \frac{\sqrt{\gamma(u_h)}}{16\pi G} = \frac{s}{4\pi}, \quad (4.20)$$

where  $\gamma = g/g_{tt}g_{uu}$ . The evolution along the holographic coordinate is determined by (4.16) which becomes

$$\partial_u \Pi_\perp(K, u) = \frac{\sqrt{-g}}{16\pi G} g^{\mu\nu} K_\mu K_\nu \psi_\perp(K, u). \quad (4.21)$$

In the hydrodynamic limit ( $K \rightarrow 0$ )  $\partial_u \Pi_\perp = 0$  which implies that the flow of  $\eta_\perp$  along the holographic coordinate is trivial. Therefore the result of the membrane paradigm gives the purely transverse shear viscosity of the boundary theory

$$\eta_{x\ y}^y\ x = \eta_{y\ x}^x\ y = \eta_\perp = \frac{s}{4\pi}. \quad (4.22)$$

We note that the purely transverse shear viscosity saturates the holographic viscosity bound.

Next, we turn to  $\psi_L = h_z^y$ . The corresponding component of the viscosity tensor is<sup>3</sup>

$$\eta_L(u_h) = \frac{\sqrt{\gamma(u_h)} g_{xx}(u_h)}{16\pi G g_{zz}(u_h)} = \frac{s}{4\pi \mathcal{H}(u_h)} < \frac{s}{4\pi} \quad (4.23)$$

for  $a \neq 0$ . In the present case the holographic flow is still trivial in the limit  $K^\mu \rightarrow 0$ , because

$$\partial_u \Pi_L(K, u) = \frac{\sqrt{-g}}{16\pi G} \frac{g_{xx}}{g_{zz}} g^{\mu\nu} K_\mu K_\nu \psi_L(K, u). \quad (4.24)$$

---

<sup>3</sup>For vanishing  $k_1$  both  $h_z^x$  and  $h_z^y$  decouple and give the same result. Therefore the shear viscosity is the same irrespective of which mode we consider.



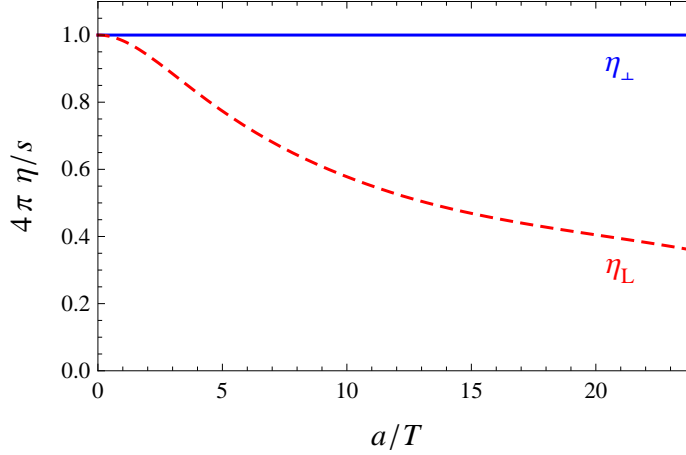


Figure 4.1: Transverse and longitudinal shear viscosities over  $s/4\pi$  as a function of the anisotropy parameter  $a/T$ .

Therefore we conclude that the second independent component in the viscosity tensor that corresponds to a shear viscosity is

$$\eta_y^z{}_y^z = \eta_y^z{}_y^z = \eta_{\perp} = \frac{s}{4\pi\mathcal{H}(u_h)} < \frac{s}{4\pi} \quad (4.25)$$

and violates the conjectured holographic viscosity bound [49]. In Fig. 4.1 we plot the two distinct shear viscosities as a function of  $a/T$ . Similar to the DC conductivities  $\eta_{\perp}$  and  $\eta_L$  are independent of the scale  $\mu$  present in the MT model. Another interesting aspect is to note that the ratios of  $\eta_L/\eta_{\perp}$  and  $\sigma_z/\sigma_{\perp}$  are identical.

In fact we have already found two different shear viscosities in the axisymmetric system we are considering and therefore we should not obtain any new information from the third scalar  $\psi_{\bar{L}} = h_y^z (= h_x^z \text{ for } k_1 = 0)$ . Computing the viscosity component at the horizon we find

$$\eta_{\bar{L}}(u_h) = \frac{\sqrt{\gamma(u_h)} g_{zz}(u_h)}{16\pi G g_{xx}(u_h)} = \frac{s\mathcal{H}(u_h)}{4\pi} > \frac{s}{4\pi} \quad (4.26)$$

and

$$\partial_u \Pi_{\bar{L}}(K, u) = \frac{\sqrt{-g}}{16\pi G} \frac{g_{zz}}{g_{xx}} (g^{tt}\omega^2 + g^{xx}k_1^2 + g^{zz}a^2 e^{2\phi}) \psi_{\perp}(K, u) \quad (4.27)$$

that is nonvanishing for  $\omega, k_1 \rightarrow 0$ . At first this seems disturbing, because it is not immediately obvious that  $\eta_{\bar{L}}$  will be the same as  $\eta_L$  in the boundary theory. However,

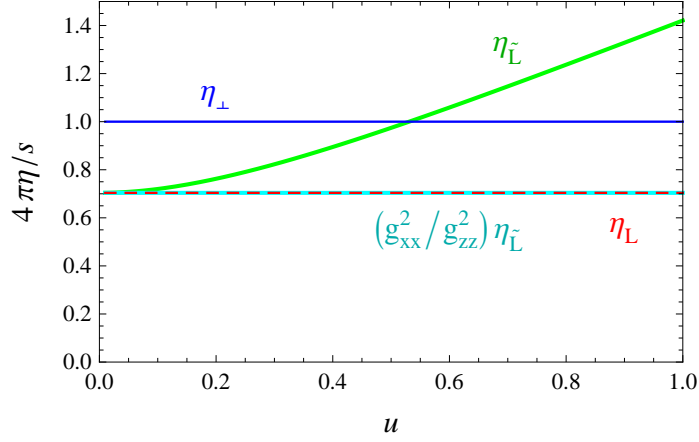


Figure 4.2: Holographic flow of shear viscosities from the horizon at  $u = 1$  to the boundary at  $u = 0$  for  $a/T \approx 6.46$ .

we emphasize that  $g_{zz}(u) \neq g_{xx}(u)$  for  $u \neq 0$  and therefore<sup>4</sup>

$$\eta_{\tilde{L}}(u) = \eta^{x \ x}_{z \ z}(u) = \left( \frac{g_{zz}(u)}{g_{xx}(u)} \right)^2 \eta^{z \ z}_{x \ x} = \left( \frac{g_{zz}(u)}{g_{xx}(u)} \right)^2 \eta_L, \quad (4.28)$$

where in the last step we used the symmetry in the indices for the viscosity tensor. The flow equation  $\partial_u \eta_{\tilde{u}}$  must compensate for the change in the metric factors, because at the boundary  $g_{zz}(0) = g_{xx}(0)$  implying  $\eta_{\tilde{L}}(0) = \eta_L$ . For small values of  $a$  this is shown in [111]; in the following we shall see that this is generally true.

### 4.3.2 From the horizon to the boundary

Alternatively to the approach we presented above, we could have calculated the shear viscosities by a direct numerical evaluation of the Kubo formula

$$\eta_n(u) = \lim_{\omega \rightarrow 0} \text{Im} \frac{\Pi_n(\omega, u)}{\omega \psi_n(\omega, u)} = \lim_{\omega \rightarrow 0} \text{Im} \frac{\mathcal{C}_n^1(\omega, u)}{8\pi G \omega} \frac{\partial_u \psi_n(\omega, u)}{\psi_n(\omega, u)}, \quad (4.29)$$

where we have set the wave vectors to zero. In the end we want to obtain the transport coefficients for the boundary theory and will send  $u \rightarrow 0$ . However, by following the flow of the shear viscosity with respect to  $u$  we are able to prove (4.28) for arbitrarily large  $a$  numerically. The equations of motion can be read off from eq. (4.14). Performing a Frobenius ansatz we find that the characteristic exponents

<sup>4</sup>Note that eq. (4.27) implies that  $\eta_{\tilde{L}}(u)$  will change as we go away from the horizon and therefore  $\eta_{\tilde{L}} = \eta_{\tilde{L}}(u)$ .

close to the horizon are  $\pm i\sqrt{\gamma_u/\gamma_t}\omega$  irrespective of which mode we consider. The minus sign corresponds to infalling boundary conditions and  $\gamma_t$  and  $\gamma_u$  are defined in eqs. (3.66) and (3.67). On the boundary we find the characteristic exponents to be 0 and 4.

The results are shown in Fig. 4.2. We note that the “additional” shear viscosity component at the horizon  $\eta_{\bar{L}}$  flows to the same result as  $\eta_L$  for  $u \rightarrow 0$ . Furthermore, we show that the difference between  $\eta_{\bar{L}}$  and  $\eta_L$  in the bulk is entirely due to the metric factors as given in (4.28). Therefore we have checked our results obtained from the membrane paradigm and also showed that taking the index positions into account we only find two distinct components of the viscosity tensor that are related to shear viscosities in the boundary theory.

## 4.4 Momentum diffusion

To conclude this chapter we study the momentum diffusion. Therefore we consider the two distinct shear modes that do not couple to axion fluctuations. The reasons we do not consider the channel that couples to the axion is that these fluctuations can lead to a nonvanishing  $\langle \mathcal{O}_\chi \rangle$  and therefore the gravitational stress energy tensor is not conserved any longer as can be seen from eq. (2.39). In that case hydrodynamic equations would change and the interpretation of the diffusion constant in the corresponding channel is unclear. As long as we can set the axion fluctuations to zero consistently we are safe and can study momentum diffusion. The hydrodynamic relations are given in appendix A.4.

### 4.4.1 Mapping to vector perturbations

Actually the easiest way to obtain the expression for the momentum diffusion constant is to map the present problem to that of a  $U(1)$  gauge field (that we solved already in section 3.5.2) via Kaluza Klein reduction [91]. We can compactify the  $y$  direction, since none of the fluctuations depends on  $y$ . Then the fields  $A_t = h_{ty}/g_{xx}$ ,  $A_x = h_{xy}/g_{xx}$  and  $A_z = h_{yz}/g_{xx}$  satisfy equations on a 3+1 dimensional background. The corresponding effective action for fluctuations  $A_t(t, x, u)$  and  $A_x(t, x, u)$  or fluctuations  $A_t(t, z, u)$  and  $A_z(t, z, u)$  can be obtained by expanding the axion-dilaton-gravity action to second order

$$S_{eff}^{(2)} = \frac{1}{16\pi G} \int d^5x \left[ \sqrt{-g}^{(2)} 2A^{(0)} + \sqrt{-g}^{(0)} \left( \mathcal{R}^{(2)} - \frac{e^{2\phi}}{2} a^2 g^{zz(2)} \right) \right], \quad (4.30)$$

where  $A^{(0)}$  is given in (4.12). For the fluctuations we consider here we can always write the action (up to boundary terms) in the following form

$$S_{eff}^{(2)} = -\frac{1}{16\pi G} \int dy \int d^4x \sqrt{-g} g_{xx} F_{\alpha\beta} F_{\gamma\delta} g^{\alpha\gamma} g^{\beta\delta}, \quad (4.31)$$

where  $F_{\alpha\beta} = \partial_\alpha A_\beta - \partial_\beta A_\alpha$  and  $\alpha, \beta, \gamma, \delta$  omit the  $y$ -direction. It is noteworthy that as before in the computation of the shear viscosity the mass term proportional to  $a^2$  vanishes after inserting the equations of motion for  $g_{zz}$  at zeroth order. Comparing this effective action with the Maxwell action given in eq. (3.26) we find that by choosing  $g_B^2 = 4\pi G/g_{xx}$  we can map the problem of tensor perturbations to the problem of vector perturbations we have already solved. Therefore using the appropriate coupling constant  $g_B$  we can read off the result for the momentum diffusion constants directly from (3.65) and (3.64). The final expressions are<sup>5</sup>

$$D_{xy} = -\frac{\sqrt{-g(u_h)}}{\sqrt{-g_{tt}(u_h)g_{uu}(u_h)}} \int_0^{u_h} du \frac{g_{uu}(u)g_{tt}(u)}{g_{xx}(u) \sqrt{-g(u)}}, \quad (4.32)$$

$$D_{zy} = -\frac{g_{xx}(u_h) \sqrt{-g(u_h)}}{g_{zz}(u_h) \sqrt{-g_{tt}(u_h)g_{uu}(u_h)}} \int_0^{u_h} du \frac{g_{uu}(u)g_{tt}(u)}{g_{xx}(u) \sqrt{-g(u)}}. \quad (4.33)$$

The diffusion constant for the third shear mode is  $D_{yx} = D_{xy}$ . If we relate these diffusion constants to the shear viscosities we find<sup>6</sup>

$$D_{xy} = \frac{\eta_{yy}^{xx}}{sT} \quad \text{and} \quad D_{zy} = \frac{\eta_{yy}^{zz}}{sT} \quad (4.34)$$

with

$$\frac{1}{sT} = 16\pi G \int_0^{u_h} du \frac{g_{uu}(u)g_{tt}(u)}{g_{xx}(u) \sqrt{-g(u)}}, \quad (4.35)$$

which we also checked numerically.

#### 4.4.2 Lowest lying quasinormal modes

Finally, we want to obtain the momentum diffusion also by solving for the lowest lying quasinormal mode of the retarded propagator of  $Z_1(u) = g^{xx}(k_1 h_{ty}(u) + \omega h_{xy}(u))$

<sup>5</sup>To explain the nomenclature we note that the first index of the diffusion constant indicates the direction of the associated wave vector, while the second index gives information about which direction has been compactified.

<sup>6</sup>When comparing to the results given in appendix A.4 we note that at the boundary  $g_{xx} = g_{zz}$  and indices can be raised and lowered by the Minkowski metric.

and  $Z_3(u) = g^{xx}(k_L h_{ty}(u) + \omega h_{zy}(u))$ , respectively. The corresponding equations of motion are

$$Z_1'' + \frac{1}{2} \left( -\frac{g'_{uu}}{g_{uu}} + \frac{g'_{zz}}{g_{zz}} + \frac{g_{xx}g'_{tt}(\omega^2 g_{xx} - k_1^2 g_{tt}) + 2g_{tt}g'_{xx}(2k_1^2 g_{tt} + \omega^2 g_{xx})}{g_{tt}g_{xx}(k_1^2 g_{tt} + \omega^2 g_{xx})} \right) Z_1' - g_{uu} \left( \frac{\omega^2}{g_{tt}} + \frac{k_1^2}{g_{xx}} \right) Z_1 = 0 \quad (4.36)$$

and

$$Z_3'' + \frac{1}{2} \left( \frac{(g_{tt}g'_{zz} - g_{zz}g'_{tt})(k_L^2 g_{tt} - \omega^2 g_{zz})}{g_{tt}g_{zz}(k_L^2 g_{tt} + \omega^2 g_{zz})} - \frac{g'_{uu}}{g_{uu}} + \frac{4g'_{xx}}{g_{xx}} \right) Z_3' - g_{uu} \left( \frac{\omega^2}{g_{tt}} + \frac{k_L^2}{g_{zz}} \right) Z_3 = 0. \quad (4.37)$$

The characteristic exponents for  $Z_1$  and  $Z_3$  are the same as for the scalar modes  $\psi_n$  that we already discussed. Close to the boundary we can write

$$Z_{1,3}(u) = \bar{\mathcal{A}}_{1,3}(\omega, k_{1,L}) + \dots + \bar{\mathcal{B}}_{1,3}(\omega, k_{1,L})u^4 + \dots \quad (4.38)$$

and the dispersion relation in the hydrodynamic limit can be obtained from

$$\bar{\mathcal{A}}_{1,3}(\omega, k_{1,L}) = 0 \quad \text{for } \omega \ll 1 \text{ and } k_{1,L} \ll 1. \quad (4.39)$$

From the dispersion relation we can extract numerically the diffusion constants  $D_{xy}$  and  $D_{zy}$  and find agreement with the result obtained via the membrane paradigm.

# Chapter 5

## Heavy Quarks

We emphasized in the introduction that important observables to gain insight into the formation of QGP in heavy ion collisions are jet quenching and bound states of heavy quarks. Using the framework of hard-anisotropic-loop effective theory these have been studied with fixed anisotropy as an approximation to the actual dynamical situation [112, 113, 114, 115, 116]. In this section we want to compare the holographic results we obtain by considering the JW model and the MT model with each other but also with the aforementioned weak coupling studies [50]. A further motivation is that the geometry can be probed directly by the hanging strings that are dual to bound states of two infinitely heavy quarks. This gives us a possibility to show the distortions in our anisotropic gravity duals graphically as we go into the bulk. We note that also the drag force acting on a heavy quark moving through the anisotropic plasma of the MT model has been studied in [117, 118, 119] and recently also light quarks were considered [120].

### 5.1 Heavy quark static potential

#### 5.1.1 Holographic computations

We begin by discussing the heavy quark potential obtained from the Wilson-Polyakov loop which is dual to a fundamental string with spacelike separated endpoints at the AdS boundary [121, 122, 123] for the generic form of a metric in the string frame describing stationary but spatially anisotropic geometries<sup>1</sup>

$$ds^2 = g_{tt}(u)^2 dt^2 + g_{xx}(u)(dx^2 + dy^2) + g_{zz}(u)dz^2 + g_{uu}(u)du^2. \quad (5.1)$$

---

<sup>1</sup>The AdS part of the string frame metric of the MT model can be found in eq. (2.18). We also note that in this section we will always refer to the holographic coordinate by  $u$ . For the JW model we simply make the substitution  $u \rightarrow v$ .

The action for the hanging string is

$$S = -\frac{1}{2\pi\alpha'} \int d^2\sigma \sqrt{-h}, \quad (5.2)$$

with  $h_{ab} = g_{MN}\partial_a X^M \partial_b X^N$  being the induced metric on the worldsheet. Here the indices  $a, b$  are either 0 or 1 and  $M, N = \{t, x, y, z, u\}$ . Due to the symmetry in the transverse plane we can always choose a coordinate system such that the  $y$ -coordinate vanishes. Parametrizing the string worldsheet by  $t$  and  $u$  and making a stationary ansatz for  $x = x(u)$  and  $z = z(u)$ , we obtain

$$\begin{aligned} S &= -\frac{1}{2\pi\alpha'} \int dt du \mathcal{L}(x'(u), z'(u), u) \\ &= -\frac{\mathcal{T}}{2\pi\alpha'} \int du \sqrt{-g_{tt}(u)(g_{uu}(u) + g_{xx}(u)x'^2(u) + g_{zz}(u)z'^2(u))}, \end{aligned} \quad (5.3)$$

where primes denote derivatives with respect to the holographic coordinate  $u$  and  $\mathcal{T}$  is a constant coming from the time integration. We need to find the string profile and therefore evaluate the equations of motion for  $x(u)$  and  $z(u)$ , which are of the form

$$-g_{tt}(u)g_{xx}(u)x'(u) = \Pi_x \mathcal{L}(x'(u), z'(u), u), \quad (5.4)$$

$$-g_{tt}(u)g_{zz}(u)z'(u) = \Pi_z \mathcal{L}(x'(u), z'(u), u), \quad (5.5)$$

$\Pi_x$  and  $\Pi_z$  being constants of motion. Disentangling the above equations we end up with

$$x'^2(u) = -\frac{\Pi_x^2 g_{uu}(u) g_{tt}(u) g_{zz}(u)}{g_{xx}(u) \left[ (g_{tt}(u) g_{xx}(u) + \Pi_x^2) (g_{tt}(u) g_{zz}(u) + \Pi_z^2) - \Pi_x^2 \Pi_z^2 \right]} \quad (5.6)$$

$$z'^2(u) = -\frac{\Pi_z^2 g_{uu}(u) g_{tt}(u) g_{xx}(u)}{g_{zz}(u) \left[ (g_{tt}(u) g_{xx}(u) + \Pi_x^2) (g_{tt}(u) g_{zz}(u) + \Pi_z^2) - \Pi_x^2 \Pi_z^2 \right]}. \quad (5.7)$$

For a hanging string that connects two spatially separated points at the boundary we expect  $x'^2(u)$  and  $z'^2(u)$  to become negative for  $u > u_0$ . Since the numerator is manifestly positive (note that in our conventions  $g_{tt}(u)$  is negative for Lorentzian signature) the denominator has to vanish at some point  $u_0$  and then becomes negative for increasing values of  $u$ . This is also in line with the requirement that  $du/dx = du/dz = 0$  at the turning point  $u_0$ . Evaluating the zero in the common factor of the denominators eventually leads to an equation that can be written as

$$\frac{\Pi_x^2}{g_{xx}(u_0)} + \frac{\Pi_z^2}{g_{zz}(u_0)} = -g_{tt}(u_0) > 0. \quad (5.8)$$

This is the defining equation of an ellipse and therefore

$$\Pi_x^2 = -g_{tt}(u_0)g_{xx}(u_0)\sin^2\phi, \quad (5.9)$$

$$\Pi_z^2 = -g_{tt}(u_0)g_{zz}(u_0)\cos^2\phi. \quad (5.10)$$

$x'(u)$  and  $z'(u)$  are completely determined by  $u_0$  and the angle  $\phi$ . To obtain the functions  $x(u)$  and  $z(u)$  we can make one further choice, namely that both  $x$  and  $z$  vanish at the turning point  $u_0$ . It is then easy to find the distance between the two string endpoints

$$L = 2\sqrt{x^2(0) + z^2(0)} \quad (5.11)$$

and the energy of the configuration

$$E^{reg.} = -\frac{S}{\mathcal{T}} - \frac{1}{\pi\alpha'} \int_0^{u_h} du \sqrt{-g_{tt}(u)g_{uu}(u)}. \quad (5.12)$$

To calculate the action above we integrate from  $u = 0$  to the turning point  $u = u_0$  in (5.3), which covers only half of the string and therefore we have to multiply by two in order to obtain the full result. The last term above is the energy of two straight strings hanging from the boundary to the horizon at  $u_h$  and is necessary to regularize the amount of energy of the hanging string. This also means that the connected configuration is energetically favored as long as  $E^{reg.} < 0$ . It can be checked easily that for an isotropic geometry with  $g_{zz}(u) = g_{xx}(u)$  we recover the already well known expression for the heavy quark static potential. If in the anisotropic case we restrict to the simpler situations where the string endpoints are either separated exactly along the  $z$  or  $x$  direction the above equations simplify and we reproduce the same solutions as given previously in [117]. Our expressions above, however, are valid for any separation of the string endpoints in the  $xz$ -plane. The generic situation allows us to probe the geometry by letting the string hang down in the bulk and study how it deforms as a function of  $u$ . The screening length for quarkonium mesons moving through an anisotropic plasma corresponding to the MT model is studied in [124].

### JW model

We start by discussing the results for the JW model, the singular anisotropic gravity dual. In Fig. 5.1 we plot the potential between the two heavy quarks, where we have adjusted the parameter  $A$  of the model such that the energy density is kept constant for different anisotropies. Full (dashed) lines correspond to quarks separated along (transverse to) the direction of anisotropy.

We note that in the oblate phase quarks separated along a transverse direction have a slightly shallower potential and consequently a smaller dissociation distance. (By dissociation distance we are referring to the maximal distance between two



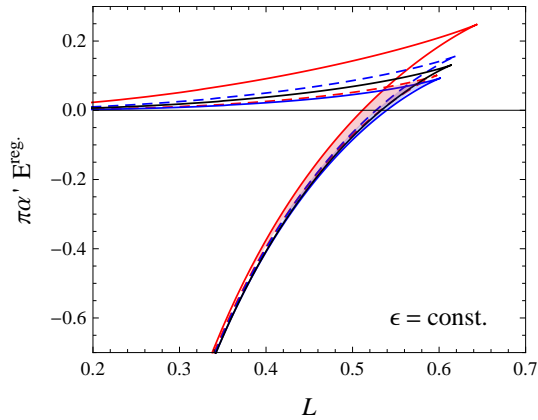


Figure 5.1: Potential energy of heavy quarks in the JW model for plasmas with different anisotropies but constant energy density. The isotropic case corresponds to  $B = 0$  (black lines), oblate anisotropy with  $P_z = 0$  to  $B = \sqrt{2}$  (blue) and prolate anisotropy with  $P_\perp = 0$  to  $B = -\sqrt{6}$  (red). Full (dashed) lines refer to a separation of the quarks along (perpendicular to) the direction of the anisotropy.

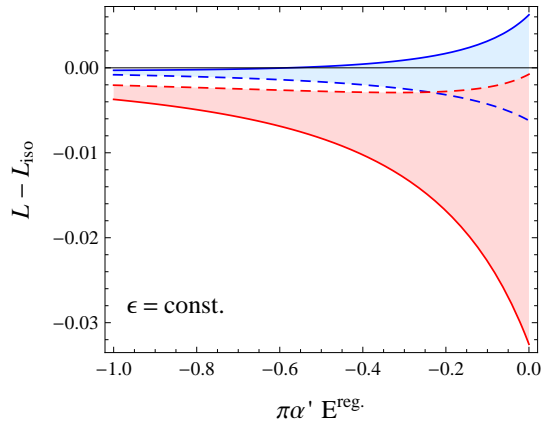


Figure 5.2: Difference in the distance between two connected quarks at a given potential with its isotropic value for a plasma with oblate ( $P_z = 0$ ,  $B = \sqrt{2}$ , blue) and prolate ( $P_\perp = 0$ ,  $B = -\sqrt{6}$ , red) anisotropy at the same energy density. Full (dashed) lines correspond to a separation of the quarks along (perpendicular to) the direction of the anisotropy.

quarks, for which it is still energetically favorable to be connected by a hanging string in the bulk.<sup>2)</sup> For prolate plasmas the heavy quark potential is instead shallower for longitudinally separated quarks than for transverse separations. Evidently the anisotropy only mildly influences the heavy quark potential even though we are considering extreme anisotropic plasmas with  $P_z = 0$  ( $B = \sqrt{2}$ ) and  $P_\perp = 0$  ( $B = -\sqrt{6}$ ). In Fig. 5.2 we have made these small effects more conspicuous by plotting the difference in the separation of two quarks at a given potential energy compared to the isotropic case.

Finally, we want to study the profile of the hanging string in the singular anisotropic geometry of the JW model in more detail. Due to the deformation of the spacetime as we go away from the boundary, the string projected onto the boundary will not be a straight line. The direction of the force acting on the string endpoint at the

<sup>2</sup>Strictly speaking, the dissociation of heavy quarkonia in a medium also depends on the imaginary part of the static potential in the real-time formalism which leads to a finite thermal decay width [125, 116] and which we ignore by only studying Wilson loops in the Euclidean time direction. However, this is valid in the limit of infinitely heavy quarks where the imaginary part is negligible.

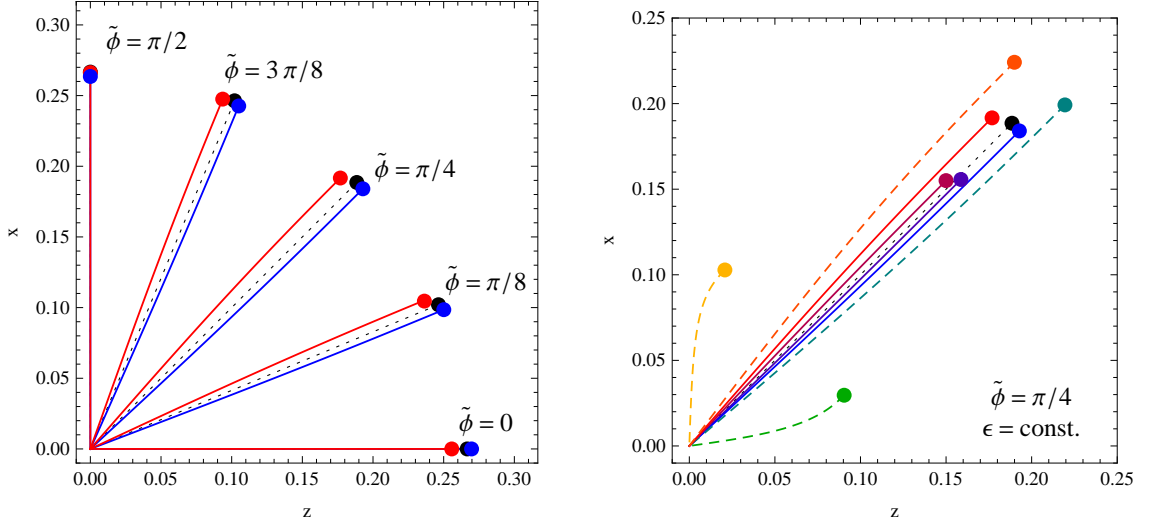


Figure 5.3: String profiles in the JW model for boundary forces acting on the quarks pointing in a fixed direction (as indicated by  $\tilde{\phi}$ ) and projected onto the boundary. The left panel shows profiles for strings at the point of string breaking ( $E^{reg.} = 0$ ) for  $B = 0$  (black, dotted),  $B = \sqrt{2}$  (blue) and  $B = -\sqrt{6}$  (red) with  $\epsilon = \text{const.}$  The right panel shows strings with  $\tilde{\phi} = \pi/4$  but different turning points for the hanging string. For  $B = \sqrt{2}$  ( $B = -\sqrt{6}$ ) the colors going from red to yellow (blue to green) correspond to  $v = \frac{4}{5}v_{sb}$ ,  $v_{sb}$ ,  $\frac{6}{5}v_{sb}$  and  $2v_{sb}$  with  $v_{sb}$  the value at string breaking. Here dashed lines indicate unstable string configurations. (Note that for the JW model the holographic coordinate is  $v$ .)

boundary can be defined by an angle

$$\tan \tilde{\phi} = \frac{\Pi_x}{\Pi_z}. \quad (5.13)$$

If  $\tilde{\phi} = 0$  then the force acts along the  $z$ -axis. One could now think of the following experiment. We act with forces pointing in a specified direction in the  $xz$ -plane on two heavy quarks that are initially close together. We choose the strength of the forces such that the heavy quarks slowly start to separate more until they dissociate. When we keep the direction of the forces fixed the whole time the quarks will, however, not follow a straight line along the force due to the deformation of the space in the holographic coordinate. Instead we observe the behavior shown in Fig. 5.3. We note that for the JW background the strings bend differently depending on the sign of the  $B$  parameter. In the right panel of Fig. 5.3 we consider a string endpoint with a force acting in  $\tilde{\phi} = \pi/4$  direction and vary the depth of the turning point of the hanging string. Therefore, we can probe the geometry up to a certain value of the holographic coordinate. As  $u$  increases the deformation of the string gets stronger and stronger. For strings hanging almost down to the singularity we notice that the

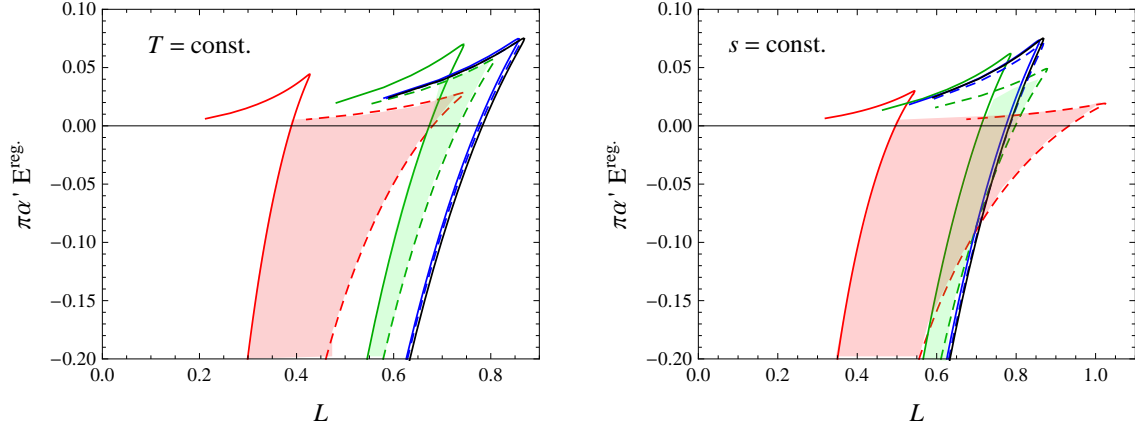


Figure 5.4: Potential for heavy quarks in the MT model. The left panel compares varying anisotropies at constant temperature:  $a/T = 0$  (isotropic; black line),  $a/T \approx 1.32$  (oblate; blue lines),  $a/T \approx 6.43$  (prolate; green) and  $a/T \approx 50.51$  (prolate; red); the right panel at constant entropy density for different anisotropies  $aN_c^{2/3}/s^{1/3} \approx 1.13$  (oblate; blue),  $aN_c^{2/3}/s^{1/3} \approx 4.23$  (prolate; green) and  $aN_c^{2/3}/s^{1/3} \approx 27.37$  (prolate; red). Full (dashed) lines correspond to a separation of the quarks along (perpendicular to) the direction of the anisotropy.

strings get deformed in such a way that they smoothly fit in the remaining space. When we take a look at the line element of the singular gravity dual we note that for  $B > 0$  the  $z$ -direction disappears while for  $B < 0$  the transverse directions vanish and the space degenerates into an infinite line as we go to the singularity. Therefore, in the JW model the pressure anisotropy is encoded very directly in the geometry which is probed by the hanging string.

### MT model

The anisotropic plasma of the MT model dual to axion-dilaton gravity is actually in thermal equilibrium and therefore we can compare the heavy quark static potential at constant temperature and at constant entropy density. The parameters we consider in either case are given in Table 3.1 and in Table 3.2, respectively. The difference can be clearly seen in Fig. 5.4. At fixed temperature the dissociation length gets smaller for any separation in the  $xz$ -plane as we increase the anisotropy parameter  $a$ . At constant entropy density the difference of the dissociation length compared to an isotropic plasma depends on whether we separate the quarks along a transverse direction (string breaking occurs at a larger distance) or along the longitudinal direction (string breaking happens at a smaller distance compared to the isotropic result).

However, regardless of the sign of the pressure anisotropy  $\Delta$  we find that in the

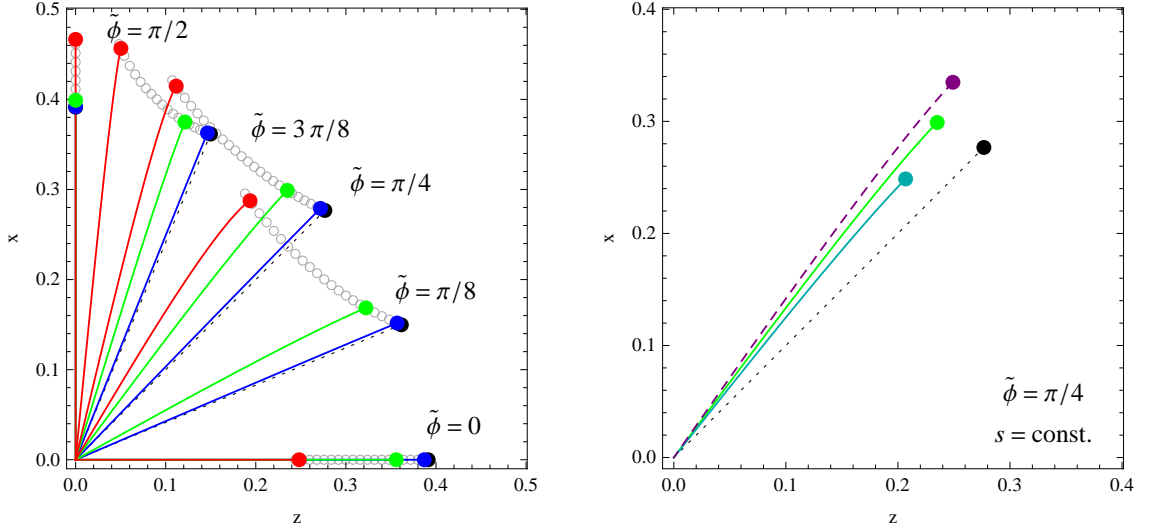


Figure 5.5: String profiles in the MT model for boundary forces acting on the quarks pointing in the same direction (as indicated by  $\tilde{\phi}$ ) and projected onto the boundary. The left panel shows the profiles for strings at the point of string breaking ( $E^{reg} = 0$ ) for  $aN_c^{2/3}/s^{1/3} = 0$  (black, dotted),  $aN_c^{2/3}/s^{1/3} \approx 1.13$  (blue),  $aN_c^{2/3}/s^{1/3} \approx 4.23$  (green) and  $aN_c^{2/3}/s^{1/3} \approx 27.37$  (red) with  $N_c^{-2}s \approx 0.159$ . The right panel shows the profiles for  $aN_c^{2/3}/s^{1/3} \approx 4.23$  and  $\tilde{\phi} = \pi/4$  but at different turning points for the hanging string: at string breaking  $u_{sb}$  (green),  $4u_{sb}/5$  (cyan) and  $6u_{sb}/5$  (purple). Here dashed lines indicate unstable string configurations.

MT model the heavy quark potential is always deeper for transverse separation of the quarks. (Note that the blue lines in the figures correspond to oblate configurations, while the green and red lines are for an increasingly prolate plasma, see Tables 3.1 and 3.2). This is a striking difference to the situation in the JW model where oblate and prolate anisotropies lead to opposite deformations of the heavy quark potential. The situation in the MT model is instead always similar to that in the JW model for prolate anisotropy. This appears to be a direct consequence of the fact that in the MT model  $g_{zz}/g_{xx} = \mathcal{H} \geq 1$  for any  $a$  whereas in the singular geometry of the JW model  $g_{zz}/g_{xx}$  is larger (smaller) than unity for prolate (oblate) pressure anisotropy.

In the remaining plots we will only show the results for constant entropy density keeping in mind that for constant temperature the distance at which the string breaks becomes smaller and smaller as we increase  $a$ .

Finally, we also present the results for strings where the forces acting on the endpoints point in certain directions specified by the angle  $\tilde{\phi}$ . In Fig. 5.5 we also note that the situation is qualitatively the same as in the prolate case for the singular gravity dual. Also indicated in the plot are the trajectories the endpoint of the string

follows as we increase the anisotropy and keep  $\tilde{\phi}$  fixed. Here we see once more that the geometry does change monotonically with increasing  $a$  irrespectively of the behavior of the pressure anisotropy in the boundary theory. In the right panel of Fig. 5.5 we also probe the geometry by varying the location of the turning point of the hanging string.

### 5.1.2 Comparison with weak-coupling calculations

At weak coupling, the real part of the heavy quark potential  $V(\mathbf{r})$  is given by the Fourier transform of the electrostatic propagator. In an axisymmetric situation integration over the azimuth angle leads to

$$V(\mathbf{r}) = -\frac{1}{4\pi^2} \int_0^\infty dk \int_{-1}^1 d\zeta J_0(kr\sqrt{1-\zeta^2}\sin\theta_r) \cos(kr\zeta\cos\theta_r) D_{00}(\omega=0, \mathbf{k}), \quad (5.14)$$

where  $\cos\theta_r = z/r$  and  $\zeta = k_z/k$  with our choice of the anisotropy direction along  $z$ . In the case of the hard anisotropic loops, the propagator  $D_{00}$  is given by

$$D_{00}(\omega=0, \mathbf{k}) = \frac{\mathbf{k}^2 + m_\alpha^2 + m_\gamma^2}{(\mathbf{k}^2 + m_\alpha^2 + m_\gamma^2)(\mathbf{k}^2 + m_\beta^2) - m_\delta^4} \quad (5.15)$$

and has poles at real  $\mathbf{k}$  corresponding to electric plasma instabilities, which are integrated over with a principal value prescription.

In appendix C.1 we discuss that there are two different possibilities to modify the distribution function at weak coupling (C.1) such that the energy density  $\epsilon$  or the hard particle density  $n$  is kept fixed. In this chapter we adjust the hard momentum scale  $p_{\text{hard}}$ , which is in agreement with [116, 126]. In Fig. 5.6 we have evaluated (5.14) with the hard-anisotropic-loop propagator for strongly oblate ( $\xi = 100$ ) and prolate ( $\xi = -0.9$ ) anisotropy (cf. Table C.1 in appendix C.1), keeping alternatively  $n$  and  $\epsilon$  fixed for different anisotropies. The details of the deviation from the isotropic result slightly depend on whether  $n$  or  $\epsilon$  is kept constant, and in either case we find that for oblate anisotropies the heavy quark potential is slightly deeper along the anisotropy direction than transverse to it, while for prolate anisotropies this situation is reversed<sup>3</sup>. In order to make these effects more visible, we also plot  $V(L)$  divided by the modulus of the vacuum (Coulomb) potential,  $1/(4\pi L)$ .

Comparing with the results of the JW model, we find a remarkable qualitative agreement in the dependence on the sign of the anisotropy and the direction of the quark separation. Moreover, the absolute deviation from the isotropic result is rather small both at weak coupling and in the JW model.

<sup>3</sup>This is also true when  $N$  rather than  $p_{\text{hard}}$  is rescaled in (C.1), but this method leads to somewhat stronger differences between fixed  $n$  and fixed  $\epsilon$ .

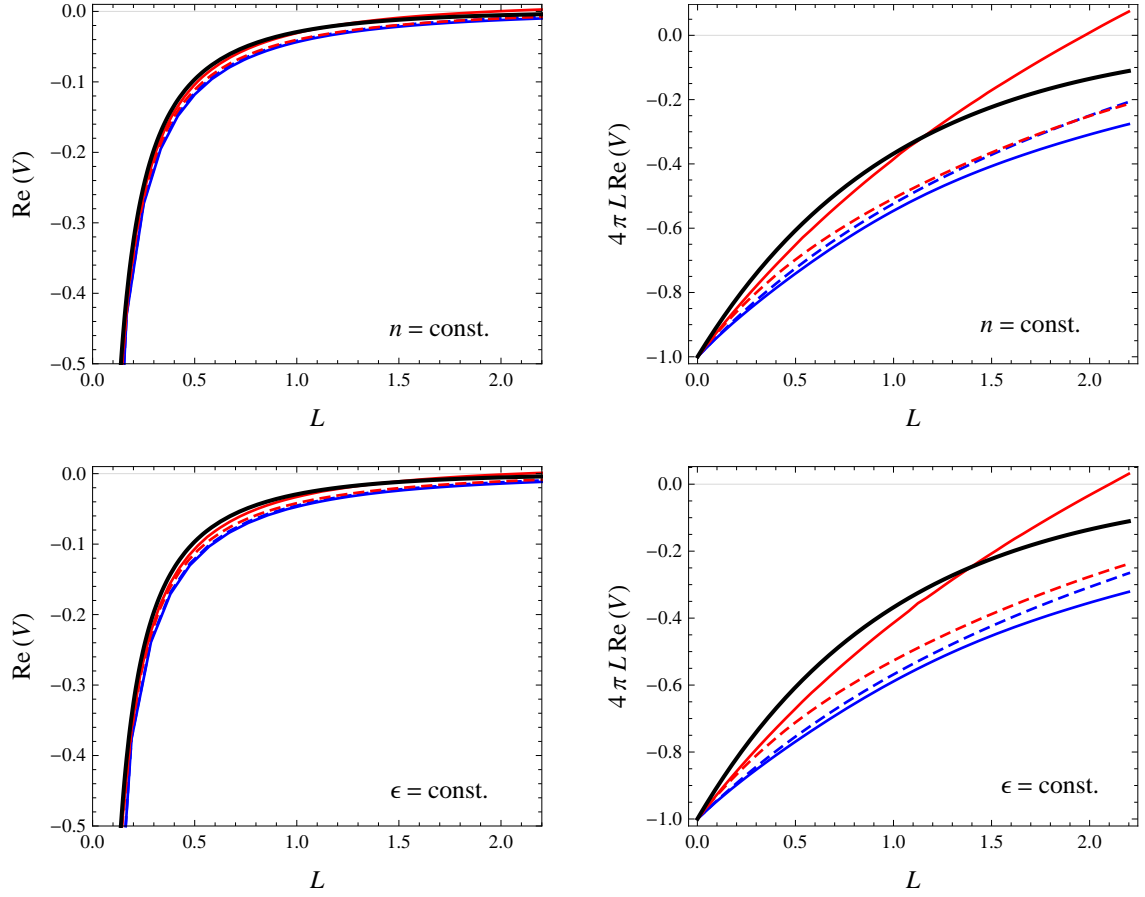


Figure 5.6: Static potential for a weakly coupled anisotropic plasma in the hard anisotropic loop formalism as a function of the quark separation  $L$  (units set by the isotropic Debye mass). The blue and red lines correspond to longitudinal (full) and transverse (dashed) orientation for  $\xi = 100$  and  $\xi = -0.9$ , respectively. The isotropic result is shown in black. In the upper two plots, the particle number density for the anisotropic and the isotropic plasma are the same, in the lower two plots the energy density is kept fixed.

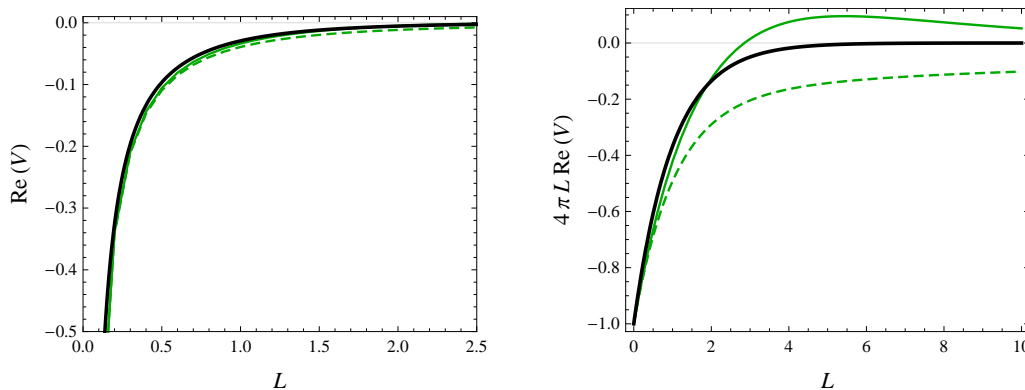


Figure 5.7: Static potential in free anisotropic  $\theta$ -QCD for  $a = 1$ . Full lines correspond to the  $z$ -direction and dashed lines to the  $x$ -direction.

On the other hand, as we have seen above, the MT model has a qualitatively different dependence on the direction of the quark separation in the case of oblate anisotropies (which are usually considered in the context of heavy ion collisions).

Turning to the zero-coupling version of the MT model introduced in section 2.2.3, the heavy quark potential is given by the Fourier transform of

$$D_{00}(\omega = 0, \mathbf{k}) = \frac{1}{\mathbf{k}^2 + a^2(1 - k_{\parallel}^2/\mathbf{k}^2)} \quad (5.16)$$

which is plotted in Fig. 5.7. As we have discussed in Sect. 2.2.3, the high-temperature limit of this weak coupling model corresponds to a prolate anisotropy (in contrast to the holographic MT model), whereas for general  $a/T$  both prolate and oblate anisotropies are possible, depending on the renormalization scale. Curiously enough, the potential shown in Fig. 5.7 (which does not depend on UV renormalization) has qualitatively similar dependence on the direction of quark separation as the holographic MT model (and the hard-anisotropic-loop potential in the prolate case).

We finally also consider the behavior of the quark potentials at large distances. In the two holographic models, there is a finite separation beyond which the string connecting the heavy quarks becomes unstable because strings entering the horizon or the naked singularity are energetically favored, and at a somewhat larger distance even no unstable connecting solution can be found.

To leading order at weak coupling, the isotropic quark potential is simply given by a Yukawa potential with exponential decay at large distance. The anisotropic weak coupling results show curious deviations. In the anisotropic  $\theta$ -deformed zero-coupling case Fig. 5.7 shows a nonmonotonic behavior of the potential along the anisotropy direction such that beyond  $L \sim 5$  (where the potential is actually already extremely small) there is even a repulsive behavior.

Even more curious behavior can be found in the hard-anisotropic-loop potential at large distances. In this case there is nonmonotonic behavior along (transverse to) the anisotropy direction for prolate (oblate) anisotropy, and here the nonmonotonic behavior is moreover oscillatory. This behavior, which has not been noted in the previous studies of the hard anisotropic loop potential [114, 115], is shown in Fig. 5.8, where the potential is plotted at large distances in the  $xz$  plane (enhanced by dividing by the modulus of the vacuum (Coulomb) potential). This oscillatory behavior, which is reminiscent of Friedel oscillations at finite chemical potential (for a recent discussion see [127]), has its origin in the presence of poles in the electrostatic propagator at real wave vector corresponding to electric plasma instabilities. It is, however, rather clear that this curious behavior is devoid of physical implications even at weak coupling, because the plasma instabilities imply that a stationary anisotropy is only a justifiable approximation at sufficiently small time scales and correspondingly small length scales.

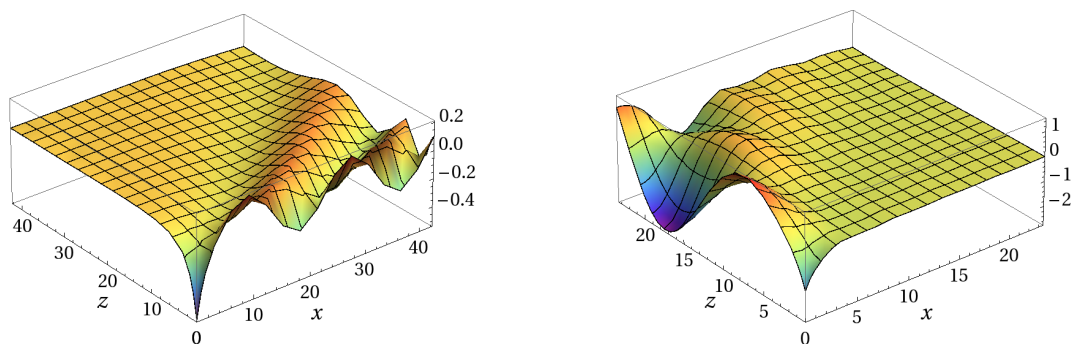


Figure 5.8: Ratio of static potential to vacuum potential for  $\xi = 100$  and  $\xi = -0.9$  at same energy density as in the isotropic plasma.

## 5.2 Jet quenching

### 5.2.1 Holographic calculations

The computation of the jet quenching parameter  $\hat{q}$  for an anisotropic plasma with an axion-dilaton-gravity dual, the MT model, has been presented in [117, 128]. Here we will reproduce the result for the most general case with an ultrarelativistic quark moving in an arbitrary direction [128] and compare the results with those of the singular geometry of the JW model.



According to the prescription of [129, 130] we calculate the string worldsheet with endpoints moving in the same direction at the speed of light and separated a small distance  $l$  along a direction perpendicular to their motion. The jet quenching parameter  $\hat{q}$  can then be obtained from

$$e^{2iS} = \langle W^A(\mathcal{C}_{lightlike}) \rangle = \exp\left(-\frac{L^{-1}l^2}{4\sqrt{2}}\hat{q}\right) + \mathcal{O}\left(\frac{1}{N^2}\right). \quad (5.17)$$

In the following we consider a quark endpoint moving in the  $xz$ -plane. The direction is parametrized by an angle  $\theta$  such that for  $\theta = 0$  the quark moves along the  $z$ -axis. We therefore start by two subsequent coordinate transformations. First, we define

$$Z = z \cos \theta + x \sin \theta, \quad (5.18)$$

$$X = x \cos \theta - z \sin \theta, \quad (5.19)$$

$$Y = y \quad (5.20)$$

and then we introduce light-cone coordinates

$$Z^\pm = \frac{1}{\sqrt{2}}(t \pm Z). \quad (5.21)$$

The metric then takes the form

$$ds^2 = G_{++}(dZ^+)^2 + G_{--}(dZ^-)^2 + 2G_{+-}dZ^+dZ^- + G_{XX}dX^2 + 2G_{X+}dXdZ^+ + 2G_{X-}dXdZ^- + G_{YY}dY^2 + G_{UU}dU^2. \quad (5.22)$$

Writing the new metric coefficients in terms of our original ones we find<sup>4</sup>

$$G_{++} = G_{--} = \frac{1}{2}(g_{tt} + g_{xx} \sin^2 \theta + g_{zz} \cos^2 \theta), \quad (5.23)$$

$$G_{XX} = g_{xx} \cos^2 \theta + g_{zz} \sin^2 \theta, \quad (5.24)$$

$$G_{YY} = g_{yy}, \quad (5.25)$$

$$G_{UU} = g_{uu}, \quad (5.26)$$

$$G_{X+} = -G_{X-} = \frac{1}{\sqrt{2}} \cos \theta \sin \theta (g_{xx} - g_{zz}). \quad (5.27)$$

We choose the worldsheet coordinates  $(\tau, \sigma) = (Z^-, U)$  and let  $Z^+$ ,  $X$  and  $Y$  depend on the holographic coordinate  $U$  in the following. It is interesting that we

---

<sup>4</sup>Here and in the following we will not write the dependence of the metric coefficients on the holographic coordinate  $u$  in order to keep the expressions shorter. There is no danger of confusing at which value of  $u$  we should evaluate the metric coefficient, because the string worldsheet in the calculation of the jet quenching parameter will always have its turning point at the horizon [128].

must allow for a non-constant embedding of the string in  $Z^+$  to find a solution in the most general case. The Nambu-Goto action of the string is then given by

$$S = -\frac{1}{2\pi\alpha'} \int dZ^- \int du \left[ G_{+-}^2 (Z^+)^{\prime 2} + G_{X-}^2 X'^2 + 2G_{+-}G_{X-} (Z^+)' X' \right. \\ \left. - G_{--} (G_{UU} + G_{++} (Z^+)^{\prime 2} + G_{XX} X'^2 + G_{YY} Y'^2 + 2G_{+X} (Z^+)' X') \right]^{\frac{1}{2}}. \quad (5.28)$$

The expression under the square root is actually negative which leads to an imaginary action. The reason is that we consider a spacelike string worldsheet. However, this is expected because it is exactly what we need to obtain a jet quenching parameter that is real.

Since the Lagrangian does not depend on  $Z^+$ ,  $X$  or  $Y$  explicitly we can find three constants of motion  $\Pi_+$ ,  $\Pi_X$  and  $\Pi_Y$ . In the limit where these constants are small<sup>5</sup> we obtain

$$(Z^+)' = c_{++}\Pi_+ + c_{+X}\Pi_X + \mathcal{O}(\Pi^2), \quad (5.29)$$

$$X' = c_{X+}\Pi_+ + c_{XX}\Pi_X + \mathcal{O}(\Pi^2), \quad (5.30)$$

$$Y' = c_{YY}\Pi_Y + \mathcal{O}(\Pi^2). \quad (5.31)$$

In [128] the coefficients  $c$  are given explicitly for the metric of the axion-dilaton-gravity dual. Since we are interested in comparing the results of two different gravity duals we express these coefficients in terms of the general form of the metric given in (5.1)

$$c_{++} = \sqrt{\frac{g_{uu}}{2(g_{tt} + g_{zz} \cos^2 \theta + g_{xx} \sin^2 \theta)}} \frac{g_{tt}(g_{xx} \cos^2 \theta + g_{zz} \sin^2 \theta) + g_{xx}g_{zz}}{g_{tt}g_{xx}g_{zz}}, \quad (5.32)$$

$$c_{XX} = \sqrt{\frac{2g_{uu}}{g_{tt} + g_{zz} \cos^2 \theta + g_{xx} \sin^2 \theta}} \frac{g_{zz} \cos^2 \theta + g_{xx} \sin^2 \theta}{g_{xx}g_{zz}}, \quad (5.33)$$

$$c_{YY} = \sqrt{\frac{2g_{uu}}{g_{tt} + g_{zz} \cos^2 \theta + g_{xx} \sin^2 \theta}} \frac{1}{g_{xx}}, \quad (5.34)$$

$$c_{+X} = c_{X+} = \sqrt{\frac{g_{uu}}{g_{tt} + g_{zz} \cos^2 \theta + g_{xx} \sin^2 \theta}} \frac{(g_{zz} - g_{xx}) \sin \theta \cos \theta}{g_{xx}g_{zz}}. \quad (5.35)$$

This agrees with [128] if we insert the precise form of the metric in the axion-dilaton-gravity case. However, it is now also straightforward to consider any background whose metric is of the form (5.1).

<sup>5</sup>We want to consider small separation lengths  $l$  between the two string endpoints. In [128] it is shown that this corresponds to the limit of small  $\Pi$ 's. As a further remark we note that the worldsheet turning point characterized by  $dU/dX = 0$  (and similarly for  $Z^+$  and  $Y$ ) is located at the horizon.

The string endpoints at the boundary are not separated along the  $Z^+$  direction and integrating (5.29) gives

$$\Pi_+ = -\frac{\int_0^{u_h} du \, c_{+X}}{\int_0^{u_h} du \, c_{++}} \Pi_X. \quad (5.36)$$

Along the  $X$ -axis the separation of the endpoints is  $l \sin \phi$  while in  $Y$ -direction it is  $l \cos \phi$ . The constants of motion are then

$$\Pi_X = \frac{l \sin \phi}{2} \frac{\int_0^{u_h} du \, c_{++}}{\int_0^{u_h} du \, c_{XX} \int_0^{u_h} du \, c_{++} - \left( \int_0^{u_h} du \, c_{+X} \right)^2}, \quad (5.37)$$

$$\Pi_Y = \frac{l \cos \phi}{2} \frac{1}{\int_0^{u_h} du \, c_{YY}}. \quad (5.38)$$

If we insert the expressions (5.29)-(5.31) into the action (5.28) and expand to second order in  $\Pi$ 's we obtain

$$S = \frac{iL^-}{\pi\alpha'} \int_0^{u_h} du \sqrt{G_{--} G_{UU}} \quad (5.39)$$

$$+ \frac{iL^-}{2\pi\alpha'} \int_0^{u_h} du [c_{++}\Pi_+^2 + c_{XX}\Pi_X^2 + 2c_{+X}\Pi_+\Pi_X + c_{YY}\Pi_Y^2].$$

The action is imaginary because we considered a spacelike worldsheet and  $L^-$  is the length of the Wilson line in  $Z^-$ -direction. The first,  $\Pi$  independent term is divergent, however, the jet quenching parameter is proportional to  $l^2$  and therefore just contained in the second finite term. Upon inserting (5.36)-(5.38) into the action and considering the defining relation for the jet quenching parameter (5.17) we eventually obtain

$$\hat{q}_{\theta,\phi} = \frac{\sqrt{2}}{\pi\alpha'} (P(\theta) \sin^2 \phi + Q(\theta) \cos^2 \phi) \quad (5.40)$$

with

$$P(\theta) = \frac{\int_0^{u_h} du \, c_{++}}{\int_0^{u_h} du \, c_{XX} \int_0^{u_h} du \, c_{++} - \left( \int_0^{u_h} du \, c_{+X} \right)^2}, \quad (5.41)$$

$$Q(\theta) = \frac{1}{\int_0^{u_h} du \, c_{YY}}. \quad (5.42)$$

The average

$$\hat{q}_\theta \equiv \frac{1}{2\pi} \int_0^{2\pi} d\phi \, \hat{q}_{\theta,\phi} \equiv \frac{1}{2} (\hat{q}_{\theta,0} + \hat{q}_{\theta,\pi/2}) \equiv \hat{q}_{\theta,\pi/4} \quad (5.43)$$

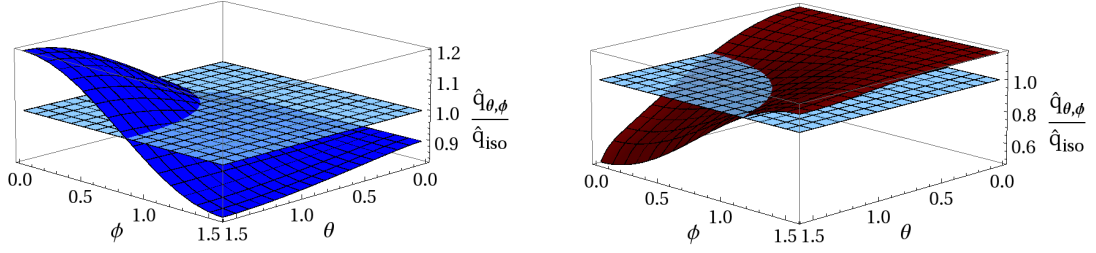


Figure 5.9: Jet quenching parameter normalized to the isotropic result in the JW model. Left panel for an oblate plasma with  $B = \sqrt{2}$ , right panel for a prolate plasma with  $B = -\sqrt{6}$ , with  $\epsilon = \text{const.}$

is the total jet quenching parameter for a quark moving with angle  $\theta$  with respect to the anisotropy direction, while  $\hat{q}_{\theta,\phi}$  contains the information about momentum broadening in directions transverse to the motion of the quark, with  $\phi = 0$  being perpendicular to both the direction of the jet and the anisotropy direction. When  $\theta = 0$ , i.e. the quark moving along the direction of anisotropy,  $\hat{q}_{0,\phi} \equiv \hat{q}_0$  is independent of  $\phi$ . In the context of heavy-ion collisions, one is of course mostly interested in jets at larger  $\theta$ . For  $\theta = \pi/2$  one can define transverse and longitudinal jet quenching parameters

$$\hat{q}_\perp = \hat{q}_{\pi/2,0}, \quad \hat{q}_L = \hat{q}_{\pi/2,\pi/2}. \quad (5.44)$$

In Figures 5.9 and 5.10  $\hat{q}_{\theta,\phi}$  is plotted for oblate and prolate pressure anisotropies in the MT model and in the JW model. Once more we see that in the JW model a different sign of the anisotropy parameter leads to a qualitative change of the result, in particular whether  $\hat{q}_L$  is larger or smaller than  $\hat{q}_\perp$ , while the results for the MT model are more similar to the prolate phase of the JW model, for any parameter  $a$  and thus regardless of the sign of the pressure anisotropy  $\Delta$ .

### 5.2.2 Comparison with weak coupling calculations

Attempts to calculate the anisotropic jet quenching parameters for a quark moving transverse to the anisotropy direction ( $\theta = \pi/2$ ) have been presented in Refs. [112, 113] based on one-loop calculations using hard anisotropic loops. In this situation the presence of spacelike poles in the static gluon propagator leads to nonintegrable singularities. In Ref. [112] it was conjectured that these singularities might get cured by the generation of an imaginary part in the static gluon self energy at higher loop order and this conjecture was used for an estimate of this “anomalous” contribution. While in Ref. [131] this conjecture was refuted, Ref. [113] proposed alternative resolutions, which all point to anomalous contributions of the same sign and angular dependence

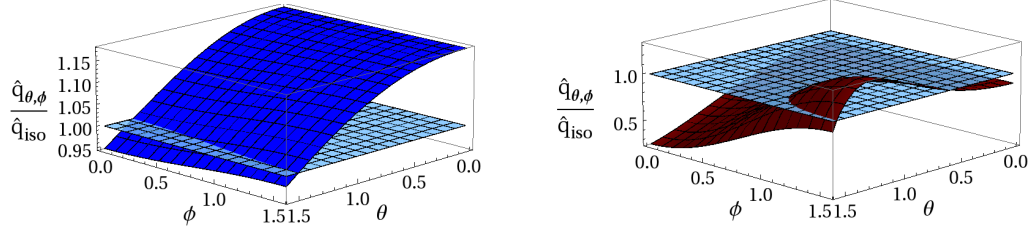


Figure 5.10: Jet quenching parameter normalized to the isotropic result in the MT model. Left panel for a plasma at the same entropy density for  $aN_c^{2/3}/s^{1/3} \approx 1.13$  and  $N_c^{-2}s \approx 0.159$  which corresponds to oblate pressure anisotropy; right panel for prolate pressure anisotropy with  $aN_c^{2/3}/s^{1/3} \approx 27.37$ .

as the infrared-safe regular contributions computed previously in Ref. [112] to leading logarithmic order. For a quark moving with the speed of light and in the limit of small anisotropy parameter  $\xi$ , the regular contribution to  $\hat{q}_\perp$  and  $\hat{q}_L$  was obtained as

$$\hat{q}_{L,\perp}^{\text{reg.}} = \hat{q}_{\text{iso}} \left( 1 \pm \frac{\xi}{3} + O(\xi^2) \right). \quad (5.45)$$

To linear order in  $\xi$ , the anomalous contribution is in fact only present for oblate anisotropy<sup>6</sup> ( $\xi > 0$ ) with

$$\hat{q}_{L,\perp}^{\text{anom.}} = C \hat{q}_{\text{iso}} \left( \frac{\xi}{6} (1 \pm \frac{1}{2}) \Theta(\xi) + O(\xi^2) \right), \quad (5.46)$$

where  $C$  is a positive constant which depending on the physical cutoff for the singularities arising from plasma instabilities may differ from unity and also involve  $\ln(1/\xi)$  [113]. At any rate, to linear order in  $\xi$  the hard-anisotropic-loop calculations of Refs. [112, 113] imply  $\hat{q}_L > \hat{q}_\perp$  for oblate pressure anisotropy, and  $\hat{q}_L < \hat{q}_\perp$  for the prolate case. This result neither agrees with the results of the JW model nor with those of the MT model: in the JW model the ordering of the two jet quenching parameter changes with the sign of the anisotropy, but the ordering is just the opposite. The MT model on the other hand always has  $\hat{q}_L > \hat{q}_\perp$  which agrees with the hard anisotropic loop result in the oblate case, but differs in the prolate case.

It is actually questionable whether the one-loop calculation using hard anisotropic loops is relevant for the physics of a weakly coupled anisotropic quark-gluon plasma. Anisotropic jet quenching could be instead dominated by large chromomagnetic fields generated by plasma instabilities [132, 133]. Because plasma instabilities give rise to  $|B_\perp| > |E_\perp|$  and  $|E_L| > |B_L|$ , it has been argued in Ref. [132] that this would also

<sup>6</sup>Refs. [112, 113] only discussed oblate anisotropies, which have  $m_\alpha^2 \leq 0$  and  $m_\alpha^2 \propto \xi$ . For prolate anisotropy only the last term of Eq. (32) in [113] contributes, which is of order  $\xi^3$ .

give  $\hat{q}_L > \hat{q}_\perp$  for a plasma with oblate anisotropy. In fact, the (different) plasma instabilities for prolate anisotropies equally lead to<sup>7</sup>  $|B_\perp| > |E_\perp|$  and  $|E_L| > |B_L|$ , thus also favoring  $\hat{q}_L > \hat{q}_\perp$ . Perhaps fortuitously, this is in line with the results of the MT model, although the latter of course neglects any dynamics from instabilities and the formation of inhomogeneous configurations<sup>8</sup>.

---

<sup>7</sup>This holds true for both weak fields [35] and nonperturbatively large fields [134].

<sup>8</sup>Note that the fields associated with plasma instabilities at weak coupling have nonvanishing wave number.

# Chapter 6

## Conclusion and Outlook

In the preceding chapters we presented the main results of this thesis. Now we want to wrap up the most important aspects again and give an outlook to possible future extensions.

First of all we should note important characteristics of the two models we considered. The obvious drawback of the JW model is the presence of a naked singularity which makes the validity of the gravity dual questionable. As we have pointed out in chapter 2 we interpret the appearance of the singularity as a breakdown of the stationarity condition we imposed at the beginning. It is encouraging that only the small frequency behavior is altered dramatically when we consider spectral functions of R-current correlators, while for sufficiently large frequencies the modifications due to the anisotropy are mild. The same behavior is also seen in models of holographic thermalization that do not incorporate spatial anisotropies, but nevertheless show the same small  $\omega$  behavior, which is due to the quasi-stationarity condition imposed there [75, 76]. In the context of tensor perturbations the same modifications have been observed [135]. On the other side some qualitative similarities between the hard anisotropic loop effective theory at weak coupling and the JW model at strong coupling have been found, especially for the studies of heavy quark static potentials. The situation is clearly different when we consider the MT model that introduces an anisotropic  $\theta$ -term in the Yang-Mills lagrangian. The boundary theory dual to anisotropic axion-dilaton-gravity is qualitatively different from the hard anisotropic loop effective theory even at a conceptual level. The probably most important difference is that the MT model is always in thermodynamic equilibrium and the anisotropy is not dynamical but held fixed due to an external source. It is surprising that the boundary theory possesses an extremely rich phase diagram for both infinite and zero coupling. In [59] it was noted that the instabilities are reminiscent of instabilities of weakly coupled plasma in the presence of anisotropy. However, in the zero coupling limit of the MT model, where we were able to obtain the propagator and the phase diagram, we found that the thermodynamically unstable phases appear even

though there are no unstable modes. This is in contrast to plasma instabilities in the hard anisotropic loop framework, which are always connected to unstable modes in the propagator. Therefore it is obvious that the instabilities of the MT model are conceptually different than those found for effective theories of anisotropic QGP at weak coupling. When we studied the potential of heavy quarks in chapter 5 we have also seen that the hard anisotropic loop effective theory gives rather different results than even the zero coupling limit of the MT model. It is important to keep these fundamental differences in mind whenever we want to compare the JW model and the MT model qualitatively. Nevertheless it might be of interest to calculate several transport coefficients that are of relevance to heavy-ion phenomenology in the MT model also at weak coupling. Because of the absence of tachyonic modes in the gauge boson spectrum, such calculation are in principle feasible, while the hard anisotropic loop effective theory of a weakly coupled plasma with momentum-space anisotropy typically suffers from nonintegrable singularities.

A very curious result was obtained in the MT model for the spectral function for photons if the wave vector points along the anisotropy. There the UV behavior was strongly modified and a thorough investigation of this phenomenon would be interesting. A first check could be an analytical study of the UV asymptotics for infinitesimal small anisotropic charge density  $a$ . Unfortunately the change in the power law behavior can only be observed for larger  $a$ .

Another interesting finding is the behavior of the jet quenching parameter  $\hat{q}$ . In chapter 5 we found that for the JW model  $\hat{q}_L > \hat{q}_\perp$  ( $\hat{q}_\perp > \hat{q}_L$ ) for prolate (oblate) plasma. The fact that the MT model arrives at  $\hat{q}_L > \hat{q}_\perp$  always seems to be related to the fact that the bulk geometry is uniformly prolate ( $\mathcal{H} > 1$ ), even when the pressure of the dual gauge theory has oblate anisotropy. It would be very exciting to see whether dynamical holographic models of heavy-ion collisions, such as colliding shock waves in AdS [39], where both the bulk geometry and the pressure anisotropy have oblate character, would lead to different results (as the results obtained by the JW model could suggest). This seems to be a most pertinent question since heavy-ion data [136] indeed point towards  $\hat{q}_L > \hat{q}_\perp$ , which weak coupling calculations in an anisotropic plasma appear able to reproduce [112, 113, 132].

At the end of this thesis we should also comment on the longitudinal shear viscosity in the MT model. The result that it violates the holographic viscosity bound is interesting from a purely theoretical point of view, since it demonstrates that no higher derivative terms are needed to find at least one component of the shear viscosity that violates  $\eta/s \geq 1/4\pi$ . Recently, a very similar result has been obtained for another holographic model, where one shear viscosity tends to zero at low temperature [137]. It would be interesting to investigate further anisotropic top-down models (as opposed to anisotropic bottom-up models for which no violation of the holographic viscosity bound has been found so far) and study the behaviour of different shear viscosities. The hope would be that some pattern emerges that would



indicate under which circumstances the holographic viscosity bound can be violated in anisotropic systems. Aside from these theoretical questions the implications of a longitudinal shear viscosity below the KSS bound for hydrodynamic evolution of the QGP produced in heavy ion collisions would be interesting to study. First results [138] obtained by including different shear viscosity components in the numerical code of [139] however suggest that the longitudinal shear viscosity has very little impact on the elliptic flow that is strongly dominated by the shear viscosity in the transverse plane.

# Appendix A

## Basics of Relativistic Hydrodynamics

Hydrodynamics is an effective theory that describes small frequency and large wavelength phenomena of an underlying microscopic theory. It requires certain inputs like the equation of state  $P(\epsilon)$  or viscosities that must be provided either from theoretical computations of the microscopic theory or from experiment. The relevant degrees of freedom for this approach are expectation values of conserved currents such as the stress energy tensor  $T^{\mu\nu}$ . The conservation equation is given by

$$\partial_\mu T^{\mu\nu} = 0. \quad (\text{A.1})$$

It takes a long time for large wavelength excitations to relax because the conserved energy and momentum must be transported over distances of the order of the wavelength. Modes for which the lifetime diverges with their wavelength are therefore known as hydrodynamic modes. For a more detailed discussion of hydrodynamics in the context of heavy ion collisions see [140, 141, 142].

### A.1 Ideal Hydrodynamics

In an ideal relativistic fluid, where there is no dissipation, the stress energy tensor can be built out of the energy density  $\epsilon$ , the pressure  $P$ , the fluid velocity vector  $u^\mu$  (with  $u_\mu u^\mu = -1$ ) and the metric  $g^{\mu\nu}$

$$T_{ideal}^{\mu\nu} = \epsilon u^\mu u^\nu + P \Delta^{\mu\nu} \quad \text{with} \quad \Delta^{\mu\nu} = g^{\mu\nu} + u^\mu u^\nu \quad (\text{A.2})$$

In the local rest frame of the fluid  $u^\mu = (1, \mathbf{0})$  and  $T_{ideal}^\mu{}_\nu = \text{diag}(\epsilon, P, P, P)$ . From the conservation equation (A.1) we obtain

$$u^\mu \partial_\mu \epsilon = -(\epsilon + P) \partial_\mu u^\mu, \quad (\text{A.3})$$

$$(\epsilon + P) u^\mu \partial_\mu u^\rho = -\Delta^{\rho\nu} \partial_\nu P, \quad (\text{A.4})$$

after contraction with  $u^\nu$  and  $\Delta_\nu^\rho$ , respectively. As a consequence of the first equation the entropy is conserved. This becomes transparent when we use the thermodynamic relations  $\epsilon + P = Ts$  and  $Tds = d\epsilon$  to rewrite it and find

$$\partial_\mu(su^\mu) = 0. \quad (\text{A.5})$$

The second equation states that the change in velocity of a fluid cell is proportional to the pressure gradient. It is at the basis of the result that ideal hydrodynamic evolution transforms initial spacetime anisotropy leading to pressure gradients to a strong elliptic flow surprisingly similar to that observed in noncentral heavy ion collisions.

## A.2 Adding Dissipation

Dissipation arises from the leading gradient terms in the energy momentum tensor  $T^{\mu\nu} = T_{ideal}^{\mu\nu} + \Pi^{\mu\nu}$  with

$$\Pi^{\mu\nu} = -\eta\sigma^{\mu\nu} - \zeta\Delta^{\mu\nu}\partial \cdot u, \quad (\text{A.6})$$

where  $\sigma^{\mu\nu} = \Delta^{\mu\alpha}\Delta^{\nu\beta}(\partial_\alpha u_\beta + \partial_\beta u_\alpha) - \frac{2}{3}\Delta^{\mu\nu}\partial \cdot u$ . Here  $\eta$  and  $\zeta$  are the shear and bulk viscosity, respectively. In a system with no additional conserved charges than energy and momentum all momentum density is due to the flow of energy density which leads to the condition  $u_\mu\Pi^{\mu\nu} = 0$ . In general we can view this condition as a choice of frame for the definition of the fluid four-velocity, sometimes referred to as Landau-Lifshitz frame. While in the Landau-Lifshitz frame the energy density is at rest, in systems with additional charges other choices are possible, e. g. the Eckart frame where the charge density is at rest [141]. Taking the dissipative terms into account the longitudinal and transverse components of the conservation equation are

$$\partial_\mu(su^\mu) = \frac{\eta}{T}\sigma^{\mu\nu}\sigma_{\mu\nu} + \frac{\zeta}{T}(\partial \cdot u)^2 \quad (\text{A.7})$$

$$u^\mu\partial_\mu u^\rho = -\frac{1}{sT}\Delta_\nu^\rho(\partial^\nu P - \eta\partial_\mu\sigma^{\mu\nu} - \zeta\partial^\nu(\partial \cdot u)). \quad (\text{A.8})$$

Since dissipation can only increase the entropy density from eq. (A.7) we find that  $\eta, \zeta \geq 0$ . Furthermore, shear viscosity tends to decrease the effect of the pressure gradient. Hydrodynamic evolution in viscous systems washes out the initial spacetime anisotropy present in noncentral heavy ion collisions. Therefore, we can restrict the maximal value of the shear viscosity by measuring the elliptic flow and it turns out that  $\eta/s$  has to be remarkably small to fit the experimental data.

The first-order expression for  $\Pi^{\mu\nu}$  we have given in this section turns out to be not suitable for numerical computations. The reason is that truncating the gradient

expansion after the leading term leads to acausal propagation of certain modes. The problem can be solved by taking higher orders into account. Discussions of second-order viscous hydrodynamics can be found e.g. in [143, 144, 145, 146].

### A.3 Anisotropic Hydrodynamics

Systems that are homogeneous but anisotropic are well known in nonrelativistic hydrodynamics. Examples are nematic liquid crystals, which have one preferred axis characterized by the director field  $\mathbf{n}$ , but do not depend on the direction ( $\mathbf{n}$  and  $-\mathbf{n}$  are physically equivalent). These liquid crystals possess five first-order dissipative coefficients, of which two are shear viscosities [108].

The relativistic version of a homogeneous but anisotropic energy momentum tensor neglecting dissipation is given by

$$T_{ideal}^{\mu\nu} = \epsilon u^\mu u^\nu + P_\perp \Delta^{\mu\nu} + \delta_{\mathbf{n}} \Delta_\alpha^\mu \Delta_\beta^\nu n^\alpha n^\beta, \quad (\text{A.9})$$

where the pressure along the director field  $P_{\mathbf{n}} = P_\perp + \delta_{\mathbf{n}}$ . Adding first order gradient terms we can write the dissipative part as

$$\Pi^{\mu\nu} = -\eta^{\mu\nu\rho\sigma} u_{\rho\sigma}, \quad (\text{A.10})$$

where we have used  $u_{\rho\sigma} = \frac{1}{2}(\partial_\rho u_\sigma + \partial_\sigma u_\rho)$ . In the Landau-Lifshitz frame  $u_\mu \Pi^{\mu\nu} = 0$  and therefore the viscosity tensor has nonvanishing components only in the spatial direction. In general there are 21 independent components, but in the case of interest to us, where the fluid has only one preferred axis, this reduces to five independent components. When we specify the  $z$ -direction as the preferred direction in our plasma these are  $\eta^{xxxx} = \eta^{yyyy}$ ,  $\eta^{zzzz}$ ,  $\eta^{xxzz} = \eta^{yyzz}$ ,  $\eta^{xyxy}$  and  $\eta^{xzzz} = \eta^{yzyz}$ , with the last two being shear viscosities. In principle further transport coefficients can arise from derivatives of the director field. However, in this work we only consider a constant preferred direction and therefore do not discuss the most general case. In the context of relativistic superfluids a discussion of viscosities in the anisotropic case can be found in the appendix of [105, 107].

### A.4 Momentum Diffusion

In this section we calculate the diffusion constants for momentum diffusion by considering small fluctuations in the energy density  $\epsilon = \epsilon_0 + \delta\epsilon$ , the transverse pressure  $P_\perp = P_\perp^0 + \delta P_\perp$ , the pressure difference  $\delta_z = \delta_z^0 + \delta\delta_z$  and the velocity vector whose components are  $u^0 = 1 + \mathcal{O}(\mathbf{u}^2)$  and  $\mathbf{u} \ll 1$ . To first order in the small quantities the

conservation equation  $\partial_0 T^{0y} = -\partial_x T^{xy} - \partial_y T^{yy} - \partial_z T^{zy}$  gives

$$\begin{aligned} -i\omega(\epsilon_0 + P_\perp^0)u^y = & -\eta_{xy}^{xy}(k_x k^x u^y + k_x k^y u^x) + ik_y \delta P_\perp - 2\eta_{yy}^{yy} k_y k^y u^y \\ & - \eta_{zy}^{zy}(k_z k^z u^y + k_z k^y u^z). \end{aligned} \quad (\text{A.11})$$

For  $k_y = 0$  and  $k_z = 0$  we find the dispersion relation of the transverse shear mode

$$\omega = -i \frac{\eta_{xy}^{xy}}{\epsilon_0 + P_\perp^0} k_x k^x, \quad (\text{A.12})$$

while for  $k_y = 0$  and  $k_x = 0$  we obtain

$$\omega = -i \frac{\eta_{zy}^{zy}}{\epsilon_0 + P_\perp^0} k_z k^z. \quad (\text{A.13})$$

If we instead start from the conservation equation  $\partial_\mu T^{\mu z}$  and set  $k_z = 0$  and  $k_y = 0$  the dispersion relation we get is

$$\omega = -i \frac{\eta_{xz}^{xz}}{\epsilon_0 + P_\perp^0 + \delta_z^0} k_x k^x. \quad (\text{A.14})$$

In the MT model the entropy density is given by  $s = (\epsilon_0 + P_\perp^0)/T$  and therefore the diffusion constants obtained from (A.12) and (A.13) are

$$D_{xy} = \frac{\eta_{xy}^{xy}}{sT} \quad \text{and} \quad D_{zy} = \frac{\eta_{zy}^{zy}}{sT}, \quad (\text{A.15})$$

respectively. The final diffusion constant we could in principle obtain from (A.14) is related to a shear mode that couples to axion fluctuations. However, then the stress energy tensor obtained by varying with respect to the metric is not conserved any longer and therefore the hydrodynamic equations we consider here are not applicable. We will not study this channel in this thesis.

# Appendix B

## Ingredients of the string theoretic foundation of AdS/CFT

In this appendix we want to review in a more formal way the original arguments for the holographic duality [20] (see also the detailed AdS/CFT reviews [147, 148, 149] and string theory text books [150, 151, 152]). An important role play objects in string theory called D-branes. The “D” stands for Dirichlet and a  $Dp$ -brane is a  $(p + 1)$ -dimensional hyperplane with  $p$  spatial dimensions on which open strings can end. These D-branes can be studied in different limits in order to learn something about their properties. We start by discussing two limits and then present the argument for the holographic duality. Finally, we will discuss holographic renormalization, which plays an important role in applying the duality.

### B.1 D-branes and Yang-Mills theory

In string theory  $Dp$ -branes carry Ramond-Ramond (RR) charge and if we place  $N$   $Dp$ -branes on top of each other, the resulting  $(p + 1)$ -dimensional hyperplane carries exactly  $N$  units of the  $(p + 1)$ -form  $C_{p+1}$  charge. There exist electrically and magnetically charged D-branes with the magnetic dual form

$$d\tilde{C}_{D-p-3} = \tilde{F}_{D-p-2} = \star F_{p+2} = \star dC_{p+1} \quad (\text{B.1})$$

with  $D$  being the dimension of the spacetime. Magnetic and electric charges have to obey the Dirac quantization condition  $Q_p \tilde{Q}_{D-p-4} = 2\pi k$  with  $k \in \mathbb{Z}$ .

If we attach an open string endpoint to the  $Dp$ -brane it must obey Neumann boundary conditions along the  $(p + 1)$  directions and Dirichlet boundary conditions along the transverse directions. In type IIB (IIA) string theory half of the supersymmetry is preserved if  $p$  is odd (even). If we consider a stack of  $N$   $Dp$ -branes the open string endpoints carry Chan Patton factors and the low energy effective theory of

open strings on the stack of D $p$ -branes is a  $U(N)$  gauge theory in  $(p+1)$  dimensions with 16 supercharges. The full low energy effective action taking into account closed and open string excitations can be schematically written as

$$S = S_{\text{bulk}} + S_{\text{brane}} + S_{\text{interaction}}. \quad (\text{B.2})$$

If we take all energies to be small or equivalently take the characteristic scale of the theory, the string length,  $l_s \rightarrow 0$  keeping all other dimensionless parameters (like  $N$  or  $g_s$ ) finite,  $S_{\text{interaction}}$  vanishes and we end up having a free bulk supergravity in 10 dimensions from the closed strings and a  $(p+1)$  dimensional super Yang-Mills (SYM) theory from the open strings. This description is good in string perturbation theory which is valid for  $g_s N \ll 1$ .

## B.2 D-branes and Supergravity

Another possibility to obtain information about D-branes is to consider the classical supergravity limit where the action in the string frame becomes

$$S = \frac{1}{(2\pi)^7 l_s^8} \int d^{10}x \sqrt{-g} \left( e^{-2\Phi} (\mathcal{R} + 4(\partial\phi)^2) - \frac{2}{(8-p)!} F_{p+2}^2 \right), \quad (\text{B.3})$$

with  $l_s$  being the string length,  $\phi$  the dilation and  $F_{p+2} = dC_{p+1}$ .

We are interested in a solution of a flat  $p$ -brane that is charged under  $C_{p+1}$ . An appropriate ansatz for the metric is

$$ds_{10}^2 = \frac{-f(r)dt^2 + \sum_i^p dx^i dx^i}{\sqrt{H_p(r)}} + \sqrt{H_p(r)} \left( \frac{dr^2}{f(r)} + r^2 d\Omega_{8-p}^2 \right) \quad (\text{B.4})$$

and after solving the equations of motion we obtain

$$e^{2\phi} = g_s^2 H_p^{(3-p)/2}(r), \quad (\text{B.5})$$

with  $H_p(r) = 1 + L^{7-p}/r^{7-p}$  and  $f(r) = 1 - r_0^{7-p}/r^{7-p}$ . One can also obtain the expression for the  $C_{p+1}$  form, the charge  $N$  and the asymptotic ADM mass  $M$  (see e.g. [152]). We note that for  $r \rightarrow \infty$  the metric becomes that of flat ten dimensional space. Extremal branes with  $r_0 = 0$  and  $(2\pi)^p g_s l_s^{p+1} M = N$  are BPS states and preserve half of the spacetime supersymmetry. The near horizon region, also called the “throat”, is obtained in the limit of small  $r$  where we can write the metric as

$$ds_{10}^2 = \sqrt{\frac{r^{7-p}}{L^{7-p}}} \left( -dt^2 + \sum_i^p dx^i dx^i \right) + \sqrt{\frac{L^{7-p}}{r^{7-p}}} \left( dr^2 + r^2 d\Omega_{8-p}^2 \right). \quad (\text{B.6})$$

The throat size is proportional to the charge

$$\left(\frac{L}{2\pi l_s}\right)^{7-p} = \frac{g_s N}{7-p} \frac{\Gamma(\frac{9-p}{2})}{2\pi^{(9-p)/2}}. \quad (\text{B.7})$$

In this section we are considering classical supergravity and this is only justified if the curvature of the  $p$ -brane geometry is small compared to the string scale, so that stringy corrections are negligible. This implies  $L \gg l_s$ . Additionally, we want to suppress loop correction and therefore also the effective string coupling  $e^\phi$  must be kept small. This is easy to achieve for  $p = 3$  where the dilaton is constant and therefore  $e^\phi$  can be set to a small value by demanding  $g_s < 1$ . Eventually, we find using the relation between  $L$  and  $N$  that the supergravity description is valid for  $1 \ll g_s N < N$ . We emphasize that this is the opposite limit than in the previous section. For  $p \neq 3$  the metric is singular at  $r = 0$  and the classical supergravity approximation is valid only in a limited region.

To conclude this section we write down the near horizon geometry in the extremal case for  $p = 3$

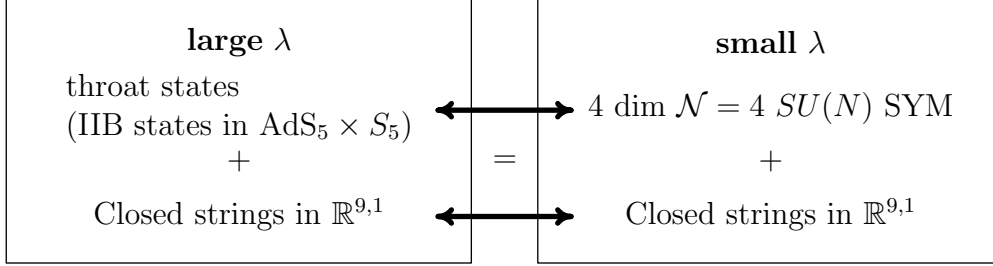
$$ds_{10}^2 = \frac{r^2}{L^2} (-dt^2 + \sum_i^3 dx^i dx^i) + \frac{L^2}{r^2} dr^2 + L^2 d\Omega_5^2, \quad (\text{B.8})$$

which is a direct product of a five-sphere and  $\text{AdS}_5$ . To compare it to the metric we write down in the introduction (1.6) we need to transform  $r \rightarrow L^2/v$ .

### B.3 Statement of the Duality

In the following we will concentrate on the famous example of D3-branes in type IIB string theory. According to the previous sections we can then consider two different approximations in the limits  $g_s N \ll 1$  and  $g_s N \gg 1$ . For  $g_s N \ll 1$  we can use perturbative string theory around flat spacetime and in section B.1 we found that the low energy description of open strings ending in D3-branes is  $\mathcal{N} = 4$  SYM theory living in four dimensions. For  $g_s N \gg 1$  a good approximation is given in terms of perturbation theory around a curved spacetime with no branes and no open strings which is classical type IIB supergravity theory. To find the duality we have to concentrate on the low energy limit in both cases. We have already discussed that for small  $g_s N$  we then obtain a free 10 dimensional supergravity for the closed strings and an  $\mathcal{N} = 4$  SYM theory in 4 dimensions for the open strings. For large  $g_s N$  we find two kinds of low energy excitations. First of all there are massless excitations with large wavelength. Due to the large wavelength they can not resolve the throat and decouple from the near horizon region. The second kind of low energy excitations are states that can have any energy, but are at small  $r$  and get redshifted because  $\sqrt{g_{tt}} \rightarrow 0$  for  $r \rightarrow 0$ . Therefore, we end up with





where we have introduced the t'Hooft coupling  $\lambda = 4\pi g_s N = g_{YM}^2 N$ . If we assume that taking the low energy limit commutes with changing  $\lambda$  we can state that  $\mathcal{N} = 4$  SYM theory is identical to full string theory in  $\text{AdS}_5 \times S_5$ . In order for a gravity theory to be a good approximation for string theory we have to ensure that  $L/l_s \gg 1$ , which can be achieved by taking the limit where at first  $g_s \rightarrow 0$  and  $N \rightarrow \infty$  such that  $\lambda = \text{const.}$  and in the end we take  $\lambda \rightarrow \infty$ . Therefore it becomes possible to investigate strongly coupled  $\mathcal{N} = 4$  SYM theory by studying a gravity theory in  $\text{AdS}_5 \times S_5$ .

Here a comment is in order about the gauge group  $SU(N)$ . The gauge group generated by a stack of  $N$  D3-branes is  $U(N)$ , which itself is equivalent to a free supersymmetric  $U(1)$  theory and an  $SU(N)$  theory. Since on the  $\text{AdS}_5 \times S_5$  side of the duality all the excitations couple to gravity the  $U(1)$  factor is not included in the duality, but can be thought of as representing the free motion of the position of the D3-branes.

Finally, let us mention the bulk field and boundary operator correspondence. For example, we consider an additional term in the gauge theory action of the form

$$\int d^4x \phi_0(x) \mathcal{O}(x). \quad (\text{B.9})$$

$\phi_0(x)$  corresponds to the boundary value of a scalar field, for example the dilaton (then the operator would correspond to the Lagrangian density operator), such that  $\phi(x, u)|_{u=0} = \phi_0(x)$  and  $u = 0$  corresponds to the boundary of  $\text{AdS}_5$ . Therefore, we could equally well formulate the AdS/CFT correspondence as

$$\langle e^{\int d^4x \phi_0(x) \mathcal{O}(x)} \rangle_{CFT_4} = \mathcal{Z}_{string} [\phi(x, u)|_{u=0} = u^{4-\Delta} \phi_0(x)], \quad (\text{B.10})$$

where  $\Delta$  is the scaling dimension of the operator  $\mathcal{O}$ . This relation between the generating functionals can be used to calculate correlators.

## B.4 Holographic Renormalization

When we attempt to compute  $n$ -point correlators with use of eq. (B.10), we encounter divergencies. These are the well known UV divergencies on the gauge theory side,

but also appear in the gravity theory. To obtain finite results we have to employ a procedure called holographic renormalization [53, 153, 154].

We consider a spacetime that is asymptotically AdS and has the metric

$$ds^2 = \frac{d\rho^2}{4\rho^2} + \frac{1}{\rho} g_{\mu\nu}(x, \rho) dx^\mu dx^\nu \quad (\text{B.11})$$

$$g_{\mu\nu}(x, \rho) = g_{(0)\mu\nu}(x) + g_{(2)\mu\nu}(x)\rho + \dots, \quad (\text{B.12})$$

where  $\rho = v^2$  (and  $v$  is the holographic coordinate in Fefferman-Graham coordinates). Suppressing all spacetime and internal indices we denote a generic bulk field by  $\mathcal{F}(x, \rho)$  and its near-boundary behavior is determined by

$$\mathcal{F}(x, \rho) = \rho^m \left( f_{(0)}(x) + f_{(2)}(x)\rho + \dots + \rho^n (f_{(2n)}(x) + \tilde{f}_{(2n)}(x) \ln \rho) + \dots \right). \quad (\text{B.13})$$

The asymptotic behaviors of the two solutions of the equations of motion for  $\mathcal{F}$  are  $\rho^m$  and  $\rho^{m+n}$ . If  $n$  was not an integer, the logarithmic term would not be present. It turns out that  $f_{(0)}$  is the field source of the theory and  $f_{(2)}, \dots, f_{(2n-2)}$  and  $\tilde{f}_{(2n)}$  are local functions of  $f_{(0)}$ .  $\tilde{f}_{(2n)}$  is related to conformal anomalies.  $f_{(2n)}$  is not determined by the near-boundary analysis and is related to the exact 1-point function of the corresponding operator  $\mathcal{O}_{\mathcal{F}}$ .

Next, we calculate the on-shell action of  $\mathcal{F}$  and evaluate the boundary terms at  $\rho = \epsilon$ . A finite number of terms diverge as  $\epsilon \rightarrow 0$  and the on-shell action takes the form

$$S_{\text{o.s.}}[f_{(0)}, \epsilon] = \int_{\rho=\epsilon} d^d x \sqrt{|g_{(0)}|} (\epsilon^{-\nu} a_{(0)} + \epsilon^{-\nu+1} a_{(2)} + \dots - \ln \epsilon a_{(2\nu)} + \mathcal{O}(\epsilon^0)), \quad (\text{B.14})$$

with  $\nu > 0$  that only depends on the scale dimension of the dual operator. In the above expression all  $a_{(2k)}$ 's are local functions of  $f_{(0)}$ . The action can be made finite by adding counterterms

$$S_{\text{c.t.}}[\mathcal{F}(x, \epsilon), \epsilon] = -\text{divergent terms of } S_{\text{o.s.}}[f_{(0)}, \epsilon]. \quad (\text{B.15})$$

This step requires an inversion of eq. (B.13) up to the desired order. The subtracted action

$$S_{\text{sub}}[\mathcal{F}(x, \epsilon), \epsilon] = S_{\text{o.s.}}[f_{(0)}, \epsilon] + S_{\text{c.t.}}[\mathcal{F}(x, \epsilon), \epsilon] \quad (\text{B.16})$$

has a finite  $\epsilon \rightarrow 0$  limit and the renormalized action is

$$S_{\text{ren}}[f_{(0)}] = \lim_{\epsilon \rightarrow 0} S_{\text{sub}}[\mathcal{F}(x, \epsilon), \epsilon]. \quad (\text{B.17})$$

Eventually we can obtain the  $n$ -point function by functional differentiation. For the 1-point function in the presence of sources we get

$$\langle \mathcal{O}_{\mathcal{F}} \rangle = \frac{1}{\sqrt{|g_{(0)}|}} \frac{\delta S_{\text{ren}}}{\delta f_{(0)}} = \lim_{\epsilon \rightarrow 0} \left( \frac{1}{\epsilon^{d/2-m} \sqrt{|\gamma|}} \frac{\delta S_{\text{sub}}}{\delta \mathcal{F}(x, \epsilon)} \right), \quad (\text{B.18})$$

where  $\gamma_{\mu\nu} = g_{\mu\nu}(x, \epsilon)/\epsilon$  is the induced metric at the regulated surface  $\rho = \epsilon$ . For the simplest example, the massive scalar field, all the steps are discussed explicitly in [154, 9].

To conclude we state the general results for the stress-energy tensor, which is the dual operator to the metric, in  $d = 4$  dimensions [53]. The general form of  $g_{\mu\nu}$  close to the boundary is

$$g_{\mu\nu}(x, \rho) = g_{(0)\mu\nu} + \dots + \rho^2 g_{(4)\mu\nu} + h_{(4)\mu\nu} \rho^2 \ln \rho + \dots \quad (\text{B.19})$$

Solving Einstein's equations we find

$$g_{(4)\mu\nu} = \frac{1}{8} g_{(0)\mu\nu} \left( (\text{Tr} g_{(2)})^2 - \text{Tr} g_{(2)}^2 \right) + \frac{1}{2} (g_{(2)})_{\mu\nu}^2 - \frac{1}{4} g_{(2)\mu\nu} \text{Tr} g_{(2)} + t_{\mu\nu}, \quad (\text{B.20})$$

with the symmetric tensor  $t_{\mu\nu}$  obeying the relations

$$\nabla^\mu t_{\mu\nu} = 0, \quad \text{Tr } t = -\frac{1}{4} \left( (\text{Tr} g_{(2)})^2 - \text{Tr} g_{(2)}^2 \right). \quad (\text{B.21})$$

Here  $\nabla^\mu$  is the covariant derivative constructed from  $g_{\mu\nu}$ . After performing the procedure of holographic renormalization we find

$$\langle T_{\mu\nu} \rangle = \frac{1}{8\pi G_N} (2t_{\mu\nu} + 3h_{(4)\mu\nu}) \text{ and } \langle T_\mu^\mu \rangle = \frac{1}{16\pi G_N} (-2a_{(4)}). \quad (\text{B.22})$$

We note that  $a_{(4)}$  is the analog of the term multiplying  $\ln \epsilon$  in eq. (B.14) and is related to  $h_{(4)}$ . In conformal theories  $\langle T_\mu^\mu \rangle = 0$  and therefore  $a_{(4)}$  and  $h_{(4)\mu\nu}$  vanish. However, if  $h_{(4)\mu\nu}$  does not vanish, it turns out that its contribution to the stress-energy tensor is renormalization scheme dependent. The scheme independent part of  $T_{\mu\nu}$  can then be given as

$$\begin{aligned} \langle T_{\mu\nu} \rangle = \frac{4}{16\pi G_N} & \left( g_{(4)\mu\nu} - \frac{1}{8} g_{(0)\mu\nu} ((\text{Tr} g_{(2)})^2 + \text{Tr} g_{(2)}^2) \right. \\ & \left. - \frac{1}{2} (g_{(2)})_{\mu\nu}^2 + \frac{1}{4} g_{(2)\mu\nu} \text{Tr} g_{(2)} \right). \end{aligned} \quad (\text{B.23})$$

# Appendix C

## Hard-anisotropic-loop effective theory

In the main body of the text we often attempt to compare our findings to weakly coupled anisotropic plasma. A lot of computations in the literature have been done in the “hard anisotropic loop” (HAL) framework [155]. This is a generalization of the “hard thermal loop” (HTL) [156] effective theory that describes collective behavior in thermal equilibrium. In this appendix we summarize important aspects needed for the comparisons done in the main body of this thesis and refer the interested reader to the original publications for details.

### C.1 Distribution functions and normalization

In a weakly coupled (nearly collisionless) ultrarelativistic gauge theory plasma there is a hierarchy of scales, with hard scales  $p$  defined as typical energies and momenta of plasma constituents, and soft scales  $gp$ , with coupling constant  $g \ll 1$ , pertaining to leading-order collective phenomena such as Debye screening and plasmon masses. With anisotropic distribution functions for hard particles, the corresponding “hard anisotropic loop” effective theory involves a rich spectrum of stable and unstable modes at momentum scales  $gp$ , which have been worked out completely for axisymmetric deformations of distribution functions of the form [30]

$$f(\mathbf{p}, \xi, p_{hard}) = N(\xi) f_{iso}(\sqrt{p_{\perp}^2 + \xi p_z^2}, p_{hard}) = \frac{N(\xi)}{\exp(\sqrt{p_{\perp}^2 + \xi p_z^2}/p_{hard}) \mp 1}, \quad (\text{C.1})$$

where the sign depends on whether we consider bosons or fermions. Here the anisotropy is along the  $z$ -direction and  $N(\xi)$  is some renormalization factor with  $N(0) = 1$  for vanishing anisotropy parameter  $\xi$ . A prolate momentum distribution is obtained for  $-1 < \xi < 0$ , whereas  $\xi > 0$  parametrizes oblate momentum distributions.  $p_{hard}$  is

$\xi$	$\Delta$	$N^{(n)}$	$N^{(\epsilon)}$	$p_{\text{hard}}^{(n)}/T$	$p_{\text{hard}}^{(\epsilon)}/T$
-0.9	-0.8365	0.3162	0.1678	0.681	0.640
0	0	1	1	1	1
10	6.442	3.317	4.075	1.491	1.421
100	55.72	10.05	12.74	2.158	1.889

Table C.1: Anisotropy parameters in the hard anisotropic loop effective theory

the momentum scale of the hard particles that is equal to the temperature in the isotropic case.

The stress-energy tensor for deformed distributions functions is given by

$$T^{\mu\nu} = N_{eff} \int \frac{d^3\mathbf{p}}{(2\pi)^3} p^\mu p^\nu f(\mathbf{p}). \quad (\text{C.2})$$

While the pressure anisotropy  $\Delta = P_\perp/P_z - 1$  is directly determined by  $\xi$  (see Table C.1), a comparison of quantities at different anisotropy is rather ambiguous [126]. This could be done, e.g., by keeping the number density or the energy density fixed, but in both cases it also depends on whether this is done by adjusting the normalization  $N$  or the parameter  $p_{\text{hard}}$ . Keeping number densities of hard particles fixed by adjusting  $N$ , as done in Ref. [157, 115], leads to  $N^{(n)}(\xi) = \sqrt{1+\xi}$ , whereas constant energy density in hard particles requires  $N^{(\epsilon)}(\xi) = \mathcal{R}^{-1}(\xi)$  with

$$\mathcal{R}(\xi) = \begin{cases} \frac{1}{2}[(1+\xi)^{-1} + \xi^{-1/2}\arctan(\sqrt{\xi})] & \text{for } \xi > 0 \\ \frac{1}{2}[(1-\xi)^{-1} + (-\xi)^{-1/2}\text{atanh}(\sqrt{-\xi})] & \text{for } \xi < 0 \end{cases} \quad (\text{C.3})$$

Alternatively, one could compare isotropic and anisotropic plasmas by fixing  $N = 1$  and adjusting  $p_{\text{hard}}$ . Keeping the number density constant requires

$$p_{\text{hard}}^{(n)} = (1+\xi)^{1/6}T, \quad (\text{C.4})$$

whereas for constant energy density one has

$$p_{\text{hard}}^{(\epsilon)} = \mathcal{R}^{-1/4}(\xi)T, \quad (\text{C.5})$$

with  $T = p_{\text{hard}}|_{\xi=0}$ .

## C.2 Relation to holographic models

### C.2.1 JW model

The anisotropy parameters  $B$  and  $\xi$  can be related by comparing the pressure anisotropies, but it is important to note that HAL only covers the range where both  $P_z$  and  $P_\perp$  are positive.

$B$	$\xi$	$P_L/\epsilon$	$P_T/\epsilon$
-4	-	3	-1
$-\sqrt{6}$	-1	1	0
-1	-0.69675	0.5620	0.2190
-0.1	-0.1160	0.35556	0.3222
0	0	1/3	1/3
0.1	0.1355	0.3111	0.3444
1	4.8102	0.1047	0.4477
$\sqrt{2}$	$\infty$	0	1/2
$\sqrt{12}$	-	-1	1

Table C.2: Relation between different anisotropy parameters

Using the analytic expressions for  $\epsilon$ ,  $P_\perp$  and  $P_z$  of [34] the relation between  $\xi$  and  $B$  is given by

$$\frac{\sqrt{36 - 2B^2} + 2B}{\sqrt{36 - 2B^2} - 4B} = \frac{\xi - 1}{2} + \frac{\xi}{(\xi + 1)\xi^{-1/2} \operatorname{atan} \xi^{1/2} - 1}. \quad (\text{C.6})$$

For small anisotropies  $\xi = \frac{5}{4}B + O(B^2)$ . In Table C.2 we give the corresponding  $\xi$  explicitly for certain values of  $B$ .

### C.2.2 MT model

There is no precise relation between the parameters of the MT model and those of HAL effective theory. For example for any  $\Delta \geq 0$  we can find two distinct configurations in the MT model that would give the same pressure anisotropy. Additionally to the relation between parameters being not unique there are also conceptual differences. While the anisotropically  $\theta$ -deformed theory describes a medium in thermal equilibrium, HAL does not.

On some occasions we nevertheless try to compare the models qualitatively mentioning differences when going from oblate to prolate plasma.

# Appendix D

## Details of the anisotropic axion-dilaton-gravity dual

In this section we want to fill in the gaps in section 2.2 and present in detail our procedure to obtain the numerical solution.

### D.1 Equations of motion

The equations for the functions in the line element which can be extracted from six independent Einstein and dilaton equations read

$$\mathcal{H} = e^{-\phi}, \tag{D.1}$$

$$\mathcal{F} = \frac{e^{-\phi/2}}{4(\phi' + u\phi'')} \left( a^2 e^{7\phi/2} (4u + u^2\phi') + 16\phi' \right), \tag{D.2}$$

$$\frac{\mathcal{B}'}{\mathcal{B}} = \frac{1}{24 + 10u\phi'} \left( 24\phi' - 9u\phi'^2 + 20u\phi'' \right) \tag{D.3}$$

and depend only on the dilaton<sup>1</sup>. The latter obeys a third order non linear differential equation

$$\begin{aligned} 0 = & u(5u\phi' + 12)(u\phi'' + \phi') \left( 256\phi'\phi'' - 16\phi'^3(7u\phi' + 32) \right) + \\ & \phi' \left( ua^2 e^{7\phi/2} (u\phi' + 4) + 16\phi' \right) \left( 13u^3\phi'^4 + 8u(11u^2\phi''^2 - 60\phi'' - 12u\phi''') \right) \\ & + u^2\phi'^3(13u^2\phi'' + 96) + 2u\phi'^2(-5u^3\phi''' + 53u^2\phi'' + 36) \\ & + \phi'(30u^4\phi''^2 - 64u^3\phi''' - 288 + 32u^2\phi'') \Big). \end{aligned} \tag{D.4}$$

---

<sup>1</sup>The freedom to normalize (D.3) is used to set  $\mathcal{B}_{bdry} = 1$

In the above, primes denote derivatives with respect to the holographic coordinate  $u$ . In eq. (D.4) we can get rid of the parameter  $a$  by shifting the dilaton

$$\phi \rightarrow \tilde{\phi} = \phi + \frac{4}{7} \ln a \quad (\text{D.5})$$

and because we chose to fix  $\phi_{bdry} = 0$  we find

$$a = e^{7\tilde{\phi}_{bdry}/4}. \quad (\text{D.6})$$

This only leads to an overall factor of  $a^{2/7}$  in eq. (D.2), while all the other factors of  $a$  get eliminated.

## D.2 Numerical solution

### D.2.1 Series expansion close to the horizon

We can expand the dilaton close to the horizon as

$$\tilde{\phi} = \tilde{\phi}_h + \sum_{n \geq 1} \tilde{\phi}_n (u - u_h)^n. \quad (\text{D.7})$$

Because all the functions in the bulk metric depend on  $\tilde{\phi}$  only, it is enough to study the expansion of the dilaton here. Because the ODE for the dilaton is of third order we need to specify  $\tilde{\phi}_1$  and  $\tilde{\phi}_2$  in addition to the value at the horizon.  $\tilde{\phi}_1$  can be obtained from eq. (D.2) and the requirement that  $\mathcal{F}_h$  must vanish. This gives

$$\tilde{\phi}_1 = -\frac{4u_h e^{\frac{7\tilde{\phi}_h}{2}}}{u_h^2 e^{\frac{7\tilde{\phi}_h}{2}} + 16}. \quad (\text{D.8})$$

Next, we can insert the series for  $\tilde{\phi}$  into eq. (D.4) and get as possibilities for  $\tilde{\phi}_2$

$$\tilde{\phi}_2 = \frac{2e^{\frac{7\tilde{\phi}_h}{2}}}{u_h^2 e^{\frac{7\tilde{\phi}_h}{2}} + 16} \quad \text{or} \quad \tilde{\phi}_2 = \frac{2u_h^2 e^{7\tilde{\phi}_h} \left( u_h^2 e^{\frac{7\tilde{\phi}_h}{2}} + 128 \right)}{\left( u_h^2 e^{\frac{7\tilde{\phi}_h}{2}} + 16 \right)^3}. \quad (\text{D.9})$$

However, only the second option leads to a unique solution completely fixed by the horizon data  $\tilde{\phi}_h$  and  $u_h$ , which is what we are looking for. Eventually we obtained all the coefficients up to  $O((u - u_h)^{36})$  in the dilaton series.



### D.2.2 Series expansion close to the boundary

We can now repeat the procedure in the vicinity of the boundary at  $u = 0$ . The form of the series are

$$\tilde{\phi} = \sum_{n \geq 0} \sum_{k=0}^{2n} \tilde{\phi}_{2n,k} u^{2n} (\ln u)^k \quad (\text{D.10})$$

$$\mathcal{F} = \sum_{n \geq 0} \sum_{k=0}^{2n} \mathcal{F}_{2n,k} u^{2n} (\ln u)^k \quad (\text{D.11})$$

$$\mathcal{B} = \sum_{n \geq 0} \sum_{k=0}^{2n} \mathcal{B}_{2n,k} u^{2n} (\ln u)^k \quad (\text{D.12})$$

$$\mathcal{H} = \sum_{n \geq 0} \sum_{k=0}^{2n} \mathcal{H}_{2n,k} u^{2n} (\ln u)^k, \quad (\text{D.13})$$

where the constants  $\mathcal{F}_4$  and  $\mathcal{B}_4$ , defined in section 2.2.2, correspond to  $\mathcal{F}_{4,0}$  and  $\mathcal{B}_{4,0}$ , respectively. We again concentrate on the dilaton, because all the other functions can be expressed in terms of it. For  $\tilde{\phi}$  the expansion is given by

$$\tilde{\phi}(u) = \tilde{\phi}_{bdry} - \frac{1}{4} u^2 e^{\frac{7\tilde{\phi}_{bdry}}{2}} + u^4 \left( \tilde{\phi}_{4,0} - \frac{1}{6} e^{7\tilde{\phi}_{bdry}} \ln(u) \right) \quad (\text{D.14})$$

$$+ u^6 \left( \tilde{\phi}_{6,0} + \frac{23}{432} e^{\frac{21\tilde{\phi}_{bdry}}{2}} \ln(u) \right) + O(u^8), \quad (\text{D.15})$$

with all higher terms only depending on  $\tilde{\phi}_{bdry}$ ,  $\tilde{\phi}_{4,0}$  and  $\tilde{\phi}_{6,0}$ . We computed the series up to order  $O(u^{22})$ .  $\tilde{\phi}_{4,0}$  and  $\tilde{\phi}_{6,0}$  must then be determined by matching the series to the dilaton which has been numerically integrated from the horizon sufficiently close to the boundary. We will discuss this in a moment. We conclude this section with stating the expressions for  $\mathcal{F}_{4,0}$  and  $\mathcal{B}_{4,0}$

$$\mathcal{B}_{4,0} = \frac{7\tilde{\phi}_{4,0}}{2} - \frac{121e^{7\tilde{\phi}_{bdry}}}{1152}, \quad (\text{D.16})$$

$$\mathcal{F}_{4,0} = - \frac{e^{-\frac{7\tilde{\phi}_{bdry}}{2}} \left( -576\tilde{\phi}_{4,0} e^{\frac{7\tilde{\phi}_{bdry}}{2}} + 725e^{\frac{21\tilde{\phi}_{bdry}}{2}} - 20736\tilde{\phi}_{6,0} \right)}{1728}. \quad (\text{D.17})$$

### D.2.3 Matching of solutions

The matching between the horizon data and the boundary data was done by applying the Newton-Raphson method following partly the description given in the appendix

of [158]. We start by integrating numerically from close to the horizon to near the boundary<sup>2</sup> for fixed  $u_h$  and  $\tilde{\phi}_h$  and compute  $\tilde{\phi}$ ,  $\tilde{\phi}'$  and  $\tilde{\phi}''$  at some value  $u_*$  close to the boundary. A convenient choice in most cases is  $u_* = 1/100$ , however if  $u_h$  becomes too small we have to adjust the value of  $u_*$  accordingly. Additionally, we start with a guess  $\mathbf{X} = (\tilde{\phi}_{bdry}, \tilde{\phi}_{4,0}, \tilde{\phi}_{6,0})$  and compute  $\tilde{\phi}$ ,  $\tilde{\phi}'$  and  $\tilde{\phi}''$  from the boundary series. Then we construct the 'mismatch vector'  $\mathbf{M}$ , which is given by

$$\mathbf{M} = (\tilde{\phi}, \tilde{\phi}', \tilde{\phi}'')(u_*)|_{\text{boundary data}} - (\tilde{\phi}, \tilde{\phi}', \tilde{\phi}'')(u_*)|_{\text{horizon data}} \quad (\text{D.18})$$

and obviously depends on our initial guess. For the correct choice of  $\mathbf{X}$  the mismatch vector must vanish. Therefore, we are looking for a good enough guess such that the Manhattan norm  $|\mathbf{M}| = \sum_{i=1}^3 |M_i|$  is below some threshold<sup>3</sup>. Essentially the problem is finding a root of  $\mathbf{M}$ . Next, the Jacobian matrix  $\mathbf{J}$  of partial derivatives of the mismatch vector ( $J_{ij} = \partial_j M_i$ ) is computed. Then a new guess is formed by

$$\mathbf{X}_{new} = \mathbf{X} - \mathbf{J}^{-1}\mathbf{M}. \quad (\text{D.19})$$

This procedure is iterated until  $\mathbf{X}_{new}$  converges and is sufficiently close to the true value, such that the norm of  $\mathbf{M}$  drops below the specified threshold.

For this method to work the initial guess has to be reasonably good. We found it is extremely sensitive on our initial choice of  $\tilde{\phi}_{bdry}$ , which we fix by taking the value of  $\tilde{\phi}|_{\text{horizon data}}$  as close to the boundary as possible. Since the initial values of  $\tilde{\phi}_{4,0}$  and  $\tilde{\phi}_{6,0}$  are less critical we start with setting them to zero always.

---

<sup>2</sup>We typically choose to integrate from  $u_h - 1/1000$  to  $1/1000$ . We use Mathematica's `NDSolve` with `PrecisionGoal` and `AccuracyGoal` set to 20 and `WorkingPrecision` set to 40.

<sup>3</sup>A convenient threshold was  $10^{-25}$ .

# Appendix E

## Details on the zero-coupling limit of the MT model

### E.1 $T = 0$ contribution

The  $T = 0$  contribution to the free energy density is given by

$$\begin{aligned} f(0, a) &= \Omega + \frac{1}{2} \int_k [\omega_+(k_\perp, k_z) + \omega_-(k_\perp, k_z)] \\ &= \Omega_B(\Lambda_\perp, \epsilon) + \frac{1}{4\pi} \int_{k_z} \int_0^{\Lambda_\perp} dk_\perp k_\perp \left[ \sqrt{k_\perp^2 + M_+^2(k_z)} + \sqrt{k_\perp^2 + M_-^2(k_z)} \right], \end{aligned} \quad (\text{E.1})$$

where we have introduced a UV regulator for the integration over the transverse momenta and anticipated that the zero-loop contribution (which is just  $\Omega$ ) will need to be renormalized. The integral over the transverse momentum can be carried out easily, giving

$$\begin{aligned} \int_0^{\Lambda_\perp} dk_\perp k_\perp \sqrt{k_\perp^2 + M_\pm^2(k_z)} &= \int_0^\infty dk k \left[ \sqrt{k^2 + M_\pm^2(k_z)} - k - \frac{M_\pm^2(k_z)}{2k} \right] \\ &\quad + \int_0^{\Lambda_\perp} dk \left( k^2 + \frac{1}{2} M_\pm^2(k_z) \right) + \mathcal{O}(1/\Lambda_\perp) \\ &= -\frac{1}{3} M_\pm^3(k_z) + \frac{1}{3} \Lambda_\perp^3 + \frac{1}{2} M_\pm^2(k_z) \Lambda_\perp + \mathcal{O}(1/\Lambda_\perp). \end{aligned} \quad (\text{E.2})$$

Inserting this into  $f(0, a)$  above, dropping terms that vanish as the regulators are removed, we get

$$\begin{aligned} f(0, a) &= -\frac{1}{12\pi} \int_{k_z} [M_+^3(k_z) + M_-^3(k_z)] + \frac{\Lambda_\perp}{4\pi} \int_{k_z} (2k_z^2 + a^2) + \Omega_B(\Lambda_\perp, \epsilon) \\ &= -\frac{1}{12\pi} \int_{k_z} [M_+^3(k_z) + M_-^3(k_z)] + \Omega_B(\Lambda_\perp, \epsilon). \end{aligned} \quad (\text{E.3})$$

Extracting the large- $k_z$  behavior, the first term can be written as

$$\begin{aligned} \sum_{\pm} \int_{k_z} M_{\pm}^3(k_z) &= \frac{1}{\pi} \int_0^{\infty} dk_z \left[ M_+^3(k_z) + M_-^3(k_z) - 2k_z^3 - \frac{9}{4}a^2k_z - \frac{15a^4}{64\sqrt{k_z^2 + a^2}} \right] \\ &\quad + \int_{k_z} \left[ 2k_z^2 + \frac{9}{4}a^2k_z + \frac{15a^4}{64\sqrt{k_z^2 + a^2}} \right] + \mathcal{O}(\epsilon) \\ &= \frac{c a^4}{\pi} + \frac{15a^4}{128\pi} \left( \frac{1}{\epsilon} - \ln \frac{a^2}{\bar{\Lambda}^2} \right) + \mathcal{O}(\epsilon), \end{aligned} \quad (\text{E.4})$$

where

$$\begin{aligned} c &= \int_0^{\infty} dx \left[ \left( x^2 + \frac{1}{2}(1 + \sqrt{1 + 4x^2}) \right)^{3/2} + \left( x^2 + \frac{1}{2}(1 - \sqrt{1 + 4x^2}) \right)^{3/2} \right. \\ &\quad \left. - 2x^3 - \frac{9}{4}x - \frac{15}{64\sqrt{1 + x^2}} \right] = 0.29136 \dots \end{aligned} \quad (\text{E.5})$$

The free energy density at  $T = 0$  is then

$$\begin{aligned} f(0, a) &= -\frac{c a^4}{12\pi^2} - \frac{5a^4}{512\pi^2} \left( \frac{1}{\epsilon} - \ln \frac{a^2}{\bar{\Lambda}^2} \right) + \Omega_B(\Lambda_{\perp}, \epsilon) \\ &\equiv -\frac{c a^4}{12\pi^2} + \frac{5a^4}{256\pi^2} \ln \frac{a}{\bar{\Lambda}} + \Omega(\bar{\Lambda}), \end{aligned} \quad (\text{E.6})$$

where  $\Omega(\bar{\Lambda})$  is the renormalized cosmological constant in the  $\overline{MS}$ -scheme.

## E.2 Finite $T$ contribution

The finite- $T$  contribution is given by

$$f(T, a) - f(0, a) = T \sum_{\pm} \int_k \ln(1 - e^{-\beta\omega_{\pm}}). \quad (\text{E.7})$$

The integral over the transverse momenta can be carried out immediately using standard integrals. Noting that

$$2T \frac{\partial}{\partial k_{\perp}^2} \ln(1 - e^{-\beta\omega_{\pm}}) = \frac{1}{\omega_{\pm}} \frac{1}{e^{\beta\omega_{\pm}} - 1}, \quad (\text{E.8})$$

we find

$$T \int \frac{d^2 k_{\perp}}{(2\pi)^2} \ln(1 - e^{-\beta\omega_{\pm}}) = -\frac{3T^3}{2\pi} h_4(M_{\pm}(k_z)/T, 0), \quad (\text{E.9})$$

where the function  $h_n(y, r)$  is defined by

$$h_n(y, r) = \frac{1}{\Gamma(n)} \int_0^\infty dx \frac{x^{n-1}}{\sqrt{x^2 + y^2}} \frac{1}{e^{\sqrt{x^2 + y^2} - ry} - 1}. \quad (\text{E.10})$$

Their properties are discussed in detail in [159]. In particular,

$$\frac{\partial}{\partial y} h_{n+1}(y, 0) = -\frac{y}{n} h_{n-1}(y, 0), \quad (\text{E.11})$$

$$h_2(y, 0) = -\ln(1 - e^{-y}), \quad (\text{E.12})$$

$$h_4(y, 0) = \frac{1}{3} [y \text{Li}_2(e^{-y}) + \text{Li}_3(e^{-y})]. \quad (\text{E.13})$$

We now get for the integral over the longitudinal momentum,

$$\begin{aligned} \int_{-\infty}^{\infty} \frac{dk_z}{2\pi} h_4(M_\pm/T, 0) &= \frac{1}{\pi} \int_0^\infty dk_z h_4(M_\pm/T, 0) \\ &= \frac{1}{3\pi T^2} \int_0^\infty dk_z k_z M_\pm \frac{dM_\pm}{dk_z} h_2(M_\pm/T, 0) \\ &= -\frac{T}{3\pi} \int_0^\infty dx x^2 \left(1 \pm \frac{y}{\sqrt{x^2 + y^2}}\right) \ln(1 - e^{-\sqrt{x^2 + y^2} \mp y}), \end{aligned} \quad (\text{E.14})$$

where we have denoted  $y = a/(2T)$ . The finite- $T$  contribution is thus given by the integral

$$f(T, a) - f(0, a) = \frac{T^4}{2\pi^2} \sum_{\pm} \int_0^\infty dx x^2 \left(1 \pm \frac{y}{\sqrt{x^2 + y^2}}\right) \ln(1 - e^{-\sqrt{x^2 + y^2} \mp y}). \quad (\text{E.15})$$

### E.2.1 High- and low- $T$ expansions

Even though we shall study the thermodynamic properties of this system numerically, it is instructive to calculate the analytic high- and low- $T$  approximations to the free energy as well. As derived above, the finite- $T$  contribution is given by

$$f(T, a) - f(0, a) = -\frac{4T^4}{\pi^2} [h_5(y, 1) + h_5(y, -1)] + \frac{T^4}{2\pi^2} I(y, 1), \quad (\text{E.16})$$

where

$$I(y, r) = \int_0^\infty dx \frac{yx^2}{\sqrt{x^2 + y^2}} \left[ \ln(1 - e^{-\sqrt{x^2 + y^2} - ry}) - \ln(1 - e^{-\sqrt{x^2 + y^2} + ry}) \right]. \quad (\text{E.17})$$

We immediately find that

$$I(y, 0) = 0, \quad (\text{E.18})$$

$$\frac{\partial I}{\partial r} = 2y^2 [h_3(y, r) + h_3(y, -r)] \quad (\text{E.19})$$

and thus

$$I(y, 1) = 2y^2 \int_0^1 dr [h_3(y, r) + h_3(y, -r)]. \quad (\text{E.20})$$

The high- $T$  (small- $y$ ) expansions of  $h_n(y, r) + h_n(y, -r)$  have been computed in [159], with the results

$$h_5(y, 1) + h_5(y, -1) = \frac{\pi^4}{180} + \frac{\pi^2 y^2}{48} + \frac{y^4}{64} \left( \ln \frac{y}{4\pi} + \gamma_E + \frac{7}{12} \right) + \mathcal{O}(y^6), \quad (\text{E.21})$$

$$h_3(y, r) + h_3(y, -r) = \frac{\pi^2}{6} - \frac{\pi y}{2} \sqrt{1 - r^2} - \frac{y^2}{4} \left( \ln \frac{y}{4\pi} + \gamma_E - \frac{1}{2} + r^2 \right) + \mathcal{O}(y^4) \quad (\text{E.22})$$

Putting everything together, and setting  $y = a/(2T)$  we get

$$f(T, a) - f(0, a) = -\frac{\pi^2 T^4}{45} + \frac{a^2 T^2}{48} - \frac{a^3 T}{64} - \frac{5a^4}{256\pi^2} \left( \ln \frac{a}{8\pi T} + \gamma_E - \frac{1}{60} \right) + \mathcal{O}(a^6 T^{-2}) \quad (\text{E.23})$$

for the high- $T$  expansion. On the other hand, at low temperatures (high- $y$  limit) we have

$$h_5(y, 1) + h_5(y, -1) = \frac{1}{64} \sqrt{\frac{\pi y}{2}} \left( 8\zeta(5/2)y + 15\zeta(7/2) + \mathcal{O}(1/y) \right), \quad (\text{E.24})$$

$$h_3(y, r) + h_3(y, -r) = \frac{1}{2} \sqrt{\frac{\pi y}{2}} \left[ \text{Li}_{3/2}(e^{(r-1)y}) + \text{Li}_{3/2}(e^{-(r+1)y}) \right. \\ \left. + \frac{3}{8y} (\text{Li}_{5/2}(e^{(r-1)y}) + \text{Li}_{5/2}(e^{-(r+1)y})) + \mathcal{O}(1/y^2) \right], \quad (\text{E.25})$$

$$\Rightarrow I(y, 1) = \frac{1}{8} \sqrt{\frac{\pi y}{2}} \left( 8\zeta(5/2)y + 3\zeta(7/2) + \mathcal{O}(1/y) \right). \quad (\text{E.26})$$

Combining the results gives us

$$f(T, a) - f(0, a) = -\frac{3\zeta(7/2)}{8\pi^{3/2}} a^{1/2} T^{7/2} + \mathcal{O}(a^{-1/2}) \quad (\text{E.27})$$

in the low- $T$  limit.

# Acknowledgments

Eventually it is time for me to say a heartfelt “thank you” to the many people who contributed to this thesis in one way or another.

First of all I want to mention my supervisor Toni Rebhan, who is not only an excellent mentor but also has become a good friend. Ever since I first entered his office in 2008 looking for a student’s project, I have profited tremendously from his knowledge and have been impressed by his commitment to science. In the following four and a half years he encouraged me to follow my own ideas but was always there to discuss any problems that would surely appear sooner or later. Working with him was a truly inspiring experience. But aside from his scientific guidance I wish to thank him for his support in every respect during difficult times.

Next, I want to express my gratitude to Karl Landsteiner, who not only welcomed me to a short stay in Madrid in 2010 and readily discussed physics with me, but also supported me in many ways later on. It is a pleasure and honor to have him as my external examiner.

I also thank Jean-Paul Blaizot for his trust in my skills when he offered me a post doc position at Saclay and his hospitality during a short visit at the IPhT.

In the past years I had the luck to collaborate with Antti Gynther, Aleksi Vuorinen and Stefan Stricker on some projects. It was a truly pleasure to work with them and learn from them. Especially the part about the zero coupling limit of the MT model presented in this thesis would not exist without the expertise of Antti. Stefan and Aleksi offered me the possibility to join their collaboration and investigate the coupling dependence of thermalization processes via the holographic duality, which is, however, not covered in this thesis. Stefan also helped me a lot by proofreading an early draft of my thesis and I owe him a big thank you for this as well.

When I got up in the morning I usually enjoyed going to work and this is due to my dear colleagues and friends at the Institute of Theoretical Physics. Especially I want to mention Max Attems, Stefan Stricker, David Burke, Christoph Mayrhofer and Maria Schimpf with whom I shared an office. I enjoyed the many discussions whether they were about physics or not. I want to express my gratitude to Max who not only helped me with any computer related problem, but also took care of me when I started to work at the institute in 2008. Furthermore, I thank the additional

members of the “Strong Group” Andreas Ipp, Andreas Schmitt, Denis Parganlija, Florian Preis, Stephan Stetina and Frederic Brünner for all the fun at the institute and at conferences, where we sometimes even went skiing or hiking. I am also grateful for all the support from the former and present administrative staff at the institute Elfriede Mössmer, Roswitha Uden, Sylvia Riedler and Heike Höller.

I surely would not have been able to write this thesis without the encouragement from my family and friends. My parents Gerti and Hans always regarded it as to go without saying that they would support me in every respect of my life and made my studies possible in a first place. I know that this can not be taken for granted and I want to thank them for being there whenever I need them. I also wish to thank my deceased brother Manuel, who was always concerned that I would work too much, for his numerous attempts to convince me that there is a life besides physics too. I could without exception always rely on him when something bothered me. I thank Natalie and Darleen, my nieces, for the many happy moments and wish them only the best for their future.

I consider myself to be a really lucky person, because I even found a kind of second family and I want to thank Reinhard, Anni, Josef, Tanja, Christoph and Pizi for their support and friendship. Furthermore I wish to thank all my friends I do not list by names here for being there for me and at the same time apologize that I am in contact so rarely.

Finally, I want to express my heartfelt gratitude to Theresa, the love of my life, who has the ability to make me smile when I am desperate and who stands by me no matter what happens. And especially I thank her for saying “yes”.



# Bibliography

- [1] G. Veneziano, “Construction of a crossing - symmetric, Regge behaved amplitude for linearly rising trajectories,” *Nuovo Cim.* **A57** (1968) 190–197.
- [2] M. Gell-Mann, “A Schematic Model of Baryons and Mesons,” *Phys.Lett.* **8** (1964) 214–215.
- [3] D. Gross and F. Wilczek, “Ultraviolet Behavior of Nonabelian Gauge Theories,” *Phys.Rev.Lett.* **30** (1973) 1343–1346.
- [4] H. D. Politzer, “Reliable Perturbative Results for Strong Interactions?,” *Phys.Rev.Lett.* **30** (1973) 1346–1349.
- [5] **Wuppertal-Budapest Collaboration** Collaboration, S. Borsanyi *et al.*, “Is there still any  $T_c$  mystery in lattice QCD? Results with physical masses in the continuum limit III,” *JHEP* **1009** (2010) 073, [arXiv:1005.3508 \[hep-lat\]](#).
- [6] A. Bazavov, T. Bhattacharya, M. Cheng, C. DeTar, H. Ding, *et al.*, “The chiral and deconfinement aspects of the QCD transition,” *Phys.Rev.* **D85** (2012) 054503, [arXiv:1111.1710 \[hep-lat\]](#).
- [7] R. Stock, “Relativistic nucleus-nucleus collisions: From the BEVALAC to RHIC,” *J.Phys.G* **G30** (2004) S633–S648, [arXiv:nucl-ex/0405007 \[nucl-ex\]](#).
- [8] M. L. Miller, K. Reygers, S. J. Sanders, and P. Steinberg, “Glauber modeling in high energy nuclear collisions,” *Ann.Rev.Nucl.Part.Sci.* **57** (2007) 205–243, [arXiv:nucl-ex/0701025 \[nucl-ex\]](#).
- [9] J. Casalderrey-Solana, H. Liu, D. Mateos, K. Rajagopal, and U. A. Wiedemann, “Gauge/String Duality, Hot QCD and Heavy Ion Collisions,” [arXiv:1101.0618 \[hep-th\]](#).
- [10] A. Adams, L. D. Carr, T. Schäfer, P. Steinberg, and J. E. Thomas, “Strongly Correlated Quantum Fluids: Ultracold Quantum Gases, Quantum

- Chromodynamic Plasmas, and Holographic Duality,” [arXiv:1205.5180](#) [hep-th].
- [11] P. Romatschke and U. Romatschke, “Viscosity Information from Relativistic Nuclear Collisions: How Perfect is the Fluid Observed at RHIC?,” *Phys.Rev.Lett.* **99** (2007) 172301, [arXiv:0706.1522](#) [nucl-th].
  - [12] **ALICE Collaboration** Collaboration, K. Aamodt *et al.*, “Elliptic flow of charged particles in Pb-Pb collisions at 2.76 TeV,” *Phys.Rev.Lett.* **105** (2010) 252302, [arXiv:1011.3914](#) [nucl-ex].
  - [13] S. C. Huot, S. Jeon, and G. D. Moore, “Shear viscosity in weakly coupled  $N = 4$  super Yang-Mills theory compared to QCD,” *Phys.Rev.Lett.* **98** (2007) 172303, [arXiv:hep-ph/0608062](#) [hep-ph].
  - [14] **STAR Collaboration** Collaboration, J. Adams *et al.*, “Distributions of charged hadrons associated with high transverse momentum particles in pp and Au + Au collisions at  $\sqrt{s_{NN}} = 200$  GeV,” *Phys.Rev.Lett.* **95** (2005) 152301, [arXiv:nucl-ex/0501016](#) [nucl-ex].
  - [15] **CMS Collaboration** Collaboration, S. Chatrchyan *et al.*, “Observation and studies of jet quenching in PbPb collisions at nucleon-nucleon center-of-mass energy = 2.76 TeV,” *Phys.Rev.* **C84** (2011) 024906, [arXiv:1102.1957](#) [nucl-ex].
  - [16] **PHENIX Collaboration** Collaboration, K. Adcox *et al.*, “Centrality dependence of  $\pi^{+/-}$ ,  $K^{+/-}$ ,  $p$  and  $\bar{p}$  production from  $\sqrt{s_{NN}} = 130$  GeV Au+Au collisions at RHIC,” *Phys.Rev.Lett.* **88** (2002) 242301, [arXiv:nucl-ex/0112006](#) [nucl-ex].
  - [17] **ALICE Collaboration** Collaboration, K. Aamodt *et al.*, “Suppression of Charged Particle Production at Large Transverse Momentum in Central Pb–Pb Collisions at  $\sqrt{s_{NN}} = 2.76$  TeV,” *Phys.Lett.* **B696** (2011) 30–39, [arXiv:1012.1004](#) [nucl-ex].
  - [18] **PHENIX Collaboration** Collaboration, T. Isobe, “Systematic study of high- $p(T)$  direct photon production with the PHENIX experiment at RHIC,” *J.Phys.G* **G34** (2007) S1015–1018, [arXiv:nucl-ex/0701040](#) [nucl-ex].
  - [19] **CMS Collaboration** Collaboration, S. Chatrchyan *et al.*, “Indications of suppression of excited  $\Upsilon$  states in PbPb collisions at  $\sqrt{s_{NN}} = 2.76$  TeV,” *Phys.Rev.Lett.* **107** (2011) 052302, [arXiv:1105.4894](#) [nucl-ex].

- [20] J. M. Maldacena, “The Large N limit of superconformal field theories and supergravity,” *Adv.Theor.Math.Phys.* **2** (1998) 231–252, [arXiv:hep-th/9711200](#) [hep-th].
- [21] S. S. Gubser and A. Karch, “From gauge-string duality to strong interactions: A Pedestrian’s Guide,” *Ann.Rev.Nucl.Part.Sci.* **59** (2009) 145–168, [arXiv:0901.0935](#) [hep-th].
- [22] J. McGreevy, “Holographic duality with a view toward many-body physics,” *Adv.High Energy Phys.* **2010** (2010) 723105, [arXiv:0909.0518](#) [hep-th].
- [23] J. Polchinski, “Introduction to Gauge/Gravity Duality,” [arXiv:1010.6134](#) [hep-th].
- [24] G. Policastro, D. Son, and A. Starinets, “The shear viscosity of strongly coupled N=4 supersymmetric Yang-Mills plasma,” *Phys.Rev.Lett.* **87** (2001) 081601, [arXiv:hep-th/0104066](#) [hep-th].
- [25] W. Florkowski and R. Ryblewski, “Highly-anisotropic and strongly-dissipative hydrodynamics for early stages of relativistic heavy-ion collisions,” *Phys.Rev.* **C83** (2011) 034907, [arXiv:1007.0130](#) [nucl-th].
- [26] M. Martinez and M. Strickland, “Matching pre-equilibrium dynamics and viscous hydrodynamics,” *Phys.Rev.* **C81** (2010) 024906, [arXiv:0909.0264](#) [hep-ph].
- [27] M. Martinez and M. Strickland, “Non-boost-invariant anisotropic dynamics,” *Nucl.Phys.* **A856** (2011) 68–87, [arXiv:1011.3056](#) [nucl-th].
- [28] M. Martinez and M. Strickland, “Dissipative Dynamics of Highly Anisotropic Systems,” *Nucl.Phys.* **A848** (2010) 183–197, [arXiv:1007.0889](#) [nucl-th].
- [29] S. Mrowczynski, “Stream instabilities of the quark-gluon plasma,” *Phys.Lett.* **B214** (1988) 587.
- [30] P. Romatschke and M. Strickland, “Collective modes of an anisotropic quark gluon plasma,” *Phys.Rev.* **D68** (2003) 036004, [arXiv:hep-ph/0304092](#) [hep-ph].
- [31] P. B. Arnold, J. Lenaghan, and G. D. Moore, “QCD plasma instabilities and bottom up thermalization,” *JHEP* **0308** (2003) 002, [arXiv:hep-ph/0307325](#) [hep-ph].

- [32] P. B. Arnold, G. D. Moore, and L. G. Yaffe, “The Fate of non-Abelian plasma instabilities in 3+1 dimensions,” *Phys.Rev.* **D72** (2005) 054003, [arXiv:hep-ph/0505212](#) [[hep-ph](#)].
- [33] A. Rebhan, P. Romatschke, and M. Strickland, “Hard-loop dynamics of non-Abelian plasma instabilities,” *Phys.Rev.Lett.* **94** (2005) 102303, [arXiv:hep-ph/0412016](#) [[hep-ph](#)].
- [34] A. Rebhan, M. Strickland, and M. Attems, “Instabilities of an anisotropically expanding non-Abelian plasma: 1D+3V discretized hard-loop simulations,” *Phys.Rev.* **D78** (2008) 045023, [arXiv:0802.1714](#) [[hep-ph](#)].
- [35] A. Rebhan and D. Steineder, “Collective modes and instabilities in anisotropically expanding ultrarelativistic plasmas,” *Phys.Rev.* **D81** (2010) 085044, [arXiv:0912.5383](#) [[hep-ph](#)].
- [36] M. Attems, A. Rebhan, and M. Strickland, “Instabilities of an anisotropically expanding non-Abelian plasma: 3D+3V discretized hard-loop simulations,” [arXiv:1207.5795](#) [[hep-ph](#)].
- [37] D. Grumiller and P. Romatschke, “On the collision of two shock waves in  $\text{AdS}_5$ ,” *JHEP* **0808** (2008) 027, [arXiv:0803.3226](#) [[hep-th](#)].
- [38] P. M. Chesler and L. G. Yaffe, “Horizon formation and far-from-equilibrium isotropization in supersymmetric Yang-Mills plasma,” *Phys.Rev.Lett.* **102** (2009) 211601, [arXiv:0812.2053](#) [[hep-th](#)].
- [39] P. M. Chesler and L. G. Yaffe, “Holography and colliding gravitational shock waves in asymptotically  $\text{AdS}_5$  spacetime,” *Phys.Rev.Lett.* **106** (2011) 021601, [arXiv:1011.3562](#) [[hep-th](#)].
- [40] M. P. Heller, R. A. Janik, and P. Witaszczyk, “The characteristics of thermalization of boost-invariant plasma from holography,” *Phys.Rev.Lett.* **108** (2012) 201602, [arXiv:1103.3452](#) [[hep-th](#)].
- [41] M. P. Heller, R. A. Janik, and P. Witaszczyk, “A numerical relativity approach to the initial value problem in asymptotically Anti-de Sitter spacetime for plasma thermalization - an ADM formulation,” *Phys.Rev.* **D85** (2012) 126002, [arXiv:1203.0755](#) [[hep-th](#)].
- [42] M. P. Heller, D. Mateos, W. van der Schee, and D. Trancanelli, “Strong Coupling Isotropization of Non-Abelian Plasmas Simplified,” *Phys.Rev.Lett.* **108** (2012) 191601, [arXiv:1202.0981](#) [[hep-th](#)].

- [43] D. Vollhardt and P. Wölfle, *The Phases of Superfluid Helium-3*. Taylor and Francis, London, 1990.
- [44] S. S. Gubser and S. S. Pufu, “The Gravity dual of a p-wave superconductor,” *JHEP* **0811** (2008) 033, [arXiv:0805.2960 \[hep-th\]](#).
- [45] M. Ammon, J. Erdmenger, V. Grass, P. Kerner, and A. O’Bannon, “On Holographic p-wave Superfluids with Back-reaction,” *Phys.Lett.* **B686** (2010) 192–198, [arXiv:0912.3515 \[hep-th\]](#).
- [46] S. Chandrasekhar, *Liquid Crystals*. Cambridge University Press, Cambridge, second ed., 1993.
- [47] A. Gynther, A. Rebhan, and D. Steineder, “Thermodynamics and phase diagram of anisotropic Chern-Simons deformed gauge theories,” *JHEP* **1210** (2012) 012, [arXiv:1207.6283 \[hep-th\]](#).
- [48] A. Rebhan and D. Steineder, “Electromagnetic signatures of a strongly coupled anisotropic plasma,” *JHEP* **1108** (2011) 153, [arXiv:1106.3539 \[hep-th\]](#).
- [49] A. Rebhan and D. Steineder, “Violation of the Holographic Viscosity Bound in a Strongly Coupled Anisotropic Plasma,” *Phys.Rev.Lett.* **108** (2012) 021601, [arXiv:1110.6825 \[hep-th\]](#).
- [50] A. Rebhan and D. Steineder, “Probing Two Holographic Models of Strongly Coupled Anisotropic Plasma,” *JHEP* **1208** (2012) 020, [arXiv:1205.4684 \[hep-th\]](#).
- [51] R. C. Myers, “Stress tensors and Casimir energies in the AdS/CFT correspondence,” *Phys.Rev.* **D60** (1999) 046002, [arXiv:hep-th/9903203 \[hep-th\]](#).
- [52] V. Balasubramanian, J. de Boer, and D. Minic, “Mass, entropy and holography in asymptotically de Sitter spaces,” *Phys.Rev.* **D65** (2002) 123508, [arXiv:hep-th/0110108 \[hep-th\]](#).
- [53] S. de Haro, S. N. Solodukhin, and K. Skenderis, “Holographic reconstruction of space-time and renormalization in the AdS/CFT correspondence,” *Commun.Math.Phys.* **217** (2001) 595–622, [arXiv:hep-th/0002230 \[hep-th\]](#).
- [54] G. Beuf, M. P. Heller, R. A. Janik, and R. Peschanski, “Boost-invariant early time dynamics from AdS/CFT,” *JHEP* **0910** (2009) 043, [arXiv:0906.4423 \[hep-th\]](#).

- [55] R. A. Janik and R. B. Peschanski, “Asymptotic perfect fluid dynamics as a consequence of AdS/CFT,” *Phys.Rev.* **D73** (2006) 045013, [arXiv:hep-th/0512162](#) [hep-th].
- [56] R. A. Janik and P. Witaszczyk, “Towards the description of anisotropic plasma at strong coupling,” *JHEP* **0809** (2008) 026, [arXiv:0806.2141](#) [hep-th].
- [57] I. Gahramanov, T. Kalaydzhyan, and I. Kirsch, “Anisotropic hydrodynamics, holography and the chiral magnetic effect,” *Phys.Rev.* **D85** (2012) 126013, [arXiv:1203.4259](#) [hep-th].
- [58] D. Mateos and D. Trancanelli, “The anisotropic N=4 super Yang-Mills plasma and its instabilities,” *Phys.Rev.Lett.* **107** (2011) 101601, [arXiv:1105.3472](#) [hep-th].
- [59] D. Mateos and D. Trancanelli, “Thermodynamics and Instabilities of a Strongly Coupled Anisotropic Plasma,” *JHEP* **1107** (2011) 054, [arXiv:1106.1637](#) [hep-th].
- [60] T. Azeyanagi, W. Li, and T. Takayanagi, “On String Theory Duals of Lifshitz-like Fixed Points,” *JHEP* **0906** (2009) 084, [arXiv:0905.0688](#) [hep-th].
- [61] M. Fujita, W. Li, S. Ryu, and T. Takayanagi, “Fractional Quantum Hall Effect via Holography: Chern-Simons, Edge States, and Hierarchy,” *JHEP* **0906** (2009) 066, [arXiv:0901.0924](#) [hep-th].
- [62] J. Estes, A. O’Bannon, E. Tsatis, and T. Wrase, “Holographic Wilson Loops, Dielectric Interfaces, and Topological Insulators,” [arXiv:1210.0534](#) [hep-th].
- [63] I. Papadimitriou, “Holographic renormalization of general dilaton-axion gravity,” *JHEP* **1108** (2011) 119, [arXiv:1106.4826](#) [hep-th].
- [64] S. M. Carroll, G. B. Field, and R. Jackiw, “Limits on a Lorentz and Parity Violating Modification of Electrodynamics,” *Phys.Rev.* **D41** (1990) 1231.
- [65] J. Ralston, “Gauge theory in the adiabatic approximation,” *Phys.Rev.* **D51** (1995) 2018–2021.
- [66] C. Adam and F. R. Klinkhamer, “Causality and CPT violation from an Abelian Chern-Simons like term,” *Nucl.Phys.* **B607** (2001) 247–267, [arXiv:hep-ph/0101087](#) [hep-ph].

- [67] P. Aurenche, F. Gelis, R. Kobes, and H. Zaraket, “Bremsstrahlung and photon production in thermal QCD,” *Phys.Rev.* **D58** (1998) 085003, [arXiv:hep-ph/9804224](#) [hep-ph].
- [68] P. B. Arnold, G. D. Moore, and L. G. Yaffe, “Photon emission from quark gluon plasma: Complete leading order results,” *JHEP* **0112** (2001) 009, [arXiv:hep-ph/0111107](#) [hep-ph].
- [69] P. B. Arnold, G. D. Moore, and L. G. Yaffe, “Photon and gluon emission in relativistic plasmas,” *JHEP* **0206** (2002) 030, [arXiv:hep-ph/0204343](#) [hep-ph].
- [70] J.-P. Blaizot and F. Gelis, “Photon and dilepton production in the quark-gluon plasma: Perturbation theory vs lattice QCD,” *Eur.Phys.J.* **C43** (2005) 375–380, [arXiv:hep-ph/0504144](#) [hep-ph].
- [71] S. Caron-Huot, P. Kovtun, G. D. Moore, A. Starinets, and L. G. Yaffe, “Photon and dilepton production in supersymmetric Yang-Mills plasma,” *JHEP* **0612** (2006) 015, [arXiv:hep-th/0607237](#) [hep-th].
- [72] A. Parnachev and D. A. Sahakyan, “Photoemission with Chemical Potential from QCD Gravity Dual,” *Nucl.Phys.* **B768** (2007) 177–192, [arXiv:hep-th/0610247](#) [hep-th].
- [73] D. Mateos and L. Patino, “Bright branes for strongly coupled plasmas,” *JHEP* **0711** (2007) 025, [arXiv:0709.2168](#) [hep-th].
- [74] A. Nata Atmaja and K. Schalm, “Photon and Dilepton Production in Soft Wall AdS/QCD,” *JHEP* **1008** (2010) 124, [arXiv:0802.1460](#) [hep-th].
- [75] R. Baier, S. A. Stricker, O. Taanila, and A. Vuorinen, “Holographic dilepton production in a thermalizing plasma,” *JHEP* **1207** (2012) 094, [arXiv:1205.2998](#) [hep-ph].
- [76] R. Baier, S. A. Stricker, O. Taanila, and A. Vuorinen, “Production of Prompt Photons: Holographic Duality and Thermalization,” [arXiv:1207.1116](#) [hep-ph].
- [77] D. Steineder, S. A. Stricker, and A. Vuorinen, “Thermalization at intermediate coupling,” [arXiv:1209.0291](#) [hep-ph].
- [78] B. Schenke and M. Strickland, “Photon production from an anisotropic quark-gluon plasma,” *Phys.Rev.* **D76** (2007) 025023, [arXiv:hep-ph/0611332](#) [hep-ph].

- [79] A. Ipp, A. Di Piazza, J. Evers, and C. H. Keitel, “Photon polarization as a probe for quark-gluon plasma dynamics,” *Phys.Lett.* **B666** (2008) 315–319, [arXiv:0710.5700 \[hep-ph\]](#).
- [80] A. Ipp, C. H. Keitel, and J. Evers, “Yoctosecond photon pulses from quark-gluon plasmas,” *Phys.Rev.Lett.* **103** (2009) 152301, [arXiv:0904.4503 \[hep-ph\]](#).
- [81] M. Martinez and M. Strickland, “Measuring QGP thermalization time with dileptons,” *Phys.Rev.Lett.* **100** (2008) 102301, [arXiv:0709.3576 \[hep-ph\]](#).
- [82] M. Martinez and M. Strickland, “Pre-equilibrium dilepton production from an anisotropic quark-gluon plasma,” *Phys.Rev.* **C78** (2008) 034917, [arXiv:0805.4552 \[hep-ph\]](#).
- [83] M. Martinez and M. Strickland, “Suppression of forward dilepton production from an anisotropic quark-gluon plasma,” *Eur.Phys.J.* **C61** (2009) 905–913, [arXiv:0808.3969 \[hep-ph\]](#).
- [84] L. Bhattacharya and P. Roy, “Measuring isotropization time of Quark-Gluon-Plasma from direct photon at RHIC,” *Phys.Rev.* **C79** (2009) 054910, [arXiv:0812.1478 \[hep-ph\]](#).
- [85] L. Bhattacharya and P. Roy, “Rapidity distribution of photons from an anisotropic Quark-Gluon-Plasma,” *Phys.Rev.* **C81** (2010) 054904, [arXiv:0907.3607 \[hep-ph\]](#).
- [86] D. T. Son and A. O. Starinets, “Minkowski space correlators in AdS/CFT correspondence: Recipe and applications,” *JHEP* **0209** (2002) 042, [arXiv:hep-th/0205051 \[hep-th\]](#).
- [87] K. Skenderis and B. C. van Rees, “Real-time gauge/gravity duality,” *Phys.Rev.Lett.* **101** (2008) 081601, [arXiv:0805.0150 \[hep-th\]](#).
- [88] K. Skenderis and B. C. van Rees, “Real-time gauge/gravity duality: prescription, renormalization and examples,” *JHEP* **0905** (2009) 085, [arXiv:0812.2909 \[hep-th\]](#).
- [89] S. Caron-Huot, P. M. Chesler, and D. Teaney, “Fluctuation, dissipation, and thermalization in non-equilibrium AdS<sub>5</sub> black hole geometries,” *Phys.Rev.* **D84** (2011) 026012, [arXiv:1102.1073 \[hep-th\]](#).
- [90] E. Thorne, Kip S., E. Price, R.H., and E. Macdonald, D.A., “Black holes: The membrane paradigm,”.



- 
- [91] P. Kovtun, D. T. Son, and A. O. Starinets, “Holography and hydrodynamics: Diffusion on stretched horizons,” *JHEP* **0310** (2003) 064, [arXiv:hep-th/0309213](#) [hep-th].
  - [92] A. O. Starinets, “Quasinormal spectrum and the black hole membrane paradigm,” *Phys.Lett.* **B670** (2009) 442–445, [arXiv:0806.3797](#) [hep-th].
  - [93] M. Fujita, “Non-equilibrium thermodynamics near the horizon and holography,” *JHEP* **0810** (2008) 031, [arXiv:0712.2289](#) [hep-th].
  - [94] N. Iqbal and H. Liu, “Universality of the hydrodynamic limit in AdS/CFT and the membrane paradigm,” *Phys.Rev.* **D79** (2009) 025023, [arXiv:0809.3808](#) [hep-th].
  - [95] P. Kovtun, D. Son, and A. Starinets, “Viscosity in strongly interacting quantum field theories from black hole physics,” *Phys.Rev.Lett.* **94** (2005) 111601, [arXiv:hep-th/0405231](#) [hep-th].
  - [96] A. Buchel, “N=2\* hydrodynamics,” *Nucl.Phys.* **B708** (2005) 451–466, [arXiv:hep-th/0406200](#) [hep-th].
  - [97] J. Mas, “Shear viscosity from R-charged AdS black holes,” *JHEP* **0603** (2006) 016, [arXiv:hep-th/0601144](#) [hep-th].
  - [98] D. T. Son and A. O. Starinets, “Hydrodynamics of R-charged black holes,” *JHEP* **0603** (2006) 052, [arXiv:hep-th/0601157](#) [hep-th].
  - [99] K. Maeda, M. Natsuume, and T. Okamura, “Viscosity of gauge theory plasma with a chemical potential from AdS/CFT,” *Phys.Rev.* **D73** (2006) 066013, [arXiv:hep-th/0602010](#) [hep-th].
  - [100] A. Buchel, J. T. Liu, and A. O. Starinets, “Coupling constant dependence of the shear viscosity in N=4 supersymmetric Yang-Mills theory,” *Nucl.Phys.* **B707** (2005) 56–68, [arXiv:hep-th/0406264](#) [hep-th].
  - [101] M. Brigante, H. Liu, R. C. Myers, S. Shenker, and S. Yaida, “Viscosity Bound Violation in Higher Derivative Gravity,” *Phys.Rev.* **D77** (2008) 126006, [arXiv:0712.0805](#) [hep-th].
  - [102] M. Brigante, H. Liu, R. C. Myers, S. Shenker, and S. Yaida, “The Viscosity Bound and Causality Violation,” *Phys.Rev.Lett.* **100** (2008) 191601, [arXiv:0802.3318](#) [hep-th].

- [103] Y. Kats and P. Petrov, “Effect of curvature squared corrections in AdS on the viscosity of the dual gauge theory,” *JHEP* **0901** (2009) 044, [arXiv:0712.0743 \[hep-th\]](#).
- [104] K. Landsteiner and J. Mas, “The shear viscosity of the non-commutative plasma,” *JHEP* **0707** (2007) 088, [arXiv:0706.0411 \[hep-th\]](#).
- [105] J. Erdmenger, P. Kerner, and H. Zeller, “Non-universal shear viscosity from Einstein gravity,” *Phys.Lett.* **B699** (2011) 301–304, [arXiv:1011.5912 \[hep-th\]](#).
- [106] P. Basu and J.-H. Oh, “Analytic Approaches to An-Isotropic Holographic Superfluids,” *JHEP* **1207** (2012) 106, [arXiv:1109.4592 \[hep-th\]](#).
- [107] J. Erdmenger, P. Kerner, and H. Zeller, “Transport in Anisotropic Superfluids: A Holographic Description,” *JHEP* **1201** (2012) 059, [arXiv:1110.0007 \[hep-th\]](#).
- [108] L. D. Landau and E. M. Lifschitz, *Course of Theoretical Physics Vol. 7: Theory of Elasticity*. Butterworth-Heinemann, Oxford, third ed., 1999.
- [109] P. K. Kovtun and A. O. Starinets, “Quasinormal modes and holography,” *Phys.Rev.* **D72** (2005) 086009, [arXiv:hep-th/0506184 \[hep-th\]](#).
- [110] G. Policastro, D. T. Son, and A. O. Starinets, “From AdS/CFT correspondence to hydrodynamics,” *JHEP* **0209** (2002) 043, [arXiv:hep-th/0205052 \[hep-th\]](#).
- [111] K. A. Mamo, “Holographic RG flow of the shear viscosity to entropy density ratio in strongly coupled anisotropic plasma,” *JHEP* **1210** (2012) 070, [arXiv:1205.1797 \[hep-th\]](#).
- [112] P. Romatschke, “Momentum broadening in an anisotropic plasma,” *Phys.Rev.* **C75** (2007) 014901, [arXiv:hep-ph/0607327 \[hep-ph\]](#).
- [113] R. Baier and Y. Mehtar-Tani, “Jet quenching and broadening: The transport coefficient  $\hat{q}$  in an anisotropic plasma,” *Phys.Rev.* **C78** (2008) 064906, [arXiv:0806.0954 \[hep-ph\]](#).
- [114] A. Dumitru, Y. Guo, and M. Strickland, “The heavy-quark potential in an anisotropic (viscous) plasma,” *Phys.Lett.* **B662** (2008) 37–42, [arXiv:0711.4722 \[hep-ph\]](#).
- [115] O. Philipsen and M. Tassler, “On quarkonium in an anisotropic quark gluon plasma,” [arXiv:0908.1746 \[hep-ph\]](#).

- 
- [116] Y. Burnier, M. Laine, and M. Vepsalainen, “Quarkonium dissociation in the presence of a small momentum space anisotropy,” *Phys.Lett.* **B678** (2009) 86–89, [arXiv:0903.3467 \[hep-ph\]](#).
- [117] D. Giataganas, “Probing strongly coupled anisotropic plasma,” *JHEP* **1207** (2012) 031, [arXiv:1202.4436 \[hep-th\]](#).
- [118] M. Chernicoff, D. Fernandez, D. Mateos, and D. Trancanelli, “Drag force in a strongly coupled anisotropic plasma,” *JHEP* **1208** (2012) 100, [arXiv:1202.3696 \[hep-th\]](#).
- [119] K. B. Fadafan and H. Soltanpanahi, “Energy loss in a strongly coupled anisotropic plasma,” *JHEP* **1210** (2012) 085, [arXiv:1206.2271 \[hep-th\]](#).
- [120] B. Muller and D.-L. Yan, “Light Probes in a Strongly Coupled Anisotropic Plasma,” [arXiv:1210.2095 \[hep-th\]](#).
- [121] J. M. Maldacena, “Wilson loops in large N field theories,” *Phys.Rev.Lett.* **80** (1998) 4859–4862, [arXiv:hep-th/9803002 \[hep-th\]](#).
- [122] S.-J. Rey, S. Theisen, and J.-T. Yee, “Wilson-Polyakov loop at finite temperature in large N gauge theory and anti-de Sitter supergravity,” *Nucl.Phys.* **B527** (1998) 171–186, [arXiv:hep-th/9803135 \[hep-th\]](#).
- [123] A. Brandhuber, N. Itzhaki, J. Sonnenschein, and S. Yankielowicz, “Wilson loops in the large N limit at finite temperature,” *Phys.Lett.* **B434** (1998) 36–40, [arXiv:hep-th/9803137 \[hep-th\]](#).
- [124] M. Chernicoff, D. Fernandez, D. Mateos, and D. Trancanelli, “Quarkonium dissociation by anisotropy,” [arXiv:1208.2672 \[hep-th\]](#).
- [125] M. Laine, O. Philipsen, P. Romatschke, and M. Tassler, “Real-time static potential in hot QCD,” *JHEP* **0703** (2007) 054, [arXiv:hep-ph/0611300 \[hep-ph\]](#).
- [126] M. Margotta, K. McCarty, C. McGahan, M. Strickland, and D. Yager-Elorriaga, “Quarkonium states in a complex-valued potential,” *Phys.Rev.* **D83** (2011) 105019, [arXiv:1101.4651 \[hep-ph\]](#).
- [127] J.-P. Blaizot, A. Ipp, and A. Rebhan, “Study of the gluon propagator in the large- $N(f)$  limit at finite temperature and chemical potential for weak and strong couplings,” *Annals Phys.* **321** (2006) 2128–2155, [arXiv:hep-ph/0508317 \[hep-ph\]](#).

- 
- [128] M. Cherneroff, D. Fernandez, D. Mateos, and D. Trancanelli, “Jet quenching in a strongly coupled anisotropic plasma,” *JHEP* **1208** (2012) 041, [arXiv:1203.0561 \[hep-th\]](#).
- [129] H. Liu, K. Rajagopal, and U. A. Wiedemann, “Calculating the jet quenching parameter from AdS/CFT,” *Phys.Rev.Lett.* **97** (2006) 182301, [arXiv:hep-ph/0605178 \[hep-ph\]](#).
- [130] H. Liu, K. Rajagopal, and U. A. Wiedemann, “Wilson loops in heavy ion collisions and their calculation in AdS/CFT,” *JHEP* **0703** (2007) 066, [arXiv:hep-ph/0612168 \[hep-ph\]](#).
- [131] M. Carrington and A. Rebhan, “On the imaginary part of the next-to-leading-order static gluon self-energy in an anisotropic plasma,” *Phys.Rev.* **80** (2009) 065035, [arXiv:0906.5220 \[hep-ph\]](#).
- [132] A. Dumitru, Y. Nara, B. Schenke, and M. Strickland, “Jet broadening in unstable non-Abelian plasmas,” *Phys.Rev.* **C78** (2008) 024909, [arXiv:0710.1223 \[hep-ph\]](#).
- [133] A. Majumder, B. Muller, and S. Mrowczynski, “Momentum Broadening of a Fast Parton in a Perturbative Quark-Gluon Plasma,” *Phys.Rev.* **D80** (2009) 125020, [arXiv:0903.3683 \[hep-ph\]](#).
- [134] A. Ipp. Private communication.
- [135] S. Lin and E. Shuryak, “Toward the AdS/CFT Gravity Dual for High Energy Collisions. 3. Gravitationally Collapsing Shell and Quasiequilibrium,” *Phys.Rev.* **D78** (2008) 125018, [arXiv:0808.0910 \[hep-th\]](#).
- [136] J. Putschke, “Intra-jet correlations of high- $p(t)$  hadrons from STAR,” *J.Phys.G* **G34** (2007) S679–684, [arXiv:nucl-ex/0701074 \[NUCL-EX\]](#).
- [137] J. Polchinski and E. Silverstein, “Large-density field theory, viscosity, and ‘ $2k_F$ ’ singularities from string duals,” *Class.Quant.Grav.* **29** (2012) 194008, [arXiv:1203.1015 \[hep-th\]](#).
- [138] B. Schenke. Private communication.
- [139] B. Schenke, S. Jeon, and C. Gale, “(3+1)D hydrodynamic simulation of relativistic heavy-ion collisions,” *Phys.Rev.* **C82** (2010) 014903, [arXiv:1004.1408 \[hep-ph\]](#).
- [140] U. W. Heinz, “Early collective expansion: Relativistic hydrodynamics and the transport properties of QCD matter,” [arXiv:0901.4355 \[nucl-th\]](#).

- 
- [141] P. Romatschke, “New Developments in Relativistic Viscous Hydrodynamics,” *Int.J.Mod.Phys.* **E19** (2010) 1–53, [arXiv:0902.3663 \[hep-ph\]](#).
- [142] D. Teaney, “Lecture notes on shear viscosity in heavy ion collisions,” *Prog.Part.Nucl.Phys.* **62** (2009) 451–461.
- [143] A. Muronga, “Second-order dissipative fluid dynamics for ultrarelativistic nuclear collisions,” *Phys.Rev.Lett.* **88** (2002) 062302, [arXiv:nucl-th/0104064 \[nucl-th\]](#).
- [144] A. Muronga, “Causal theories of dissipative relativistic fluid dynamics for nuclear collisions,” *Phys.Rev.* **C69** (2004) 034903, [arXiv:nucl-th/0309055 \[nucl-th\]](#).
- [145] R. Baier and P. Romatschke, “Causal viscous hydrodynamics for central heavy-ion collisions,” *Eur.Phys.J.* **C51** (2007) 677–687, [arXiv:nucl-th/0610108 \[nucl-th\]](#).
- [146] H. Song and U. W. Heinz, “Causal viscous hydrodynamics in 2+1 dimensions for relativistic heavy-ion collisions,” *Phys.Rev.* **C77** (2008) 064901, [arXiv:0712.3715 \[nucl-th\]](#).
- [147] O. Aharony, S. S. Gubser, J. M. Maldacena, H. Ooguri, and Y. Oz, “Large N field theories, string theory and gravity,” *Phys.Rept.* **323** (2000) 183–386, [arXiv:hep-th/9905111 \[hep-th\]](#).
- [148] E. D’Hoker and D. Z. Freedman, “Supersymmetric gauge theories and the AdS/CFT correspondence,” [arXiv:hep-th/0201253 \[hep-th\]](#).
- [149] H. Nastase, “Introduction to AdS-CFT,” [arXiv:0712.0689 \[hep-th\]](#).
- [150] M. B. Green, J. H. Schwarz, and E. Witten, *Superstring Theory: Volume 1, Introduction. Volume 2: Loop Amplitudes, Anomalies and Phenomenology*. Cambridge University Press, Cambridge, first ed., 1988.
- [151] J. Polchinski, *String Theory: Volume 1, An introduction to the bosonic string. Volume 2, Superstring theory and beyond*. Cambridge University Press, Cambridge, first ed., 1999.
- [152] E. Kiritsis, *String Theory in a Nutshell*. Princeton University Press, New Jersey, 2007.
- [153] M. Bianchi, D. Z. Freedman, and K. Skenderis, “Holographic renormalization,” *Nucl.Phys.* **B631** (2002) 159–194, [arXiv:hep-th/0112119 \[hep-th\]](#).

- [154] K. Skenderis, “Lecture notes on holographic renormalization,”  
*Class.Quant.Grav.* **19** (2002) 5849–5876, [arXiv:hep-th/0209067](#) [hep-th].
- [155] S. Mrowczynski, A. Rebhan, and M. Strickland, “Hard loop effective action for anisotropic plasmas,” *Phys.Rev.* **D70** (2004) 025004,  
[arXiv:hep-ph/0403256](#) [hep-ph].
- [156] E. Braaten and R. D. Pisarski, “Simple effective Lagrangian for hard thermal loops,” *Phys.Rev.* **D45** (1992) 1827–1830.
- [157] P. Romatschke and M. Strickland, “Collective modes of an anisotropic quark-gluon plasma II,” *Phys.Rev.* **D70** (2004) 116006,  
[arXiv:hep-ph/0406188](#) [hep-ph].
- [158] C. Hoyos, S. Paik, and L. G. Yaffe, “Screening in strongly coupled N=2\* supersymmetric Yang-Mills plasma,” *JHEP* **1110** (2011) 062,  
[arXiv:1108.2053](#) [hep-th].
- [159] H. E. Haber and H. A. Weldon, “On the relativistic Bose-Einstein integrals,”  
*J.Math.Phys.* **23** (1982) 1852.